Summer 7-15-2022

FABRICATION AND CHARACTERIZATION OF CARBON NANOTUBE METAL MATRIX COMPOSITES FOR USE IN PHOTOVOLTAIC GRIDLINE APPLICATIONS

Cayla M. Nelson

Cayla M. Nelson
Candidate

Nanoscience and Microsystems Engineering
Department

This dissertation is approved, and it is acceptable in quality and form for publication:

Approved by the Dissertation Committee:

Sang M. Han , Chairperson

Yu-Lin Shen

Mahmoud Reda Taha

David M. Wilt

FABRICATION AND CHARACTERIZATION OF CARBON NANOTUBE METAL MATRIX COMPOSITES FOR USE IN PHOTOVOLTAIC GRIDLINE APPLICATIONS

BY

CAYLA NELSON

B.S., Electrical Engineering,
B.S., Engineering Physics,
New Mexico State University, 2014

M.S., Nanoscience and Microsystems Engineering,
University of New Mexico, 2018

DISSERTATION
Submitted in Partial Fulfillment of the
Requirements for the Degree of

Doctor of Philosophy
Nanoscience and Microsystems Engineering

The University of New Mexico
Albuquerque, New Mexico

July 2022

ACKNOWLEDGEMENTS

I am grateful to my advisor Dr. Sang M. Han for his direction throughout this project and guidance in helping me to build necessary research skills and experience.

This work could not have been successful without Dr. Yu-Lin Shen's expertise in finite element modeling discussed in this work.

I would like to thank Dr. Mahmoud Reda Taha for use of his composite testing laboratory and valuable feedback of this work.

I would like to thank Mr. David M. Wilt of the Air Force Research Laboratory for access to AFRL laboratories for composite integration and device characterization.

FABRICATION AND CHARACTERIZATION OF CARBON NANOTUBE METAL MATRIX COMPOSITES FOR USE IN PHOTOVOLTAIC GRIDLINE APPLICATIONS

BY
CAYLA NELSON

B.S., Electrical Engineering,
B.S., Engineering Physics,
New Mexico State University, 2014

M.S., Nanoscience and Microsystems Engineering,
University of New Mexico, 2018

Ph.D, Nanoscience and Microsystems Engineering,
University of New Mexico, 2022

ABSTRACT

Performance reliability is crucial for photovoltaic (PV) cells in both terrestrial and space-based applications. Electrical efficiency losses over time are heavily impacted by electrical losses due to microcracks within the cell structure and metallization failure. Mechanical stresses and thermal cycling of the device can lead to fracture of the current-carrying metal (Ag) lines on the surface of the device, significantly reducing output power. Incorporating carbon nanotubes (CNTs) into PV metal lines as a reinforcement, forming a CNT/Ag metal matrix composite (MMC), enhances the electrical and mechanical performance of the device. In this work the influence of CNT/Ag MMCs were explored as PV metallization integrated onto existing devices and mechanically characterized as layer-by-layer composite films. To understand the impact of CNT dimension and loading on composite microstructure, free-standing MMCs were tested under tension using Dynamic Mechanical Analysis (DMA). Finite element analysis (FEA) was used to simulate a simplified representation of the MMC microstructure. The FEA model was used in conjunction with experimental tensile data to examine potential CNT mechanical responses by viewing the nanotube phase as an effective layer.

TABLE OF CONTENTS

LIST OF FIGURES

LIST OF TABLES

CHAPTER 1: INTRODUCTION

1.1 Metal Matrix Composites as Gridlines in Photovoltaic Devices

Solar radiation is an abundant, reliable renewable energy source for terrestrial applications and a critical source of power for satellites when converted to electrical energy by photovoltaic devices. For photovoltaic devices to operate at their full potential and longest possible lifespan, mechanical reliability is crucial. The photovoltaic (PV) device structure relies on semiconductor materials that are inherently brittle like silicon, germanium, and other III-V semiconductors. The cell structure is comprised of many different materials with a range of thermal expansion coefficients [1, 2]. Mismatch of the thermal expansion coefficients can lead to microcracks within the PV device [3, 4]. Additionally, inherent defects within the cell readily form microcracks that propagate during the lifetime of the PV module[5, 6]. Defects can arise from material imperfections like molecular impurities in the semiconductor material, or during processing such as poor solder application. This is an increased issue for space PV cells that undergo drastic thermal cycles. Unlike terrestrial cells which heat and cool throughout the day, during the transition from eclipse to illumination, the high surface area to mass ratio of typical solar arrays can cause cell temperatures to slew more than 100 °C in less than a second. These thermal shocks happen thousands of times per year for spacecraft in low earth orbit and dozens for geosynchronous spacecraft. In addition to thermal effects, space and terrestrial solar cells are subjected to various forms of mechanical loading throughout their lifetime. These sources of mechanical loading can be during transportation and installation, or due to weather effects such as hail or snow [3, 7–10]. If the load exceeds the fracture stress of a material within the cell it will fracture. Microcracks can also be introduced during these

various loading processes which can only be observed by a decrease in performance or by laboratory inspection techniques. Space solar cells must also endure the significant mechanical stresses of launch which is another source of cell cracking.

Microcracks can electrically isolate large portions of the cell and cause significant power loss with continued cell operation [3, 11–13]. Cracks in the semiconductor layer create regions of increased resistance and recombination sites, reducing carrier lifetime [13]. The maximum current of the cell is also reduced when grid fingers are fractured [11]. In terrestrial applications, replacement and maintenance costs remain a challenge to the economic viability of the solar cell modules, while in space applications, a cracked cell is unable to be replaced and may lead to early failure or reduced capability of the spacecraft. Cracks have been shown to be the leading cause of failure for terrestrial PV modules in the first two years of operation[14].

While the most brittle component in present photovoltaic devices is the semiconductor, electrical damage occurs once metallization fractures. It is common that cracks within the semiconductor, or thermal cycling of the solder will induce fracture of PV metallization. The photovoltaic effect produces electron-hole pairs within the semiconductor layer that then need to be collected by the metal contacts of the PV device to power an external load. PV cell metallization is a network of larger busbars and smaller grid fingers (Figure 1.1). Carrier collection from the semiconductor photovoltaic material is done at the thinner grid fingers and then delivered to the larger busbars. To form a module, multiple cells are connected in series by soldering metal contact ribbons from cell to cell at the busbars. If solder is not properly applied at the busbar, it can cause fracture of the grid fingers. This typically occurs when solder leaks outside the busbar [2]. The

thermal mismatch causes creep strain at the busbar/finger junction cracking the solder and breaking the grid finger [1, 15]. The fracture of grid fingers leads to current losses and increased series resistance for the PV device [2]. Along with solder joints fracturing front metallization of PV cells, cracks in the semiconductor can propagate over time and lead to fractured gridlines [10].

The traditional metallization material used for PV cells is silver. Silver has the highest conductivity of any metal ($63(10^6)$ S/m) [16] but increases the overall cell cost compared to aluminum or copper. Copper is the more affordable metallization option with reduced conductivity ($59(10^6)$ S/m) [16]. For all materials, the common deposition methods for PV metallization are metal evaporation, electrochemical deposition, or screen printing of a metal paste[17]. The work presented here explores how carbon nanotube incorporation into a silver matrix can impact the mechanical properties of the resulting composite, and

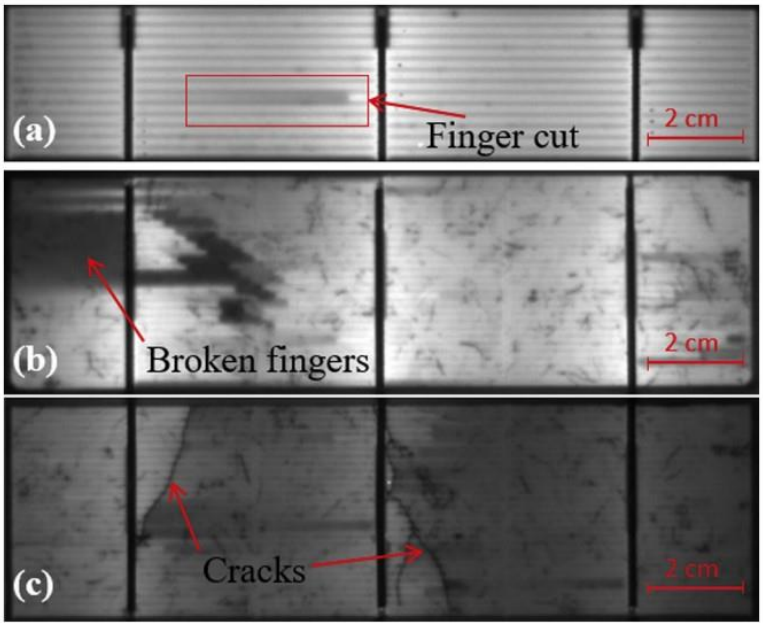

Figure 1.1 *Damage due to mechanical stresses in PV modules, dark areas indicate electrical disconnection (a) finger cut (b) finger breakage (c) wafer cracks originating from vertical busbars [2]*

resilience against cracking when integrated as PV metallization. Carbon nanotubes are known for their extraordinary mechanical properties and could enhance crack resistance of photovoltaic metallization by acting as a reinforcement within a metal matrix composite (MMC). Carbon nanotubes have conductivities that are similar to silver and copper (10^6 to 10^7 S/m) [18]. Therefore, in addition to providing mechanical reinforcement to PV metallization, carbon nanotubes can electrically bridge microcracks in the metal grid fingers and maintain current capacity.

1.2 Carbon Nanotubes in Metal Matrix Composites

The objective of a composite is to enhance a base material's properties by incorporating a reinforcement particle. The base material is referred to as the matrix and can be a variety of material classes. Ceramics, polymers, and metal matrices are the most common. For applications in photovoltaic metallization, this work is focused on a metal matrix composite (MMC) with a silver matrix material and carbon nanotubes (CNT) as the

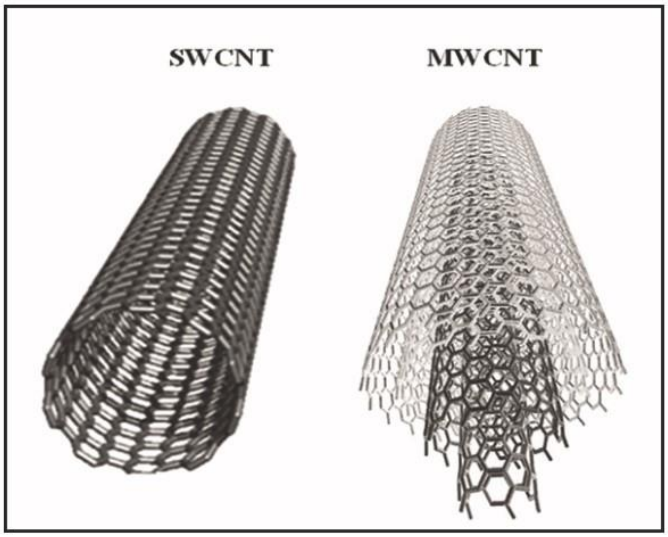

Figure 1.2 *Single-walled CNT is a carbon monolayer rolled into a cylinder. A multi-walled CNT consists of several concentric SWCNTs [19]*

reinforcement. The silver matrix is more ductile than photovoltaic semiconductor materials but as the outermost layer of a PV cell will experience higher stress and is susceptible to fracture when used as solar cell metallization. If properly incorporated during MMC fabrication, CNTs, having large elastic modulus and strength, should increase the stiffness and strength of the resulting composite.

Carbon Nanotube Synthesis

Carbon nanotubes are sheets of a one-dimensional atomic layer of carbon atoms rolled into a cylindrical structure. A single cylinder is referred to as a single walled carbon nanotube (SWCNT) [19]. Multi-walled carbon nanotubes (MWCNT) are multiple concentric layers of these cylinders with inter-wall spacing of 0.34 nm [20]. The extraordinary strength of CNTs comes from the sp^2-hybridized carbon-carbon covalent bonds. There are three common synthesis methods of carbon nanotubes: catalytic chemical vapor deposition, arc-discharge, and laser ablation. The carbon nanotubes used in this work were commercially obtained and synthesized using catalytic chemical vapor deposition.

Catalytic chemical vapor deposition (CCVD) is the most used CNT synthesis technique for mass or commercial production. A high temperature (500 – 1000 °C) chamber near atmospheric pressure is used with a carbon containing gas such as methane, ethylene, acetylene, or carbon monoxide. The growth substrate contains nanoscale metal catalyst particles to provide nucleation sites for the carbon structures. Metal particles facilitate decomposition of the gas and free carbon atoms grow into the carbon nanotube structures. Carbon nanotube length can be controlled with duration of growth, and the diameter can be controlled via metal catalyst size. Control of nanotube length and width

is beneficial since CNT aspect ratio has direct impact on mechanical performance of metal matrix composites. Chemical vapor deposition can be used to create randomly oriented CNTs or vertically aligned, tightly packed carbon nanotube forests by increasing the metal catalyst density on the growth substrate. Catalytic chemical vapor deposition of carbon nanotubes creates a high yield of nanotubes. CCVD grown carbon nanotubes typically have more defects than other synthesis methods, but defects can be reduced with a heat treatment. [20–22]

Carbon nanotubes were discovered and first fabricated using arc-discharge evaporation [23]. In this method, two graphite electrodes are placed in a high temperature furnace several millimeters apart in an inert gas environment such as helium or argon and near atmospheric pressure. A direct current of approximately 20 V and 200 A is applied across the electrodes generating an arc of carbon atoms between the electrodes. The cathode contains a catalyst metal such as iron, cobalt, or nickel. Carbon atoms condense onto the cathode growing in a helical pattern [20, 21]. Arc-discharge evaporation creates multi-walled CNTs with high crystallinity. However, other carbon structures such as carbon spheres (buckyballs) are synthesized in this method. Therefore, arc-discharge is

Table 1-1 *Comparison of most common CNT synthesis methods*

Method	Dimensional Control	Defects
CCVD	high	high
Arc-discharge	poor	low
Laser ablation	low	low

not ideal for high-yield applications since the final product must be further processed to obtain pure CNTs. Arc discharge evaporation also offers no control over the CNT geometric parameters such as diameter, length, and the number of multiwall layers [21, 22] which are crucial to providing consistent results and analytical correlations.

Laser ablation uses a high-powered pulsing laser to vaporize a graphite substrate. The substrate also contains a metal catalyst. Carbon atoms are vaporized and condense as nanotubes. Laser ablation produces mostly single-walled carbon nanotubes with very high quality. However, as with arc-discharge evaporation, the resulting CNT dimensions are difficult to control. [21, 22]

CNT Strengthening Mechanisms and Microstructural Impacts

The elastic modulus of individual CNTs can be 1800 GPa loaded axially [24]. Tensile strength values up to 110 GPa have been reported [25–27]. Many analytic models exist to predict the composite elastic modulus and strength [28]. These models indicate the resulting mechanical properties of the composite to depend on numerous variables from CNT synthesis, MMC fabrication method and final application. Common variables of interest are CNT content, aspect ratio, orientation, porosity, CNT/matrix interface adhesion, and dispersion/agglomeration. Analytical models of composite behavior also suggest various methods of mechanical reinforcement by the carbon nanotubes that impact the final composite mechanical response. The most desirable mechanism of strengthening a metal matrix via CNTs and thus enhanced composite mechanical properties is load transfer from the matrix to the reinforcement. The load transfer mechanism is most strongly impacted by the reinforcement/matrix interface and the reinforcement dispersion [29].

The strengthening mechanism of load transfer is based on the shear lag analytic model [30] which assumes load is transferred from matrix to reinforcement by a shear force at the interface for fibers in a composite given by:

$$\frac{l_f}{d_f} = \frac{\sigma_f}{4\tau_{mf}} \quad \text{(Eq. 1-1)}$$

Where l_f is the fiber length, d_f is the fiber diameter, σ_f is the stress transferred to the fiber, and τ_{mf} is the shear stress at the matrix fiber interface [28, 29]. According to the shear lag model, fibers with a larger aspect ratio will be capable of a higher load transfer. It is common in CNT-metal matrix composites for an interface containing carbides to exist, requiring load transfer from the matrix to pass through an additional layer before reaching the carbon nanotubes. Stress transfer efficiency from matrix to CNT depends on the shear stress of the CNT/Ag interfacial layer. A weak interface, with shear stress less than the applied stress, will reduce the composite strength and lead to CNT pull out during axial loading [28, 29, 31]. Within multi-walled carbon nanotubes (MWCNT), load is also transferred from wall to wall. Initially stress is transferred from the matrix to the outer wall. Once the outer wall fractures load is transferred the inner walls which begin to fracture in succession, see Figure 1.3 [26, 29, 32]. Defects within the individual walls, such as those introduced from CCVD synthesis, can lead to crosslinking between walls and ultimately increase the wall to wall load transfer ability [26]. This leads to less complete fracturing of MWCNTs within composites. Without defects in the walls of the tubes, load transfer between walls is small due to the van der Waals interactions between them [28, 29, 33]. Therefore, a higher percent of MWCNT defects inherent to the CCVD fabrication

can contribute favorably to the desired load transfer characteristics of the Ag/CNT composite.

Ideal load transfer is the dominant strengthening mechanism within CNT-metal matrix composites, leveraging the full axial strength and stiffness of the carbon nanotubes. However, it is not the only strengthening method that can occur from CNT reinforcement. Another common mechanism is grain refinement of the metal matrix due to CNT pinning. Numerous studies have shown a reduction in grain size of the metal matrix with CNT

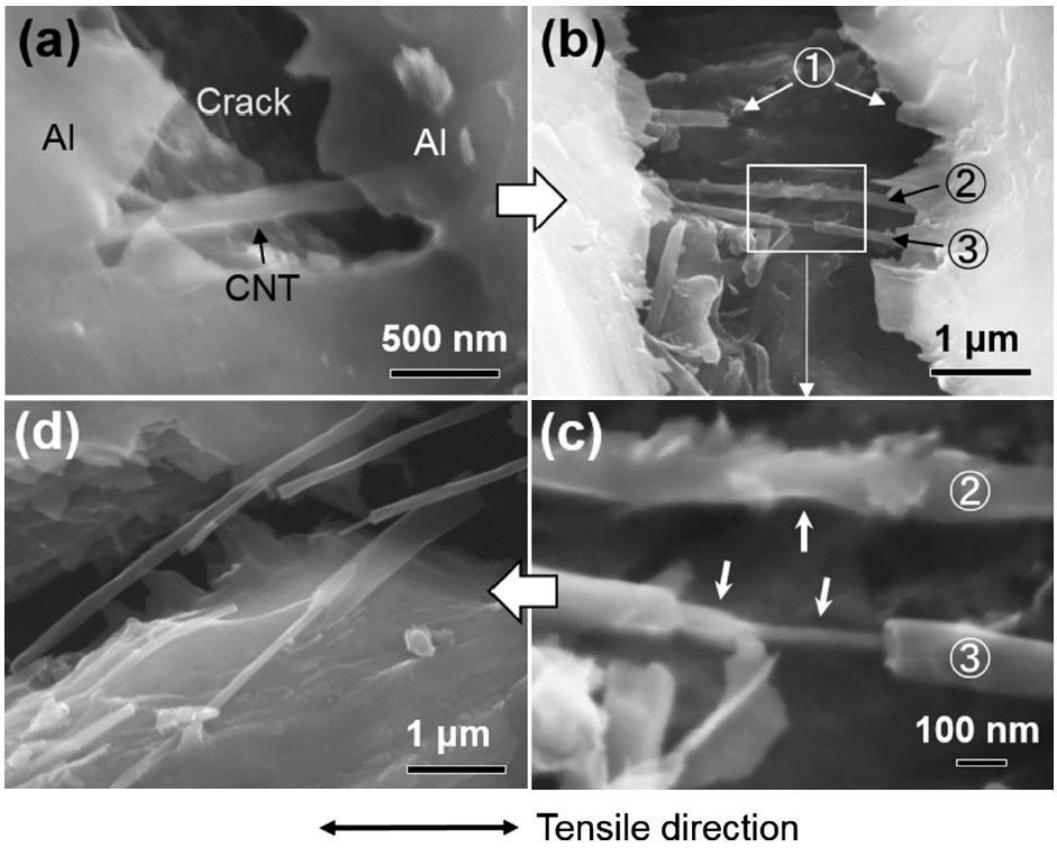

Figure 1.3 *Fracture of MWCNTS in tension. (a) CNTs bridge crack within metal matrix. (b) CNTs undergoing different fracture processes of walls in-situ. CNT ① shows all walls have been fractured. c) CNT ② and ③ indicate outer walls have been fractured, as indicated by reduced CNT diameter, and load is transferred between walls. d) Resulting CNT facture post tensile test. [29]*

incorporation [34–38], see Figure 1.4. The Hall-Petch relation (Eq. 1-2) gives an inverse relationship between yield stress (σ_y) and the grain size (d), therefore composites with a reduction in grain size will have higher yield stress [39, 40].

$$\boldsymbol{\sigma_y = \sigma_0 + kd^{-1/2}} \quad \text{(Eq. 1-2)}$$

The stress term (σ_0) is a constant that represents the yield stress of polycrystal with large grains [41]. The material constant (k) is a strengthening coefficient. The yield stress of a material is defined as the onset of plastic or permanent deformation and can be defined as the force required for plastic deformation divided by the specimen's cross-sectional area. Plastic deformation is caused by the movement of dislocations (linear atomic defects) throughout the crystal structure. Defects and dislocations are ultimately the cause of crack initiation in crystalline materials under loading. Grains of the material are regions that have the same crystal orientation and atomic ordering.

There have been numerous physical explanations for the Hall-Petch relationship [42]. The initial reasoning for increased yield stress with decreased grain size proposed by Hall and Petch [39, 40] was that grain boundaries cause dislocations to pile up, preventing dislocation motion and requiring a larger stress for plastic flow. Another commonly used explanation presented by *Ashby, 1970* [43] suggested that in order for multiple grains to undergo deformation, additional geometrically necessary dislocations (GNDs) are introduced to accommodate the deformation. The GND density increases as grain size decreases. These additional dislocations contribute to strengthening by reducing nucleation of new dislocations.

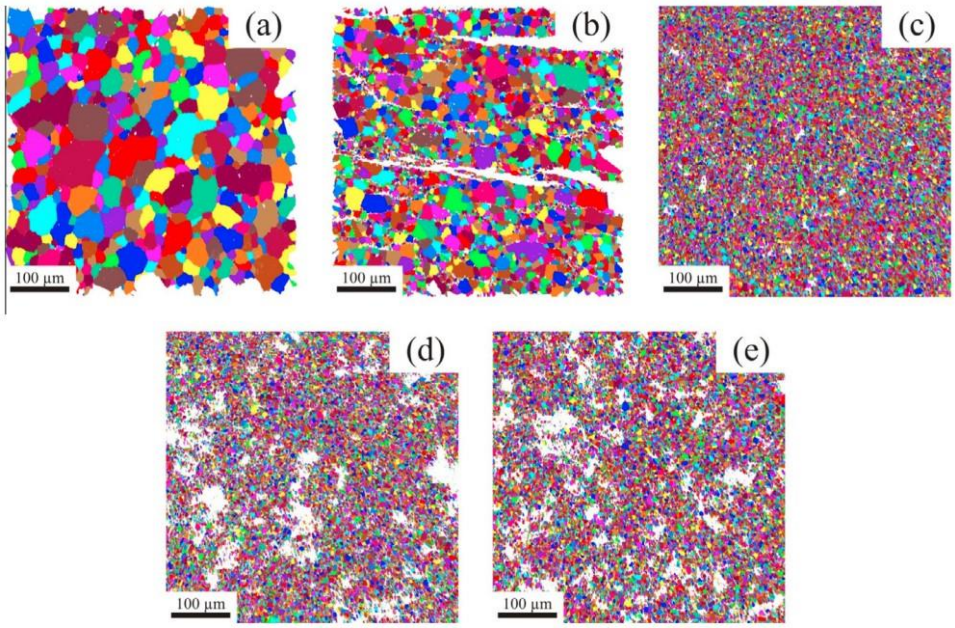

Figure 1.4 *Reduction in grain size due to CNT incorporation visualized with electron backscatter diffraction (a) Pure Ni (b) – (e) CNT/Ni composite with CNT wt% of 1%, 2%, 3%, and 5% [35]*

Carbon nanotubes can reduce the grain size of the surrounding metal matrix by pinning grain boundaries, see Figure 1.4 [35, 44]. The Zener pinning relationship says the subsequent grain size (d) due to particle pinning is proportional to the particle radius (r) and inversely proportional to the volume fraction (V_f) of the pinning particle [45]:

$$\boldsymbol{d = \frac{K*r}{V_f}} \quad \text{(Eq. 1-3)}$$

Where K is a proportionality constant. Due to increased agglomerations with increasing CNT content, the matrix grain size tends to plateau at increased CNT volume fraction [35]. Agglomerations are clusters of CNTs that form due van der Waals attractions of the CNT sidewalls. These clusters often form during composite fabrication. It is difficult to redisperse the individual nanotubes of the agglomerate once they form. If other particles are present in the composite, they may also pin grain boundaries and contribute to overall

composite strength, but it is not always straightforward to correlate. In summary, CNTs can pin the matrix grain boundaries during composite fabrication leading to smaller grain sizes creating a strengthening mechanism according to the Hall- Petch relationship. This strengthening effect can be used in combination with the load-transfer mechanism to explain effects of CNT as reinforcement in composites.

In a similar effect to grain pinning, the carbon nanotube itself functions as an obstacle to atomic dislocation migration. The matrix dislocations bend around the CNTs and start to pile up in a phenomenon described by Orowan looping [46–48]. This is another strengthening mechanism that increases over all MMC yield stress and can reduce crack initiation sites by preventing dislocation movement.

The shear lag, grain refinement, and Orowan looping mechanisms are some of the most expected methods of increasing strength with CNT reinforcement in metal matrix composites. Any given composite will have a combination of several strengthening mechanisms dictated by the microstructure. The microstructure is affected by parameters such as CNT geometry, dispersion, agglomeration, CNT/metal interface and processing techniques that determine what mechanism is dominant. These parameters can be controlled during composite fabrication and will be explored further in the body of this work. *Chen, 2017* [48] showed that for an aluminum/CNT composite with CNTs uniformly dispersed throughout and tested in tension, the mechanical enhancement from grain refinement was less than 10%, between 20 – 35% from alumina particle pinning, and 60-70% directly from CNTs either by load transfer or Orowan looping. *Chen, 2015* [29] showed load transfer to be the dominant reinforcement mechanism based on CNT fracture examination via in-situ tensile testing of Al/CNT composites. However, other

strengthening effects contribute and cannot be ignored in final material analysis or simulation.

Although the shear lag model indicates a better load transfer for a *large* aspect ratio of CNT, it has been shown that a *smaller* aspect ratio (specifically length) actually leads to a better dispersion and higher mechanical properties from a reduction in agglomerates [44, 48, 49]. Aspect ratio is defined as the CNT length to width ratio *(l/d)*. Carbon nanotubes range in diameter and length values based on processing techniques. However, the potential lengths of carbon nanotubes have a much greater range than the diameters. Therefore, length is focused on more heavily when discussing the impacts of CNT geometry on the resulting composite mechanical properties. The CNT length also has an impact on the strengthening mechanism within the composite. For very short CNTs (aspect ratios <10) the main reinforcement contribution appears to be Orowan looping, whereas for CNTs with higher aspect ratios (> 40) the main mechanism is load transfer via the shear lag theory [29, 48]. A study [44] comparing short and long CNTs found that the short CNTs resulted in better dispersion, reduced matrix grain size and increased mechanical properties compared to the long CNTs.

A significant limiting factor in the mechanical properties of a CNT-metal matrix composite is the dispersion and degree of agglomeration of the CNTs during fabrication [28]. Additionally, carbon nanotubes tend to form a wave shape and cluster due to attractive CNT-CNT van der Waals forces and their large surface area [28, 50]. Short carbon nanotubes lend themselves more to uniform dispersion due to the reduction in surface area leading to an enhanced composite mechanical response. The CNT clusters or agglomerations tend to increase with increased CNT content [28, 36, 51]. Several studies

have shown a trend of increasing mechanical properties up to a critical CNT loading, followed by a decline in properties likely due to the increased carbon nanotube clustering [34, 52–56]. Agglomerations create areas of stress concentration under loading that lead to crack initiation sites and early composite fracture [57]. In this work, both long and short CNTs are used for composite fabrication with lengths ranging from 0.9 – 10 μm.

The inherent carbon nanotube waviness and random orientation may hinder composite mechanical properties since their enhanced stiffness and strength is a result of axial loading of the C-C bonds. The radial elastic modulus of multiwalled carbon nanotubes has been reported to be around 30 GPa [58] compared to approximately 1 TPa axially [24]. Computational modeling has shown CNT waviness to decrease the carbon nanotube's effective elastic modulus [59, 60]. A molecular dynamics study by *Alian and Meguid, 2017* [61] showed that for uniformly dispersed CNTs, waviness can actually increase the interfacial shear strength between CNT and matrix reducing carbon nanotube pull out. The study also showed CNT agglomeration to be more detrimental to composite mechanical properties than CNT waviness.

Carbon bonds within the plane of carbon nanotubes are strong overlapping sp^2 hybridized σ-bonds. Normal to the CNT plane are the weaker π-orbitals. [62] For this reason CNTs are strong along the cylinder axis, but interactions between CNTs and CNT-metal are weak. This is also why defects within the carbon nanotubes can enhance interfacial interactions, by providing covalent bonding sites at the σ-bonds. This can be through cross linking of the CNT walls within multiwalled nanotubes, or the CNT-metal interface. If no treatment is done to carbon nanotubes, metals attach via van der Waals interactions. However, CNTs can be treated so that covalent bonding to metal atoms is

possible. A common treatment is the addition of carboxyl groups to atomic sites along the CNT. For this method, carbon nanotubes are sonicated in a 3:1 mixture of H_2SO_4:HNO_3, then rinsed in DI water via vacuum filtration [63]. This results in COOH- functional groups covalently bonded onto the CNT surface [64]. Metal atoms can then also covalently bond to the CNTs via the functional groups. Functionalization of the carbon nanotubes also leads to better dispersion and suspension in aqueous solutions [63]. Though functionalization increases bonding sites and allows better dispersion and suspension, this acid treatment can also cause damage that potentially degrade their mechanical properties. Non-covalent functionalization is also possible by treating CNTs with a surfactant such as sodium dodecyl sulphate. This method does not cause CNT damage, but it has been shown less effective in enhancing composite mechanical properties compared to covalent functionalization [63]. Another form of non-covalent functionalization is polymer wrapping. Polymer chains helically wrapped around CNTs help to disperse the carbon nanotubes in solvents preventing agglomerations for fabrication processes [65, 66].

With these contributions to CNT performance in MMC strengthening in mind, it has been shown the typically dominant strengthening mechanism for carbon nanotube-metal matrix composites is load transfer with other contributions from grain size refinement and CNT dislocation pinning. The two significant hurdles in composite fabrication, limiting final composite properties, are adhesion of the CNT-metal interface and uniform dispersion of carbon nanotubes with minimal agglomerations. Using shorter nanotubes at an optimal CNT loading has been shown to provide the greatest success in reducing clustering and increase dispersion uniformity.

1.3 Scope of Work

This work investigates the impact of the carbon nanotube (CNT) microstructure on the mechanical properties of the metal matrix composite (MMC). The MMC is integrated onto prefabricated photovoltaic (PV) cells, and electrically characterized before and after cracking. Metal matrix composite films are then fabricated and mechanically characterized. In the case of tension testing, the resulting stress-strain response reveals the composite mechanical behavior as a function of CNT loading. A parametric assessment is performed using a finite element analysis (FEA) model, where possible effective properties of the CNT domain are used for fitting the experimental stress-strain responses. The values of the extracted effective CNT properties give phenomenological insight into the strengthening impact and mechanism of the CNT inclusions.

As shown in section 1.2, individual CNTs can have extraordinary mechanical properties [22, 24, 67]. However, in macro-scale applications, agglomerations of the CNTs tend to drastically lower these values for CNT networks and films [57, 68, 69]. Even in highly aligned and densely packed CNT films, the elastic modulus is two orders of magnitude less than reported individual CNT values due to weak van der Waals interaction between the CNTs [70]. Here, we use experimental methods and FEA to understand the electrical and mechanical behavior of the Ag/CNT metal matrix composite.

Chapter 2 is a review of the fundamental techniques for the fabrication and characterization methods used for composite synthesis and testing. Electrochemical deposition was used to deposit silver for MMC integration onto PV cells and for MMC fabrication on a GaAs substrate for nanoindentation testing. Electron beam metal evaporation was used for silver deposition of the free-standing MMC thin films. Spray

coating methods were used to coat a CNT layer between two silver layers for both MMC metallization on to solar cells, and free-standing MMC film fabrication. Initial mechanical characterization attempts were done using nanoindentation. These nano-scale results indicated that tension testing of MMC thin films would provide more insight into composite mechanical behavior. Scanning electron microscope imaging was used for CNT quantification by imaging and analyzing the CNT surface area coverage after spray coating.

Chapter 3 reviews the methods of MMC integration as gridlines in a photovoltaic cell. After integration, the devices are characterized using electroluminescence and light current-voltage (LIV) testing before and after introducing cracks. Electroluminescence provides a visualization of how cracks impact current flow within the device. LIV provides the electrical response before and after cracking, allowing analysis of performance parameters. The most significant parameter being short circuit current.

Chapter 4 describes the mechanical characterization of the composite. Mechanical testing of layer-by-layer MMCs deposited on a GaAs substrate and tested using nanoindentation gave initial insight of CNT incorporation into a metal matrix. The process of free-standing MMC thin film fabrication and CNT quantification is described. The free-standing MMC films were tested in tension using dynamic mechanical analysis (DMA). The results of tension testing for three different datasets of free-standing MMC films with varying carbon nanotube geometries and spray coating methods are presented and discussed.

Chapter 5 discusses a finite element model of a simplified CNT/Ag microstructure with the objective of extracting potential CNT effective values of the composites fabricated

in Chapter 4. The model uses a parametric analysis of a range of possible values for elastic modulus and yield stress for the effective CNT layer.

CHAPTER 2: FABRICATION AND CHARACTERIZATION TECHNIQUES

2.1 Fabrication Techniques

Two common fabrication methods of photovoltaic (PV) metal lines are electrochemical deposition and electron beam metal evaporation, a form of physical vapor deposition (PVD). Both were explored as silver deposition techniques for the metal matrix composite (MMC) films. Electrodeposition was used for integration of the MMC as metal gridlines onto an existing PV device. Electrodeposition can be an advantageous deposition method over metal evaporation because it does not require the additional time of operating at ultra high vacuum. An MMC film was additionally deposited onto an GaAs substrate for nanoindentation testing. For tension testing of a free-standing composite film, metal evaporation was done. Metal evaporation provided a higher quality silver film that could be handled more readily as a free-standing film compared to composites fabricated by electrochemical deposition.

Spray coating of the carbon nanotube layer was chosen as a fabrication method that could be easily integrated into the photovoltaic gridline deposition process on at a manufacturing scale. Several spray coating apparatuses were used including affordable gravity feed devices like an airbrush and paint spraying gun. An ultrasonic atomizer was also explored as a more costly option, but with more control over spray parameters.

2.1.1 Electrochemical Deposition

In electrochemical deposition (or electroplating), electrolysis is used to deposit material, typically metal, from a source electrode to a substrate electrode. In the most basic electroplating setup, an anode of the source metal and a cathode for material deposition are placed in an electrolyte solution that contains ions of the source metal, in this case silver. The anode and cathode are connected to the positive and negative terminals of a power supply respectively to form an electrically conducting electroplating cell. Once the electroplating circuit is complete, free electrons are pulled out of the anode via the power supply and silver atoms within the anode are oxidized, losing an electron. The positively charged silver ions then dissolve away from the anode into the plating solution and are drawn to the cathode due to its negative charge. At the cathode, electrons moving through

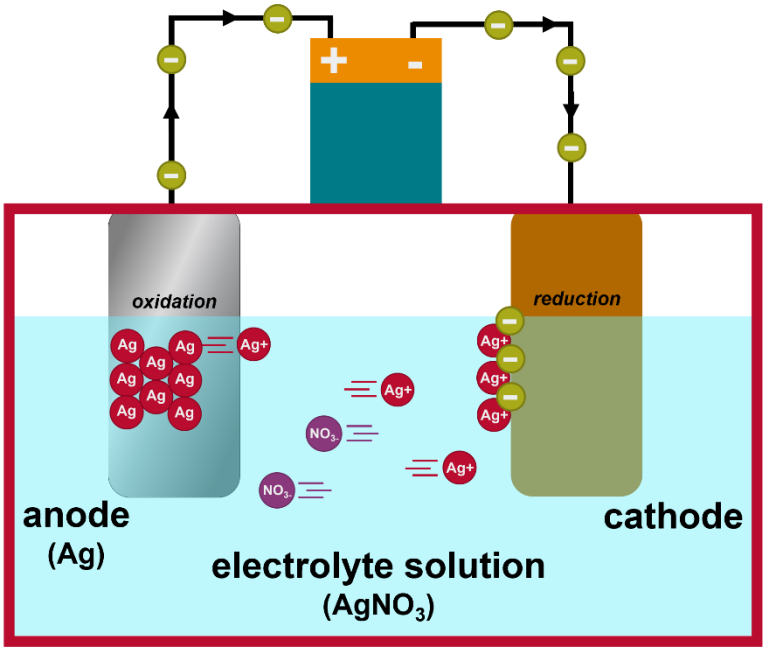

Figure 2.1 *Electroplating process. Ag atoms from anode are oxidized, silver ions from electrolyte solution and anode attract to cathode where reduction occurs, gradually forming a film*

the circuit cause a reduction of the positive silver ions at the surface of the anode, neutralizing the atoms into solid silver and initiating silver growth. This process is illustrated in Figure 2.1. [71]

The traditional silver-plating solution has been potassium silver cyanide [$KAg(CN)_2$]. Due to toxicity and environmental hazards [72], a commercially manufactured silver nitrate bath was used in this work, *E-Brite 50/50 RTP* produced by *Electrochemical Products Inc (EPi)* [73]. This solution is for use at room temperature with an optimum pH of 9.2 and a cathode current density range of 3 – 10 mA/cm^2. In the electrolyte solution the silver nitrate ($AgNO_3$) ionic compound dissolves into Ag+ and NO_3-. The Ag+ ions are drawn to the cathode and the NO_3- ions are drawn to the anode enabling current flow through the solution. This process reaches an equilibrium where the concentration of silver ions in the solution is maintained during deposition with the rate of oxidation of silver atoms at the anode being equal to the rate of reduction of silver atoms

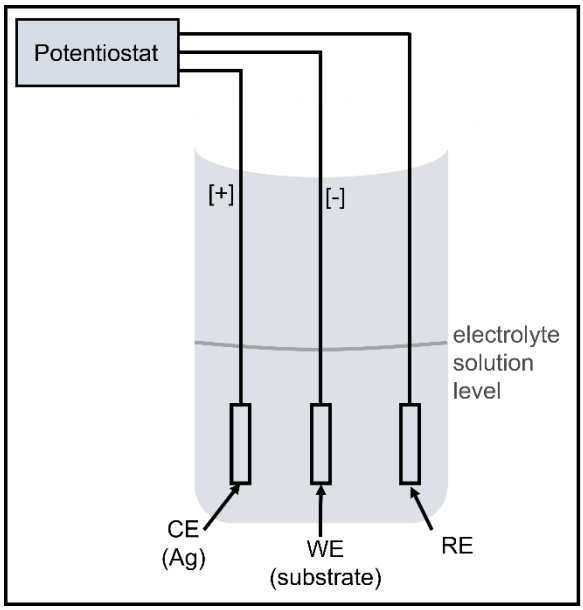

Figure 2.2 *Three-electrode electrodeposition setup. CE-counter electrode, WE- working electrode, RE- reference electrode*

at the cathode. The silver nitrate solution does not produce as high quality of film as the traditional cyanide baths [71], but the reduced toxicity permits greater flexibility in a laboratory setting.

A three-electrode cell was used for electrochemical deposition of silver in this work to monitor both the potential and current during deposition, see Figure 2.2. The cathode or working electrode (WE) is the deposition substrate. A reference electrode (RE) is used as a mechanism to measure voltage at the cathode. The counter electrode (CE) is the source material anode. All electrodes are connected to a potentiostat *(Princeton Applied Research PARSTAT 3000A-DX)* to measure current and voltage during the deposition process. The potential of the cathode is kept constant relative to the reference electrode.

The growth pattern and quality of growth for an electroplated film depends on many factors; cathode potential, current density, additives, substrate, and impurities are the most impactful. The current density has the largest impact on growth pattern and quality of the deposit [74]. A current density is chosen and that dictates the potential set between the working electrode (cathode) and reference electrode. The ideal current density for this setup was found to be 3 mA/cm^2 [74, 75]. Brightness and surface roughness (leveling) can be controlled by introducing additives to the plating solution. In this setup, the selected E-brite 50/50 solution has been formulated to provide sufficient quality without additives. The surface of the substrate influences the structure of the deposit. For silver electroplating, a thin layer (100 nm) of silver was evaporated onto a GaAs substrate or the gridlines of an existing cell as a seed layer. The electrodeposited film is initially formed by clusters of silver adions forming nucleation sites along the surface of the substrate. Those clusters form into crystals that eventually lead to a polycrystalline film. The

substrate has a significant role in the initial structure, but for films over one micron the electrodeposition parameters (mainly current density) are more important to the microstructure of the deposit which was the case in this work [71].

Most optimization work for this electroplating setup was a large part of another PhD research project [75]. In this work, electrodeposition was used for coating existing gridlines of a photovoltaic cell with a metal matrix composite (MMC) for device level electrical characterization and analytical modeling before and after cracking. It was also used for fabricating MMCs on a GaAs substrate for nanoindentation mechanical testing.

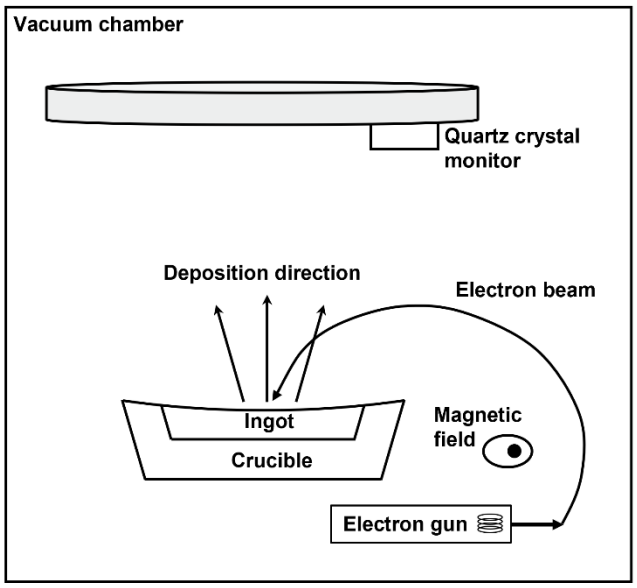

Figure 2.3 *Schematic of fundamental components and setup for electron beam evaporation*

2.1.2 Electron Beam Evaporation

Electrodeposition is a faster deposition method compared to electron beam evaporation mainly because e-beam deposition requires pumping down to low pressures of high vacuum. However, electron beam evaporation provides a better quality film to be used as a free-standing film for tension testing. Electron beam evaporation is used to

deposit the top and bottom silver layers of the free-standing metal matrix composite (MMC) to be mechanically characterized. This method of physical vapor deposition (PVD) uses an accelerated electron beam controlled by a magnetic field to vaporize the source material. The deposition is done under high vacuum to encourage transport of the vapor of source material atoms to condense on the deposition substrate. The high vacuum also reduces impurities in the deposition environment. The electron beam is created via thermionic emission of a filament, commonly tungsten. The emission current applied to the filament controls the intensity of the electron beam and determines the deposition rate of the source material onto the sample.

A schematic of the basic components and setup for electron beam evaporation are shown in Figure 2.3. The tungsten filament is the cathode within the electron gun and the anode is the material source to be heated. The negatively charged cathode ejects electrons that are then attracted to the source material (anode) where they can heat the material to a molten state and produce a vapor. A potential difference is maintained between the cathode and anode of 10 kV, accelerating the electrons to the source. An operating pressure of about 10^{-3} Torr or less is required to avoid electron scatter within the produced electron beam. The tungsten filament is positioned out of the path of the molten material and electromagnets control the electron beam location on the workpiece. The piezoelectric properties of a quartz crystal are used to measure the deposition thickness. The resonance frequency of the quartz is inversely proportional to the crystal thickness which grows as silver is deposited in the test chamber. [76] For the free-standing films characterized in this work, silver was deposited at a pressure of at least $2(10)^{-6}$ Torr and a deposition rate of 2.5 Å/s on glass substrate with thicknesses of 2 μm for each layer.

2.1.3 Spray Coating

Throughout this project several different spray deposition apparatuses were used to coat carbon nanotubes (CNTs) for metal matrix composite (MMC) fabrication. Carbon nanotubes were suspended in a fluid solvent at a given concentration. Two types of atomizers were used for CNT deposition: two different gravity fed, pressure nozzles and an ultrasonic nozzle. The gravity feed spray coaters are extremely affordable and had potential for offering low-cost CNT deposition. However, issues with controlling flow rate and atomized droplet size led to inconsistent nanotube deposition and poor repeatability. The ultra-sonic atomizer is more appropriate for a laboratory setting with precise control of flow rate and production of smaller droplet sizes.

In spray coating applications it is generally favorable to have a reduced average droplet size emitted from the nozzle. Smaller droplets lead to a more uniform coating and, in the case of CNTs, help to reduce agglomerations. Emitted droplets of the CNTs in solution are deposited on the substrate where solvent evaporation begins. During evaporation the CNTs can pool together leaving behind agglomerations. The outer edges of the droplets evaporate first. As this occurs, liquid from the center of the droplet moves toward the outer edges transporting CNTs toward the edges where they are left as agglomerates after the solution fully dries [77]. This phenomenon is referred to as the coffee ring effect [78]. The agglomerations due to the coffee ring effect can be reduced for CNT deposition by lessening the droplet size and using a heated sample stage for rapid evaporation.

In gravity fed, pressurized atomizing nozzles there are several parameters that impact the droplet size; flow rate, pressure, solvent surface tension, solvent viscosity, and

nozzle-to-sample distance. Droplet size decreases with decreasing flow rate, surface tension and viscosity [79–81]. Droplet size is also decreased with increasing pressure and nozzle-to-sample distance [79, 80, 82]. With gravity feed spray nozzles, the liquid is forced into droplets (or atomized) by a pressurized gas, commonly an air compressor [83]. The compressed air exerts a force on the liquid solution in the reservoir. When the pressure of the compressed air is greater than the internal pressure of the liquid droplet, atomization occurs.

Initial CNT deposition was done with a gravity fed airbrush aligned above the sample which is mounted on a linear translation stage, the CNT quantity was varied by varying the number of cycles the samples passed beneath the airbrush nozzle. The CNT solvent used with this nozzle was typically DI water at a concentration of 1.3 g/L. DI water kept the CNTs suspended longer than other common solvents. While the airbrush nozzle provided an extremely low cost and rapid method of deposition, the manual control of flow rate prohibited accurate control leading to large variations in output sample quality. Droplet size was also larger than optimal leading to significant agglomeration due to uneven evaporation, even when paired with the heated stage.

To continue exploring low-cost spray coating applications, a larger high-volume low pressure (HVLP) gravity feed air spray gun was used. The HVLP spray gun operates at a higher pressure compared to the airbrush nozzle (40 psi compared to 20 psi). To further reduce droplet size, chloroform ($CHCl_3$) was used as the solvent due to its lower viscosity and surface tension when compared to deionized water, see Table 4.1. Both the airbrush nozzle and the HVLP nozzle had a nozzle-to-sample distance of 12 inches.

Ultrasonic atomization is more favorable compared to the gravity feed atomizers. The droplet size and size distribution [84] are lower for ultrasonic nozzles giving a more homogeneous coating. The ultrasonic nozzle also offers control over flow rate, enhancing the repeatability of CNT surface coverage for the same translations cycles of the nozzle over the sample. Rather than dispersion by mechanical force from air pressure as in the gravity feed mechanisms above, when an ultrasonic frequency is passed through a liquid, waves are generated within the liquid. When the intensity is high enough the bulk of the liquid begins to eject droplets and atomize [85]. In 1961 the droplet size produced by ultrasonic atomization was determined [86]:

$$\boldsymbol{D = 0.34\left(\frac{8\pi\sigma}{\rho f^2}\right)^{1/3}} \qquad \text{(Eq. 2-1)}$$

Where σ is the liquid surface tension, ρ is the liquid density, and *f* is ultrasonic frequency. For this work, the *Sonaer Narrow Spray Atomizer Nozzle* was used at a frequency of 130 kHz. To direct the atomized liquid a spray shaper is used, *Sonaer's Pin Point Spray Shaper*. The spray shaper has an inlet port for compressed air. The pressure is small, around 5 psi, to direct the flow onto the sample and contributes very little to the droplet size or atomization effects. The frequency is passed into the nozzle via an ultrasonic frequency generator (*SONOZAP Atomizer Generator*). The liquid is passed into the nozzle with a syringe pump, at a given flow rate. The atomizer nozzle is attached to a linear stepper motor that translates over the sample. The sample is placed on a hot plate to speed up evaporation of the solvent. The nozzle-to-sample distance is 3.5 inches. Low CNT concentrations are used (≈ 0.0007% wt.) to avoid agglomerations [87]. The nozzle speed

was set to 1250 mm/min which was slow enough to observe solvent evaporation on the substrate between passes.

2.2 Characterization Techniques

Mechanical characterization of the composites was done using nanoindentation and tension testing via dynamic mechanical analysis (DMA). Nanoindentation was used for initial testing of layer-by-layer films, but ultimately tensile properties of the composite as a free-standing film gave more insight into the MMC mechanical response. The majority of experimental mechanical data in this work is obtained by DMA tension testing. Scanning electron microscopy was a crucial component of CNT quantification. SEM images of the CNT layer surface were analyzed using computational methods to obtain surface coverage values of the carbon nanotubes.

2.2.1 Nanoindentation

Nanoindentation was used as an initial mechanical test method for characterization of the metal matrix composite (MMC). MMC films for nanoindentation testing were fabricated using electroplated silver and either nanospread or dropcast carbon nanotubes on a gallium arsenide (GaAs) substrate.

The primary measurements during nanoindentation are penetration depth of the tip into the sample and the applied load of the indenter tip. These measurements are correlated to the material's hardness and elastic modulus. An example curve of the load-displacement measurement for a single indentation is shown in Figure 2.4. The indentation tip is typically made of diamond with a tip diameter around 100 nm. For this work, a pyramidal diamond Berkovich indenter was used. Over time the indentation tip begins to blunt,

causing errors within the measurements [88]. Based on the indenter type, instrumentation software attempts to account for blunting effects. Once the tip begins to blunt, errors are more pronounced for shallow indentation depths. A mechanical load is applied to the tip up to a penetration depth defined by the test parameters at a given loading rate then the tip is unloaded typically at the same rate with load and depth being continuously recorded. The indentation displacement is measured using an electrostatic transducer. Due to the sensitive nature of measuring atomic scale displacements (≈ nm) and applying small loads (≈ mN), the test environment must be isolated from any vibrations or fluctuations in ambient conditions. A dwell time is typically added to the test between loading and unloading to allow the creep rate of the material under test to stabilize. Individual indentations are made across the samples with spacings large enough to prohibit interference between measurements. The material properties of the sample are calculated based on the interaction of the tip with the sample material. The indentation depth and indenter tip properties are used to calculate the contact area (A_s). Which is then used for both the hardness (H) and reduced elastic modulus calculations (E_r) done by the instrumentation software. Therefore, the reliability of the contact area measurements is important for accurate material properties measurements. The hardness is calculated using the maximum load (P_{max}) and the contact area:

$$\boldsymbol{H = {P_{max}}/{A_s}} \qquad \text{(Eq. 2-2)}$$

The elastic modulus is calculated using the Oliver-Pharr method [89, 90]:

$$\boldsymbol{E_r = {\sqrt{\pi}S}/{\beta 2\sqrt{A_s}}} \qquad \text{(Eq. 2-3)}$$

Where S is the stiffness, calculated by a user defined percentage of the unloading curve. The parameter β is the indenter shape constant. The term "reduced elastic modulus" is the elastic modulus of the combination of the measured material and the indenter tip. The contact area can be affected by surface roughness since it is calculated using the penetration depth. Variations in surface can cause measurement errors [91]. The point of first surface contact (depth = 0) for the indenter can be obtained by several methods. The two most common are either using a preset force to determine when the depth is set to zero, or the force is monitored before indentation and when there is a spike in load, the depth is adjusted to zero [92]. Errors in determination of the zero-depth point propagate throughout the entire test. Measurements of contact area can also be erroneous due to "pile-up" where the material of the sample piles up around the indentation impression causing a greater contact area than is measured erroneously calculating hardness and reduced modulus [90, 93]. Pile

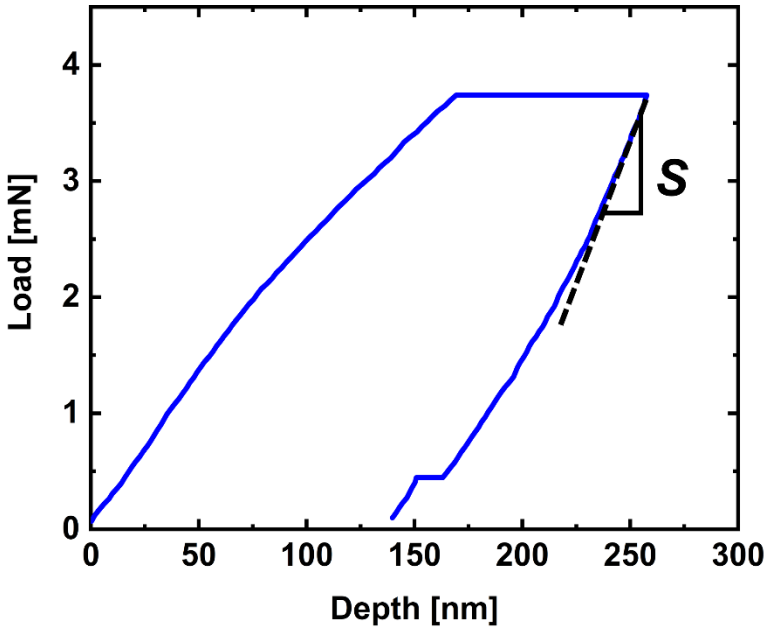

Figure 2.4 *Loading and unloading curve example of nanoindentation test with a 60 second dwell time at maximum load to allow for creep effects. Stiffness (S) is illustrated as the slope of the unloading curve.*

up is common in soft, elastic-plastic materials such as metals or metal matrix composites. The film substrate can contribute to the mechanics of the film measured by nanoindentation. To avoid substrate effects in the measured material's data the penetration depth of the measured material should not be more than 10% of its total thickness [89].

2.2.2 Scanning Electron Microscope

A scanning electron microscope (SEM) is used to image the carbon nanotube (CNT) layer of the metal matrix composite after spray coating and determine the CNT surface coverage. The components of the SEM are arranged in a column under high vacuum with an electron source at the top and ending with the specimen to be imaged at the bottom. Electrons accelerate down the column and bombard the sample. Scattered electrons from the sample material then enter detectors to form an image. The electron source is an electron gun composed of a tungsten filament cathode with an anode near by to accelerate the electrons toward the sample. The tungsten filament generates electrons via the thermionic effect. A high voltage ranging from 1 eV to 50 eV is applied at the electron gun. Commonly, the beam voltage is near 20 eV. Lower voltages give way to more aberrations within the beam and less electron scattering at the specimen, resulting in a poor image. Donut shaped electromagnets focus the beam as it passes through the annulus. Each condenser lens decreases the beam spot size by 10 – 40x and the final spot size can be decreased as low as 1 nm depending on the probe current [94]. There are traditionally two condenser lenses and one objective lens. The objective lens is the strongest and help to correct aberrations. To produce a two-dimensional image of a sample, a scanning coil sits above the objective lens and is used to rasterize the beam to scan the sample area under investigation. The rasterized scan area is the region of the resulting

image. The magnification of the image is the ratio of the generated image size to the beam scan area. Magnification is increased by decreasing the scan area. The deflection system also allows the user to select the region of the sample to be imaged by moving the beam location. The sample stage is positively charged, therefore sample charging must be considered for certain samples, such as insulators. Additionally, pure materials with high atomic number have a reduced interaction depth with the beam which can be overcome by increasing the electron beam energy[94]. The scattering intensity and area are important considerations for imaging and depend on the beam energy and sample thickness. A higher electron beam energy will have a larger interaction depth and provide more scattering collisions in addition to a larger scattering area. Thin samples will have smaller scattering area due to increased electron transmission through the sample.

There are two main types of scattered electrons during SEM imaging: secondary electrons (SE) and back scattered electrons (BSE). Secondary electrons are produced by inelastic collisions within the specimen at shallow depths. These secondary electrons have low energy (0.5 – 5 eV) [94]. Back scattered electrons come from deeper in the sample and are the product of several elastic collisions. Back scattered electrons have high energies, close to that of the initial electron beam. Separate electron detectors are used for each type of scattered electron. The back scattered electron detector sits below the objective lens with an opening the center. The BSE detector is typically a silicon pn junction. The secondary electron detector has a positive charge that attracts scattered electrons. Accelerated secondary electrons strike the detector and produce photons that travel through a “light pipe” onto a photomultiplier tube which converts the photons into electrical signals. The scattered electrons incident onto the detectors have varying intensity

based on their exit angle from the specimen. These changes in intensity are recorded as variation in contrast to produce the final SEM image.

2.2.3 Dynamic Mechanical Analysis

Dynamic Mechanical Analysis is a technique used to measure the stress-strain response of materials. Measurements can be carried out with temperature variations, under humidity conditions, or even submersed in a fluid environment. In most DMA instruments there are numerous testing clamps that can be attached so that mechanical testing can be done under tension, compression, 3 point bend or shear. For this work, free-standing metal matrix composites were tested in tension using the TA Instruments DMA Q800.

The DMA operates by applying a sinusoidal force (stress) to the sample and measuring the resulting displacement (strain). The sinusoidal force is applied to the sample via a non-contact linear drive motor. A sinusoidal response is measured, in addition to the phase shift of the two curves. The phase shift contains viscoelastic information about the material. The phase shift aspect of DMA is not of large importance for this work. Strain is measured using an optical encoder with a strain resolution of 1 nm [95]. The raw data provided by the instrument is force and displacement, stress (σ) and strain (ε) can then be calculated based on the dimensions of the sample:

$$\boldsymbol{\sigma} = \frac{\boldsymbol{F}}{\boldsymbol{A}} \frac{(\boldsymbol{force})}{(\boldsymbol{cross\ sectional\ area})} \qquad \text{(Eq. 2-4)}$$

$$\boldsymbol{\varepsilon} = \frac{\boldsymbol{\Delta L}}{\boldsymbol{L}} \frac{(\boldsymbol{change\ in\ length})}{(\boldsymbol{initial\ length})} \qquad \text{(Eq. 2-5)}$$

From the resulting stress strain curve, material properties such as elastic modulus, fracture strain, modulus of toughness, and ultimate tensile stress can be extracted.

For DMA testing of free-standing films in Chapter 4, sample lengths were measured by the instrument after being mounted to the tension clamps. The thickness of the sample was set to the sum of the MMC silver layer thicknesses, measured by the metal evaporation instrument. The carbon nanotube layer is assumed to not contribute significantly to MMC thickness. The tension tests were performed by ramping the strain 0.05% per minute up to fracture at room temperature. In tension testing, the top clamp is fixed, and the force is applied to the bottom clamp. Each time a clamp is reinstalled on the machine it is calibrated by the instrument through weight and position calibrations. The instrument is also calibrated to a known test specimen. Although a sinusoidal force is applied throughout testing, for tension tests a static force is also applied that is larger than the sinusoidal force. This is to prevent buckling of the film [96]. Because these samples are only 4 μm thick, to measure the initial specimen length, it was necessary to manually weigh down the lower clamp to remove any visible slack. However, after the test began there was typically a small amount of residual slack remaining in the film. It was visually noted during the beginning of the test when the sample was in tension. The slack region of the raw data was removed by shifting the curve to the origin at the point of sample tension. It was also noted if the sample fractured in the center. As is common for stress testing of material samples, the free-standing films were fabricated in a dog-bone shape. This shape concentrates stress in the middle of the film during tension testing, promoting failure away from the sample clamps. If there was a fracture closer to the mounting paddles, it was likely due to a pre-existing notch or tear in the film and the results were invalidated. To give more insight into the cause of the fracture, optical microscope imaging was done on the edges of each

specimen prior to testing. Notes were made on the location of any large notches that may initiate fracture.

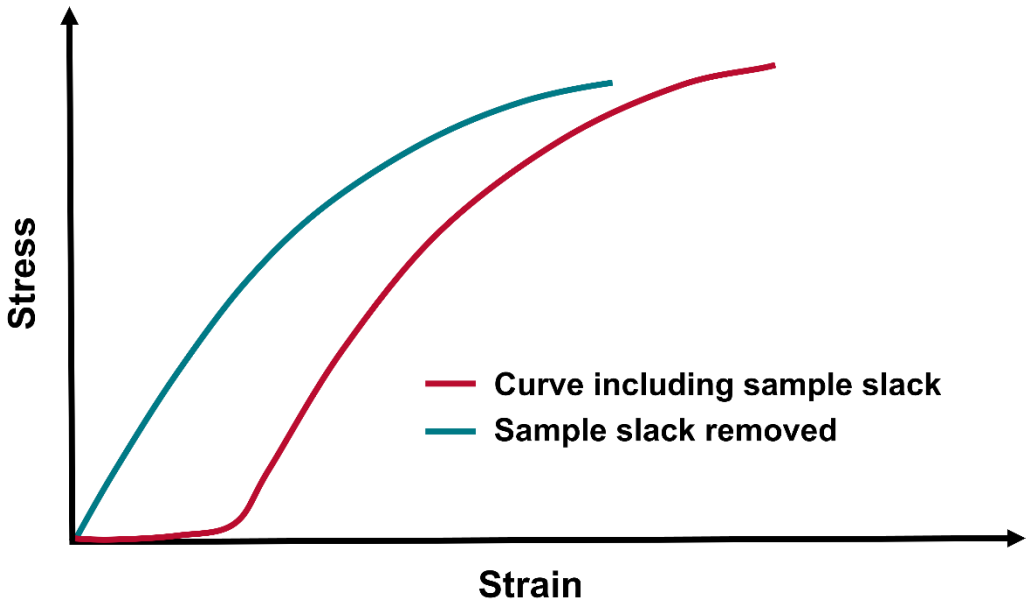

Figure 2.5 *Schematic illustrating a stress strain curve with sample slack compared to the shifted curve after the slack region is removed.*

CHAPTER 3: DEVICE-LEVEL PERFORMANCE EVALUATION OF METAL MATRIX COMPOSITES AS PHOTOVOLTAIC GRIDLINES

3.1 Fundamentals of Photovoltaic Devices

There's long been and continues to be interest in improving efficiency and longevity of solar cells. This work is focused on enhancements to device mechanical resilience that can lead to improved performance of the cell in the event of cell cracking. The work presented in this chapter aims to understand the impact of a metal matrix composite used as PV metallization.

Evolution of Photovoltaic Devices

The fundamental theory used in photovoltaic (PV) cells, the photovoltaic effect, was first observed in 1839 by Alexandre Edmond Becquerel [97]. The photovoltaic effect is an energy conversion mechanism, where photons are absorbed by a material via incident light and electrical energy is generated. The incident photons contain enough energy to

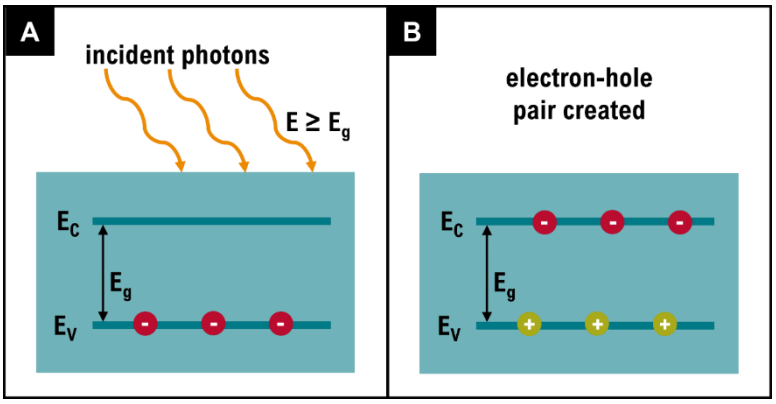

Figure 3.1 *Simplistic view of the photovoltaic effect. A.) Incident photons (sunlight) are absorbed by the material. B.) Photons with energies greater than the bandgap of the material excite electrons from the valence band (EV) into the conduction band (EC) creating an electron-hole pair.*

excite a carrier from a ground state to an excited state, during this process a free electron-hole pair is created able to generate current, see Figure 3.1.

Advances in the growth of single-crystalline silicon and a better understanding of the photovoltaic effect led to the first practical solar cell device, designed, and fabricated at Bell Labs in 1954 by *Chapin, et. Al*. [98]. This initial PV cell was a pn-junction made of silicon with a thin p-type layer on top of a thicker n-type base. The shallow penetration depth of sunlight required the junction to be near the surface of the device. At the time, a theoretical efficiency of 22% was predicted, considering that only incident light with energies matching the silicon bandgap would create free electron-hole pairs. However, further limitations to the device became obvious. The silicon surface was highly reflective, leaving only about half of the incident sunlight to absorb. Recombination of electron-hole pairs, surface resistances, and contact resistance all contributed to losses in the device.

The issue of surface recombination was addressed in 1957 by Mohamed M. Atalla at Bell Labs [99]. The surface of a semiconductor the crystal lattice is imperfect and dangling bonds exist with un-paired electrons. These dangling bonds introduce new energy levels that would otherwise be forbidden called surface states. The surface states act as recombination sites for electron-hole pairs, reducing the carrier concentration and ultimately leading to reduced efficiency in a PV cell [100]. Atalla initiated the field of surface passivation, in which a surface treatment is done to reduce surface recombination. Atalla's solution was a thin layer of silicon dioxide (SiO_2) thermally evaporated onto the silicon surface. SiO_2 is a dielectric with a wide bandgap compared to silicon. It passivates the silicon surface by providing atoms to bond with any dangling bonds. In addition to reducing losses due to surface recombination, subsequent work was done during this time

to optimize front metallization for current collection and distribution in a grid pattern [101–103]. The trade off in grid pattern optimization is shading of the cell due to reflection of the metallization versus the resistance of the metal contact with wider grid spacing. Work was also done to improve radiation resistance of PV devices for space applications [104] and increase efficiency leading to the launch of the first satellite (Vanguard 1, 1958) to use solar powered photovoltaic cells [105].

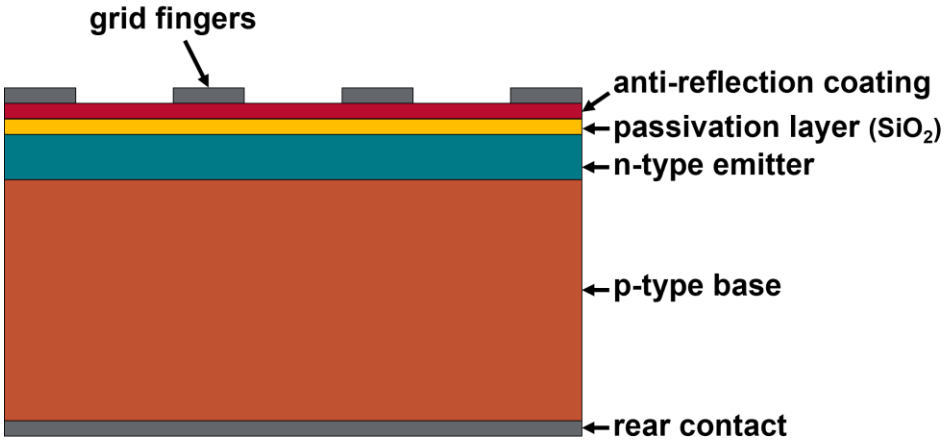

Figure 3.2 *Basic structure of single junction silicon solar cell*

The research area of photovoltaic devices has continued to grow from the earliest solar cells in the 1950s up to present day. Small solar cells were integrated into daily items like calculator and wristwatches. Research into PV device materials and structure expanded. By 1986, the efficiency of silicon PV had increased to 20% by improvements of surface passivation [106]. In the early 1990s concentrator solar cells were gaining attention. Concentrator solar cells use optics to focus the sunlight onto a smaller cell and generate higher efficiencies. A remarkable efficiency of nearly 41% was obtained in 2008 using a concentrated inverted metamorphic (IMM) triple junction cell [107]. Today there are many different categories and materials used in PV fabrication. The highest efficiencies are still coming from multijunction IMM cells. Silicon is the traditional (and

more cost effective) material used for PV. It currently holds a maximum efficiency of about 26% [108].

Photovoltaic Device Structure

The pn-junction is the basis for photovoltaic cells. In silicon cells, the negatively doped n-type silicon is typically near the top of the cell, referred to as the emitter. The positively doped p-type silicon is underneath, referred to as the base. The emitter is much thinner than the base so that the junction is near the surface of the device for better collection of free carriers by the cell metallization. Incident photons with the same energy as the bandgap of the PV material (E_g = 1.12 eV for silicon) create an electron-hole pair. The pn-junction separates the electron and hole to allow for conduction when an external load is applied. The SiO_2 passivation layer is applied over the pn-junction.

The pn- junction is the semiconductor component of the PV device responsible for converting sunlight into electron-hole pairs. Metal contacts are applied to the front and back of the pn-junction to allow for collection of the electrons and provide current to an external load. The front contacts are typically in an array of thin metal strips distributed vertically across the cell, referred to as gridlines, and connected to a slightly thicker horizontal strips referred to as a busbar. The back contact is typically a full layer of either silver or aluminum or a combination, covering the entire back surface of the cell. PV metallization is commonly applied using electroplating, metal evaporation, or screen printing. Electroplating and metal evaporation have been discussed in Chapter 2. In screen printing, a silver paste is used as the ink and a stencil with the desired gridline or metallization pattern is used to place the gridlines directly onto the device. The silver paste is then fired to lock the gridlines in place. A surface treatment is done to the top of the cell

to minimize reflections. Commonly, an anti-reflection coating (ARC) layer is applied. This optical layer is designed with a certain thickness and refractive index so that light reflected from the semiconductor surface destructively interferes with light reflected from the ARC layer. The basic structure of a single junction silicon cell is shown in Figure 3.2.

The triple junction solar cell follows the same basic structure as the conventional silicon cell but has three pn-junctions opposed to one to take advantage of a broader photon spectrum. The bottom layer is a germanium junction (E_g = 0.67 eV), the middle layer is a $In_{0.02}Ga_{0.98}As$ junction (E_g = 1.39 eV), and the top layer is a $In_{0.5}Ga_{0.5}P$ junction (E_g = 1.86 eV). The alloy compositions were chosen to best lattice match that of germanium[107]. The advantage of the triple junction is that multiple bandgap energies of light can create free carriers within the device, capturing incident light that would otherwise be lost in a single silicon junction.

Fundamentals of PV Operation

Absorption of incident photons with energies greater than the bandgap of the semiconductor used in the PV device create electron hole pairs within the semiconductor material. Photons with energies smaller than the bandgap do not generate carriers and are considered a loss from the perspective of utilized incident sunlight. Photons with energies larger than the bandgap create electron-hole pairs, but the electrons typically thermalize back to the conduction band before they are collected [109]. The electric field created at the junction of the pn-junction sweeps electrons into the n-type region and holes into the p-type region. The electrons can then be collected by the gridlines. Once the front and back contacts are connected to each other, current flows through the circuit through a resistive load.

The equivalent circuit that describes the electrical operation of a solar cell can be viewed as a current source in parallel with a diode. To further the model accuracy, resistors are added in both series and parallel to the current source to account for parasitic effects within the device. The current source is viewed as the light-generated current, I_L which is the maximum possible current the cell can provide. The diode represents the pn-junction that is critical to the device's operation by separating generated electron hole pairs from incident photons to generate a current. The resistor in parallel to the current source is the shunt resistance, R_{sh}. This resistance is viewed as an alternative current path due to defects within the device therefore a high shunt resistance is desired signifying low current leakage. The resistor in series with the current source is referred to as the series resistance, R_s. This resistance is generated from contact resistances at the metal/semiconductor interface and the flow of current through the semiconductor regions of the device. To optimize the power obtained from the cell, in real-world devices it is desirable for the series resistance to be as low as possible. This equivalent circuit and the IV curve of a PV device can be described using the following equation:

$$\boldsymbol{I = I_L - I_0\left[\frac{q(V+IR_s)}{nkT}\right] - \frac{V+IR_s}{R_{sh}}} \qquad \text{(Eq. 3-1)}$$

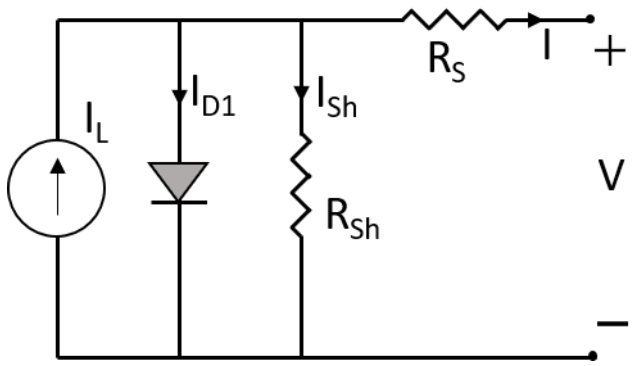

Figure 3.3 *Equivalent circuit of photovoltaic device using the single diode model*

The term I_0 represents the saturation current which is related to the current that flows under no illumination due to thermally generated carriers, the value is dependent on recombination effects within the device. The term *n* is the ideality factor and indicates how closely the cell follows the ideal diode equation. An ideality factor of $n = 1$ would be

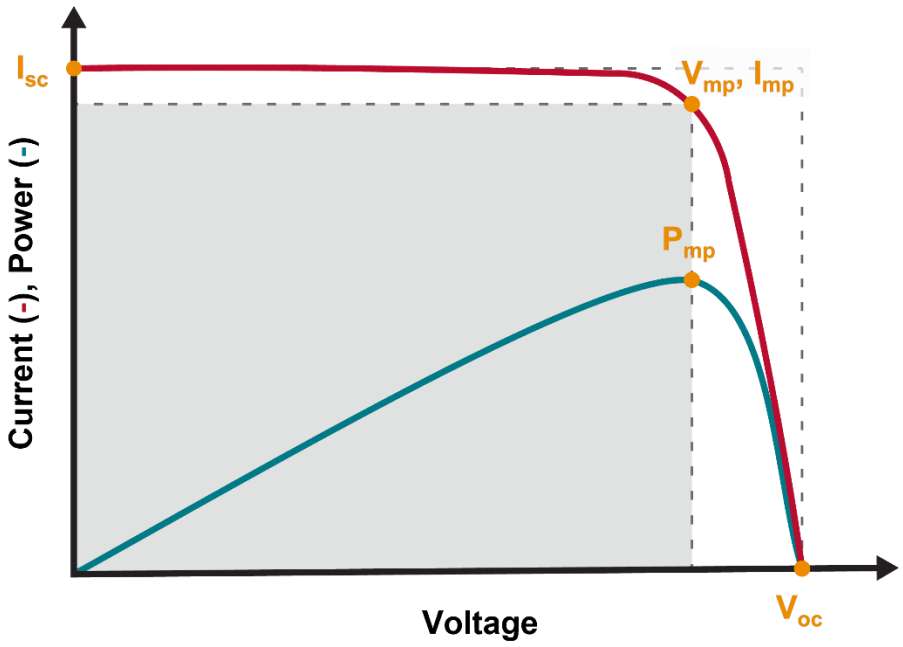

Figure 3.4 *LIV curve of a PV device (-). The power curve (-) is the integral of LIV curve. The shaded region represents the fill factor (FF)*

exactly following the ideal diode equation and anything larger indicates losses due to recombination effects. The constants in the IV equation are *q*, the electron charge, *k*, the Boltzmann constant, and *T* the operating temperature. The term *kT/q* is the thermal voltage and $V_T = 0.026\ eV$ at room temperature $(T = 300\ K)$.

Figure 3.4 shows the shape of the IV response for a photovoltaic device. The short circuit current, I_{sc} is the current when there is zero voltage across the cell and is equivalent to the light generated current, I_L under ideal conditions ($I_{sc} = I_L$). The V_{oc} is the open-circuit voltage or the voltage when there is no current, this is the maximum voltage of the cell.

The V_{oc} is dependent on I_0, and therefore is affected by recombination effects within the cell. The squareness of the curve is referred to as the fill factor, *FF*, and is a measure of the cell's maximum power. The fill factor is a ratio of the maximum power (P_{mp}) and the product of I_{sc} and V_{oc}. The maximum power of the cell is found by taking the derivative of the IV curve and locating the maximum. The fill factor is used to calculate the efficiency of the cell which is the ratio of output power over input power from the sun. The standard value for input power density from the sun is $P_{in} = 100\ mW/cm^2$. The equations for fill factor (*FF*) and efficiency (η) are as follows:

$$\boldsymbol{FF = \frac{P_{mp}}{V_{oc}I_{sc}} = \frac{V_{mp}I_{mp}}{V_{oc}I_{sc}}} \qquad \text{(Eq. 3-2)}$$

$$\boldsymbol{\eta = \frac{P_{mp}}{P_{in}} = \frac{V_{oc}I_{sc}FF}{P_{in}}} \qquad \text{(Eq. 3-3)}$$

3.2 Metal Matrix Composite Integration onto Photovoltaic Gridlines

Microcracks in PV devices can occur within the brittle semiconductor due to mechanical stresses. Not only do cracks cause defects and recombination issues, they can also damage the metallization of the device, preventing current flow through the cell and reducing the power output of the module [3, 10–13, 110–116]. With the improved tensile and electrical properties of CNTs[22, 24, 56, 67, 117–121], it is hypothesized that CNTs are capable of bridging microcracks across PV gridlines thus maintaining current across a cracked silver gridline. To investigate the influence of CNTs embedded in metal gridlines, a carbon nanotube metal matrix composite (MMC) was integrated onto existing metallization of triple junction (TJ) cells. Cracks were introduced into the cells to study the ability of the CNTs to maintain current across cracks. Both control TJ cells with no

CNT incorporation and cells with MMC incorporation were tested under solar simulation. Electroluminescence imaging was used to visually inspect the impact of cell cracking. The LIV curves provided by solar simulation were analyzed and fit to the single diode equation (Eq. 3.1), describing the electrical performance of the TJ cell, to examine the individual performance parameters of control cell and MMC cells before and after introducing cracks.

The metal matrix composite (MMC) is integrated onto the existing gridlines of 2 cm x 2 cm *SolAero ZTJ* triple-junction PV cells. The *ZTJ* cell uses the traditional triple junction structure of Ge/InGaAs/InGaP from top to bottom on a germanium substrate [122]. The silver gridlines are 30 µm wide with 750 µm spacing and 4 µm thick. The MMC is applied in a layer-by-layer structure with the CNTs sandwiched between layers of silver. The initial layer of silver is electroplated onto a seed layer of metal evaporated silver, followed by carbon nanotube (CNT) spray coating and a final layer of electroplated

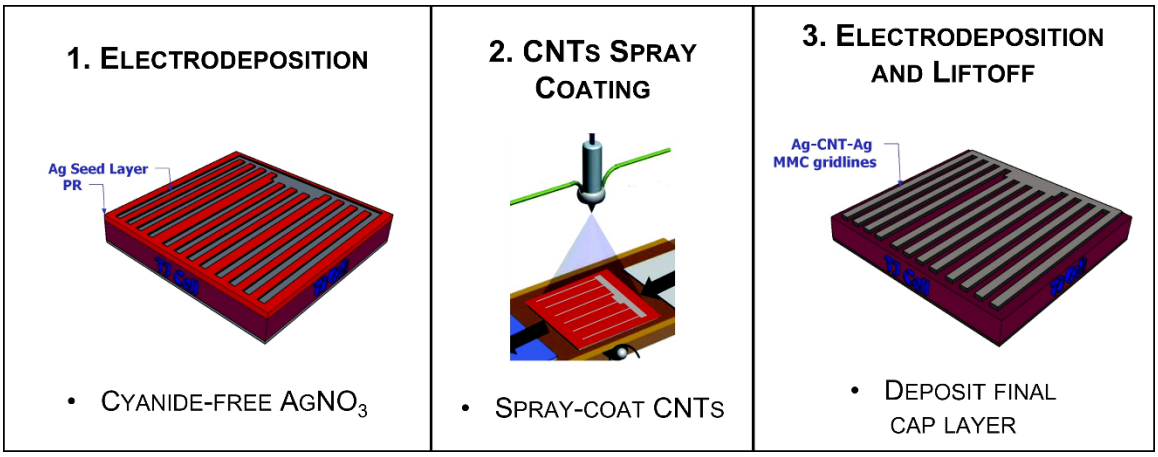

Figure 3.5 *MMC gridline fabrication process [142]*

silver. Silver electroplating was done at a current density of 9 mA/cm^2, which was chosen because it gave the brightest finish indicating higher quality silver [74]. A pre-made plating solution was used, E-brite 50/50 RTP which was chosen for its low toxicity compared to traditional cyanide-based plating solutions. The first layer of silver is approximately 3 µm

thick and the final is approximately 1 μm thick. An aqueous CNT solution with a concentration of 1.3g/L was spray-coated with the air brush nozzle onto the cell under a heated stage allowing for rapid evaporation of the solution. The CNTs used are low-cost, low-purity multi-walled CNTs (MWCNT). The MWCNTs are functionalized with COOH for a negative surface charge to produce a stable aqueous solution with better adhesion to the silver layer [74].

Solar simulation is used to obtain LIV (light current-voltage) curves for both control cells and MMC-integrated cells before and after introducing cracks. Cracks are introduced by placing the cell over a curved surface with radius of curvature r = 6 cm and applying an external load across the surface of the cell. An X-25 solar simulator (Mark II, SpectroLab Inc.) using AM0 spectrum is used for LIV testing. AM0 (air-mass 0) is the sunlight spectrum used for space applications. There is also a standard spectrum used for terrestrial applications (AM1.5), that is modified to include irradiance attenuations due to atmospheric effects. A lamp with the standard one-sun illumination intensity of 100

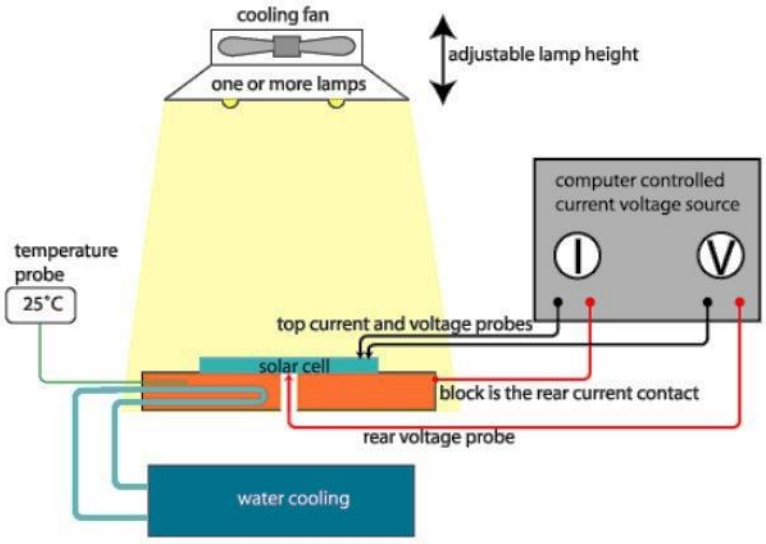

Figure 3.6 *General structure of an IV (solar simulation) test setup [144]*

mW/cm^2 is used to irradiate the sample and the current voltage response is measured. Figure 3.6 shows the basic setup of solar simulation testing.

Electroluminescence (EL) provides a visual electrical characterization of the cells before and after cracking, and is a standard tool for PV device characterization [3, 123, 124]. EL measurements are done by forward biasing the cells at 30 mA (~ 7.5 mA/cm^2). The top subcell (GaInP) emits photons in the visible region at 683 nm under forward bias and can therefore be captured with traditional photography. The EL response of this top subcell provides visualization of electrical disconnection across gridlines due to cracks introduced in the cell, an example is shown in Figure 3.7.

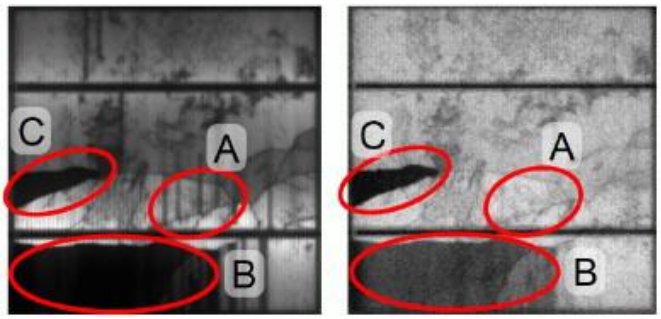

Figure 3.7 *Example of cracks indicated using electroluminescence. The dark areas represent electrical disconnections due to cracks. [3]*

3.3 Device Level Electrical Performance Analysis

LIV Curve Results & Discussion

The EL images of the control set of PV cells (Figure 3.8 inset) show large dark regions of the top cell after cracking. Dark regions are areas of the cell that are inactive indicating no electrical conduction and significant power loss. The *LIV* curves of the control samples are shown in Figure 3.8. The short circuit current (I_{sc}) shows a maximum

and average loss of 55% and 31% respectively after cracking compared to pre-crack. This indicates that as much as half the current that the cell is capable of producing has been lost due to cell cracking. The open circuit voltage (V_{oc}) is subtly impacted with maximum and average losses of 9% and 5%. This could be due to the lowered light current generated by cracked cells, or due to a low shunt resistance in the cell caused by current leakage and defects near cracks. Fill factor (*FF*) has a maximum degradation of 34% and average of 31% after cracks are introduced. The reduction in I_{sc}, V_{oc}, and maximum power contribute to the decline in fill factor. Efficiency (η) is dependent on the fill factor, I_{sc}, V_{oc}, and shows the largest deterioration of these four parameters. For control samples, the observed maximum percent decrease in efficiency post-crack is 67% with an average of 52%.

Figure 3.9 shows the *LIV* curves of the cells with MMC gridlines. In the EL images, cracks appear as bright regions opposed to the dark inactive regions of the control cells. This indicates current is being conducted across the entire cell despite the cracks. The I_{sc} of cracked MMC cells confirms that current is maintained across cracks. The maximum degradation of I_{sc} is only 1% for MMC cells, compared to 55% of control cells. The V_{oc} of the MMC cells shows similar small losses to that of the control after cracking around 5% - 10%. The bright spots near the cracks of the MMC suggest regions of higher current than the surrounding area, thus potential current leakage. Current leakage would reduce the

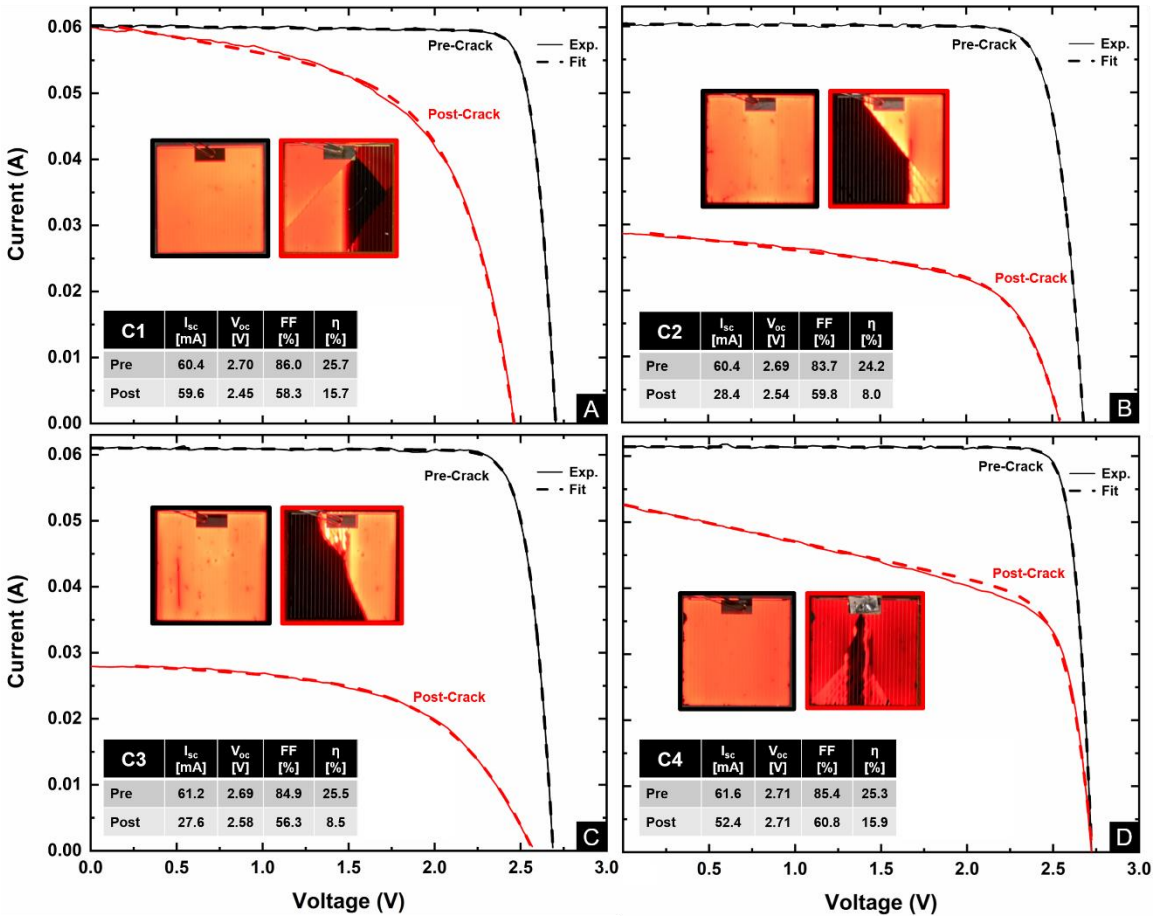

Figure 3.8 *EL images and LIV curves before and after cracking of four control cells*

shunt resistance and lower the V_{oc}. The fill factor improved for cracked cells with MMC gridlines compared to control. The average degradation in fill factor for cracked MMC cells was 16% compared to 31% for control cells. The efficiency degradation improved from 52% in control cells to 21% in MMC cells. This indicates increased performance in maintaining maximum power with MMC gridlines in the event of microcracks in the PV device.

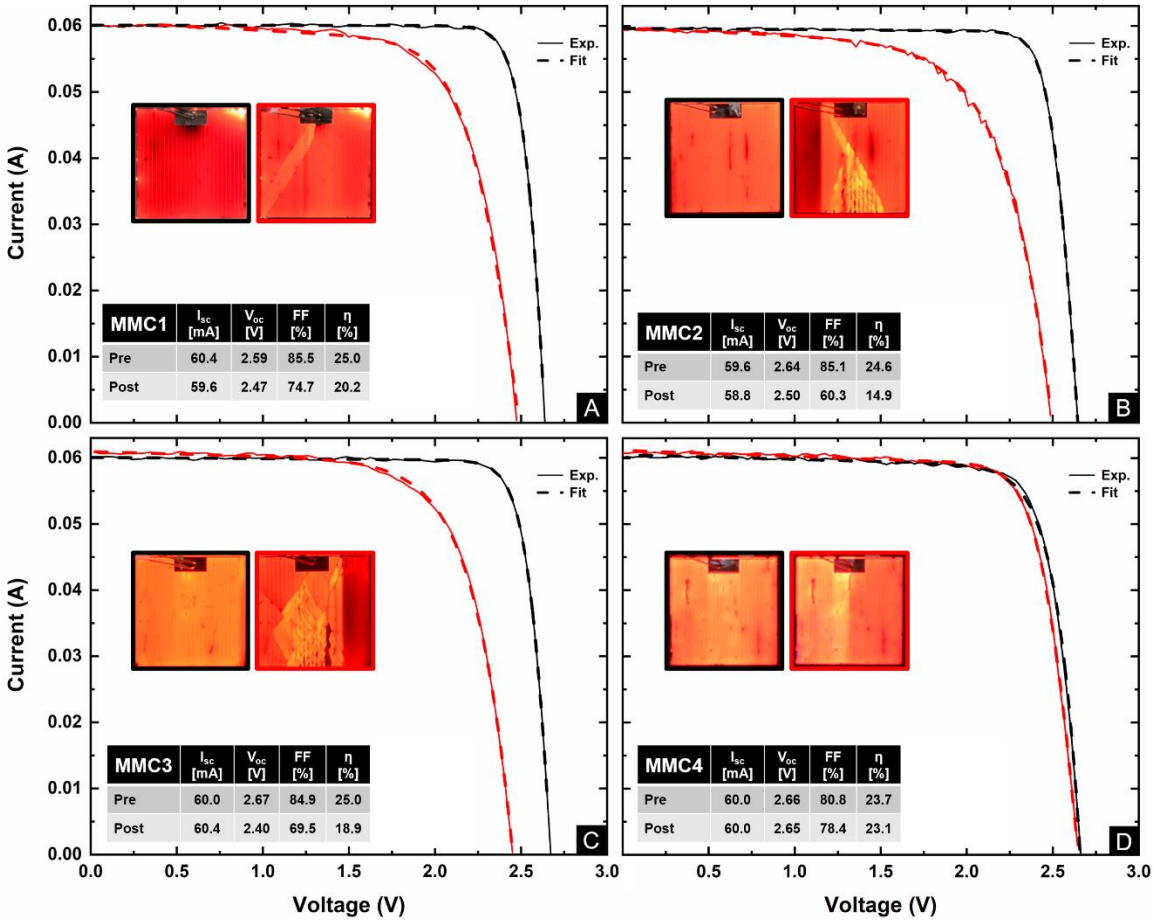

Figure 3.9 *EL images and LIV curves of cells with MMC integrated metallization*

Equivalent Circuit Analysis

Each of the *LIV* curves were fit to the single diode equation (Eq. 3-1) to extract the performance parameters I_0, I_L, n, R_s, *and* R_{sh} and compare values of control and MMC cells before and after introducing cracks. The fits were done in MATLAB using a nonlinear least squares solver function (`lsqnonlin`). The average and standard deviation of the output fit values for each parameter are shown in Figure 3.10. The averages were taken for the four cells in each data set; control pre-crack, control post-crack, MMC pre crack, and MMC post crack.

The saturation current I_0 is sensitive to recombination effects and is indicative of material quality. The value can be thought of as a leakage current, therefore a smaller value is desired. Even if current is maintained throughout the gridlines, any cracking will inevitably cause defects and cause an increase in saturation current. This is the case for both the control and MMC cells. All cells in the test have a pre-crack saturation current on the order of magnitude of 10^{-12}, the MMC value is slightly higher. However, ΔI_0 from pre-crack to post-crack is smaller for the MMC cell compared to the control cell, indicating less current leakage after cracking within the MMC cell.

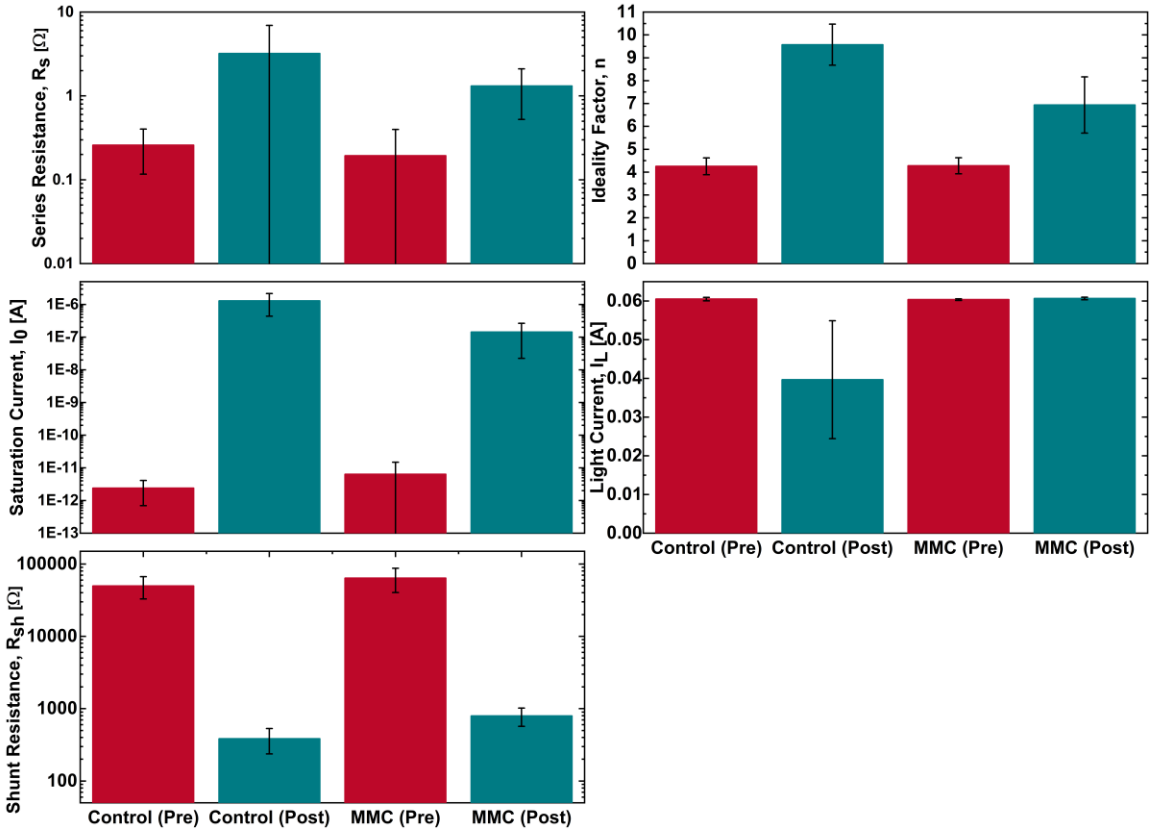

Figure 3.10 *Average and standard deviation of LIV performance parameters for control and MMC cells before and after cracking*

The light current I_L, which is equivalent to the short circuit current I_{sc}, is the most current that can be generated and collected by the cell. When gridlines are fractured to the

point of no longer being able to carry current, I_L of the cell is reduced. On average there is a 31% reduction in I_L after cracking for the control cells. The cells with MMC gridlines show a 1% reduction after cracking, indicating that current is being maintained across cracks.

The ideality factor n is an indicator of how closely the single-diode equation follows the ideal diode equation and is an indicator for types and severity of recombination effects. The control and MMC cells have similar ideality factor values before cracking. The Δn value is greater for the control samples, again indicating a smaller performance loss for cells with the MMC gridlines, showing fewer recombination losses after cracking.

Like saturation current, shunt resistance R_{sh} is impacted by material defects and leakage current. A large value of shunt resistance is desired for optimal device performance. In the PV cell equivalent circuit (Figure 3.3) it can be seen that a large shunt resistance would indicate a smaller leakage current. The values for the control and MMC cell's shunt resistance are similar both before and after cracking. It is likely that any presence of cracking would cause a large drop in shunt resistance due to the large amounts of defects introduced. Series resistance arise largely from contact resistances from the multiple layers of the PV cell, and a small value is desirable. The ΔR_s from pre-crack to post-crack in the MMC cells is half that of the control cell. For all five single-diode equation parameters, the MMC cells performed better than the control cells after cracks were introduced in this dataset.

3.4 Conclusion

The metal matrix composite (MMC) was integrated onto existing triple-junction (TJ) solar cells and tested using solar simulation before and after introducing cracks. The control solar cells with no MMC integration showed large degradation in all PV performance parameters after cracking, most notably an average decrease of 31% in short circuit current density. Cells with MMC integration maintained short circuit current density indicating a stable electrical connection across gridlines after cracking.

An analytical analysis of the LIV curves for control and MMC cells before and after cracking using the single-diode equation for PV cells was done. The introduced cracks were random in severity and location which could have led to a wide range of performance parameters extracted from the single diode fit. However, the analytical analysis does show a smaller delta for the cells with MMC integrated gridlines after cracking for all five performance parameters (I_0, I_L, n, R_s, R_{sh}) showed. That in combination with the fact that cracked MMC cells were able to maintain short circuit current density indicate, at least qualitatively, the potential for CNTs within traditional metal PV gridlines to provide electrical redundancy and a more resilient solar cell.

CHAPTER 4: MMC FABRICATION & MECHANICAL CHARACTERIZATION

4.1 Nanoindentation: Sample Preparation and Results

MMC Sample Preparation for Nanoindentation Testing

Metal matrix composites with a layer-by-layer (Ag/CNT/Ag) structure were fabricated on top of a GaAs substrate for nanoindentation testing. First, a thin seeding layer of silver was applied to the GaAs substrate using e-beam metal evaporation. Next silver was electroplated onto the seeding layer. The baseline set of samples were two layers of electroplated silver, with no carbon nanotube (CNT) incorporation. To explore the impact of electroplating current density, a range of baseline samples were fabricated with a current density ranging from 1.5 – 5.0 mA/cm^2. Dendritic silver growth was observed for films plated with current densities over 5 mA/cm^2 [75]. In the 1.5 – 5.0 mA/cm^2 range, lower current densities led to porous films while the higher current densities provided a denser film seen in the SEM images of Figure 4.1.

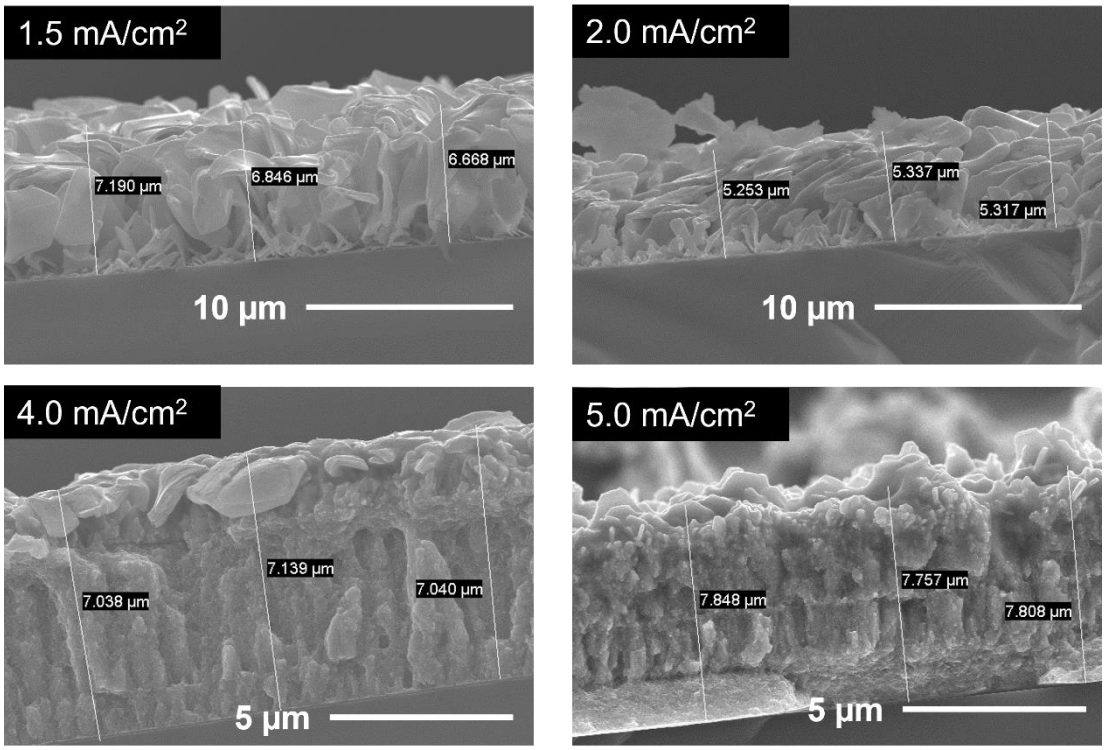

Figure 4.1 *Scanning electron microscope images for baseline Ag film with varying cathode current density.*

At this stage of this work, carbon nanotube spray coating was not yet the standard for MMC fabrication in our research group. Therefore, CNTs were deposited using two methods, 1) drop casting and 2) nano spreading. In the drop casting method, an aqueous solution of CNTs with a concentration of 1.3g/L are pipetted onto the sample on a heated substrate. The solution evaporates leaving behind the CNTs. The nano spreading technique is similar, with the added step of dragging a thin Teflon blade at an angle of 23° with respect to the substrate to distribute the solution more evenly. The blade is attached to a linear stepper motor and drags the meniscus of a droplet of the CNT solution at a constant velocity in the range of 15 µm/s. [125] The same CNT concentration of 1.3g/L was used for nano spreading. The drop casting method is very simple and fast but allows agglomerations to form while the solution evaporates leaving a non-uniform CNT

distribution. The nano spreader technique provided a more homogeneous distribution of CNTs, but with the small blade velocity was very time consuming.

After the CNTs are deposited and the solution has evaporated, a second layer of silver is electroplated. Each silver layer is approximately 3.5 µm, for a total sample thickness of 7 µm. The CNT layer is of negligible thickness compared to the silver layers. The specimen structure is shown in Figure 4.2.

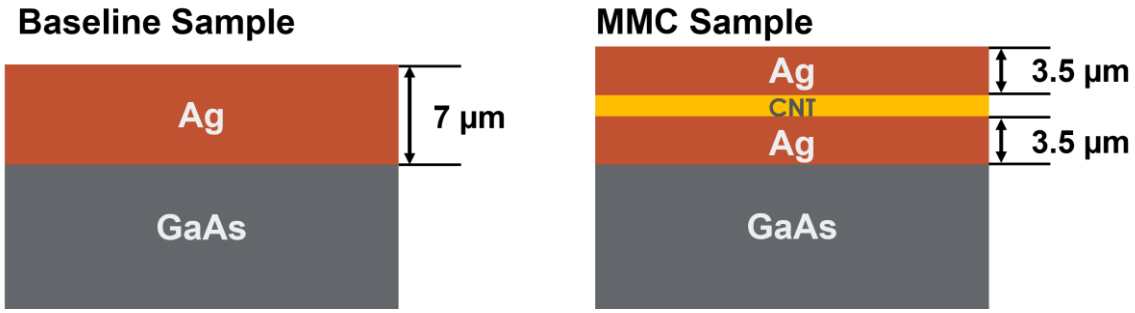

Figure 4.2 *Specimen structure for nanoindentation testing. Baseline Ag thickness is 7 µm, MMC layer-by-layer structure contains two layers of 3.5 µm thick Ag with a CNT layer of negligible thickness.*

Nanoindentation – Test Parameters

For most samples, 20 indentations were made in different locations. The indentations were spaced 75 µm in both the x and y directions. The indentations ramped up from a maximum depth of 300 nm to 1800 nm with a 60 second dwell time at the maximum load. The loading and unloading rate was the same at 1 mN/s. The indenter was a Berkovich (triangular) tip with a shape factor of 1.034.

The unloading curve fit provided the hardness *(H)* and reduced modulus *(E_r)* mechanical properties of the MMC, calculated as follows:

$$H = {P_{max}}/{A_s} \qquad \text{(Eq. 4-1)}$$

$$E_r = \sqrt{\pi}S \Big/ \beta 2\sqrt{A_s} \qquad \text{(Eq. 4-2)}$$

Hardness is calculated using the ratio of maximum load *(P_{max})* and contact surface area of the tip *(A_s)*. The reduced modulus is calculated using the stiffness *(S)* which is the slope of the unloading curve. The nanoindentation software does an automatic fitting of the unloading curve slope between 30% and 100% of the maximum load. The reduced modulus calculation is also a function of the indenter shape factor *(β)*, and the square root of the contact surface area of the tip *(A_s)*.

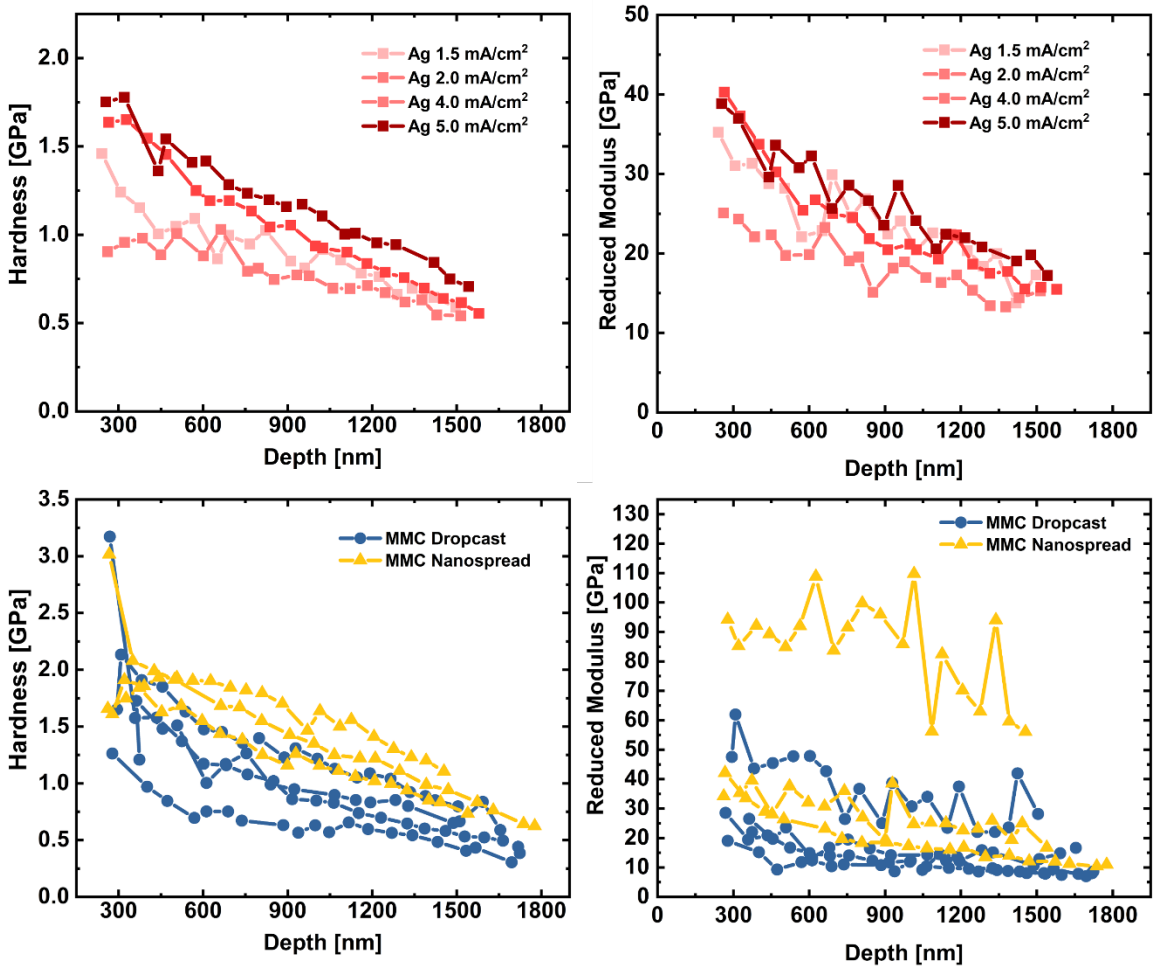

Figure 4.3 *Nanoindentation data of baseline silver and MMC with two deposition methods for CNTs, dropcast and nanospread.*

Nanoindentation – Results

Hardness and reduced modulus for the baseline silver samples are shown in Figure 4.3 (■) as a function of penetration depth. Each curve is for an individual sample with a unique current density, each data point is a single indentation at the given penetration depth. Each curve shows a decrease in hardness with increasing depth into the surface. This is a trend that is common in crystalline materials under nanoindentation testing and is attributed to the indentation size effect (ISE) [126–129]. It is possible that this trend is due to artifacts at the lower indentation depths. Several authors find that the contact area could be miscalculated due to pileup or sink in or due to blunting of the tip [93, 127, 130, 131]. A new indentation tip was used for these experiments with proper calibration to minimize the effects of tip blunting. Pileup is common in soft materials [132] and could be a factor for electroplated silver. According to finite element modeling on the impact of pileup, materials that have a ratio of the final penetration depth (h_f) to maximum penetration depth (h_{max}) of less than 0.7, pileup does not cause significant deviation in results [93]. For the results presented here, the h_f/h_{max} ratio was 0.55 on average. It is also possible that this trend is not due to measurement errors and is a true material behavior. The largely accepted physical explanation of ISE was first presented by *Nix and Gao (1998)*. Their model was based on geometrically necessary dislocations (GND) that are generated in the specimen near the indenter to accommodate the load imposed by the indenter tip [126]. These are in addition to the typically present dislocations referred to as statistically stored dislocations (SSD). These supplementary dislocations provide another hardening mechanism that is more prevalent at lower indentation depths. This explanation seems most likely to describe the hardness and indentation depth relationship present in our samples.

The average and standard deviation for baseline silver hardness and reduced elastic modulus are shown in Figure 4.4 as a function of current density. The MMCs were fabricated with a single current density, but the averages of each CNT deposition method are also shown for comparison. The baseline silver shows a gradual increase in the average hardness and elastic modulus with increased current density. This could be explained by the phenomenon of hydrogen embrittlement during electrodeposition [71]. Hydrogen is easily adsorbed into the metal deposit. The hydrogen molecules can interfere with metal deformation within the metal lattice or even accumulate in voids and create pressures higher than the metal's strength. Electroplated films in the reported current density range were annealed at 380°C for 5 minutes to outgas hydrogen and leave voids in the metal structure. SEM of the resulting cross sections show more voids present at lower current density (2-3 mA/cm^2) compared to the higher current densities up to 5 mA/cm^2. This is evidence that higher hydrogen incorporation at lower current densities has a negative impact on the hardness and reduced elastic modulus. In a separate experiment prior to

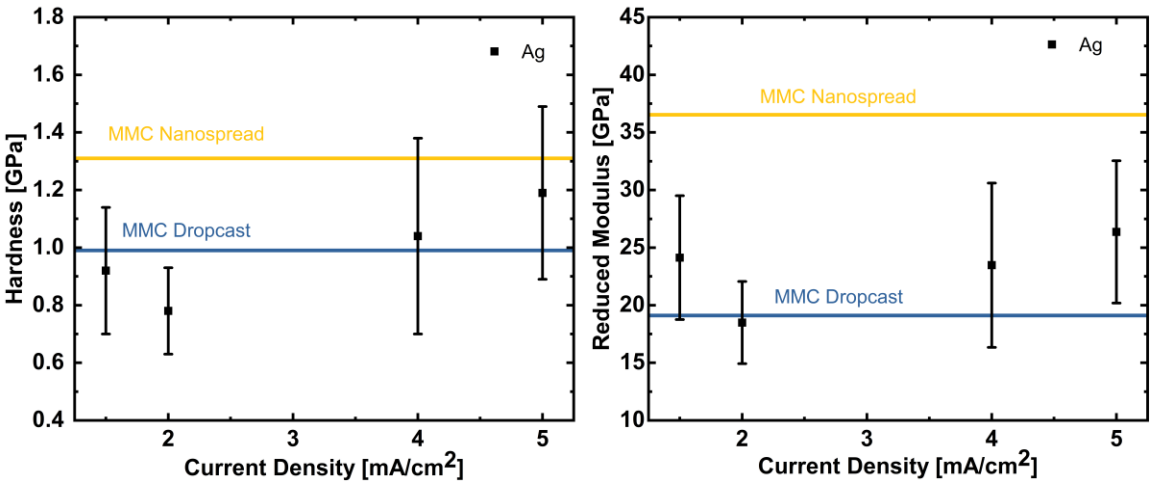

Figure 4.4 *Average hardness and reduced elastic modulus for two MMC datasets and Ag as function of electroplating current density.*

nanoindentation testing, the samples that gave the most reflective surface were electroplated with a current density of 3 mA/cm^2. A shiny, reflective silver surface is indicative of a higher quality electroplated film with low surface roughness [133], therefore the MMC samples fabricated for nanoindentation used a current density of 3 mA/cm^2.

The hardness and reduced modulus curves as a function of penetration depth for the MMC samples are shown in Figure 4.3 (▲,●). The decrease in mechanical properties as penetration depth increases also occurs for the MMC samples. The averages of both the dropcast and nanospread MMCs are plotted with the baseline silver averages in Figure 4.4 for comparison. The nano-spread deposition method seems to perform better than the drop cast samples, likely due to a more uniform distribution of CNTs obtain using the nanospreader.

Summary of Nanoindentation for MMC Mechanical Characterization

The data provided by nanoindentation gave some initial insight into how CNTs could enhance mechanical properties of silver films. It also gave evidence as to the importance of CNT dispersion. There are a few drawbacks for mechanical testing of a composite using nanoindentation. The highly localized nature of the measurements makes it difficult to understand how the entire composite behaves. A more representative mechanical response of the composite may be obtained using a spherical indenter tip opposed to Berkovich. With the Berkovich tip, it's possible that indentations could be made in regions of no carbon nanotube coverage due to the small indenter tip size. The sensitivity of the instrument made it analytically challenging to differentiate an experimental artifact from an instrumental error such as tip blunting, calibration error, surface roughness, or substrate effects. The CNT layer is extremely thin compared to the silver layer and outside of the

penetration depth, making it difficult to accurately capture CNT effects by a surface measurement technique. To obtain mechanical properties of the composite in tension with no substrate effects, a method of fabricating free-standing MMC films was explored.

4.2 Free-standing MMC Film Fabrication

Free-standing metal matrix composites (MMCs) were fabricated as a layer-by-layer structure with spray coated carbon nanotubes (CNTs) sandwiched between two layers of silver for mechanical testing, with no substrate effects, as a function of carbon nanotube content. A 3-D printed dog-bone shadow mask formed the shape of the composite structure, and focused stress in the center during tension testing. The dimensions of the dog-bone are based on work by *N.D. Cox*, et. Al [34]. The dog-bone structure is 28 mm long, with a 5mm x 5mm paddle at each end. The center of the structure is 2-mm wide and 6-mm long. There is a taper from each paddle to the center with a radius of curvature of 12.75 mm over a length of 6 mm. The dog-bone drawing was created using Autodesk Inventor computer-aided design software. The file was then printed using the Ultimaker Original+ 3D printer using a PLA filament. Each silver layer has a thickness of 2 μm. Silver layers are deposited using electron beam evaporation at a pressure of $2(10^{-6})$ Torr with an evaporation rate of 2.5 Å s^{-1}. Glass slides were used as deposition substrates for the MMC with the dog-bone mask adhered to each slide using double-sided adhesive tape. The low

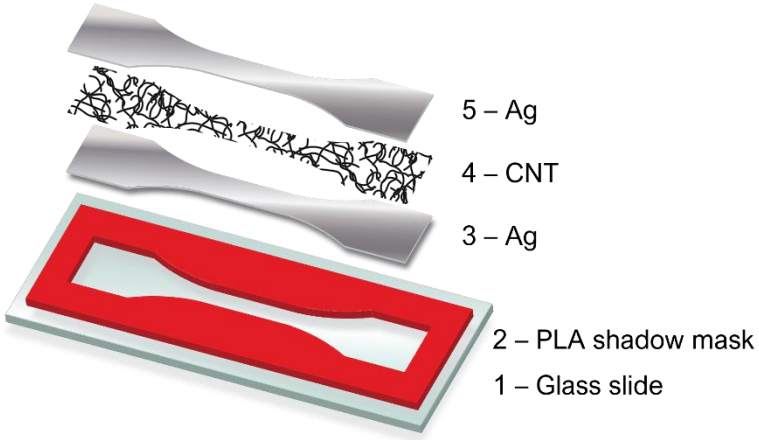

Figure 4.5 *Free-standing composite fabrication steps. Dog bone mask is attached to glass slide. First Ag layer is evaporated, followed by CNT spray deposition and final Ag layer.*

adhesion between glass and silver allows the composite to be peeled away from the substrate easily and measured as a free-standing film. Once the dog bone mask is carefully removed from the glass substrate, the MMC film is gently removed starting at each paddle.

Carbon Nanotube Spray Coating

Initial carbon nanotube spray coating was done with a low-cost option, a gravity feed high volume, low pressure (HVLP) industrial paint sprayer. Contrary to its name, it operates at a high pressure (around 30 GPa) from the perspective of CNT deposition applications. The drawback of this cost-effective option was the lack of control of flow rate and droplet size. These limitations led to large agglomerations and non-uniformity of the CNT distribution. Eventually a laboratory quality ultrasonic nozzle replaced the HVLP paint sprayer. The ultrasonic nozzle is powered by an ultrasonic generator and the solution is atomized by ultrasonic vibrations at the nozzle tip created by sound waves from the generator. The ultrasonic nozzle provided a more even distribution of the CNT solution with a predictable flow rate and smaller agglomerations. Even with improvements in the CNT spray coating equipment, CNT agglomerations proved to be an ever-present obstacle.

Three free-standing MMC film datasets were fabricated using spray coated CNTs for mechanical characterization using dynamic mechanical analysis (DMA) tension testing. *Dataset 1* was fabricated using the HVLP paint sprayer. *Datasets 2 and 3* were fabricated using the ultrasonic nozzle, but with varying spray coating parameters and CNTs. Table 4-1 summarizes the spray parameters of each dataset.

Table 4-1: *CNT spray coating parameters for each dataset.*

	Dataset 1	Dataset 2	Dataset 3
Spray Method	HVLP paint gun	Ultrasonic	Ultrasonic
Pressure	~30 psi	~5 psi	~5 psi
Nozzle Height	12 inches	3.5 inches	3.5 inches
CNT Concentration	0.007 % wt.	0.0007 % wt.	0.005 % wt.
Solvent *μ - viscosity* *σ - surf. tension* *ρ - density*	CHCl3 *μ = 0.542 mPa•s* *σ = 27 dyn/cm* *ρ = 1479 g/L*	DI water *μ = 1.0 mPa•s* *σ = 72 dyn/cm* *ρ = 1000 g/L*	Ethanol *μ = 0.983 mPa•s* *σ = 22 dyn/cm* *ρ = 789 g/L*
Temperature	~23 °C	~110 °C	~110 °C
Flow Rate	NA	0.3 mL/min	0.3 mL/min
Nozzle Speed	NA	1250 mm/min	1250 mm/min
MW or SW ***(Source)***	MWCNT *(CheapTubes.com)*	MWCNT 3.84% in DI H_2O *(Molecular Rebar)*	SWCNT 0.4% in ethanol/EGBEA *(Molecular Rebar)*
Diameter	8 - 15 nm	13 nm	1.5 - 2 nm
Length	*As received:* *10 – 20 μm* Actual ~ 2.5 μm	0.9 μm	2 - 10 μm
Functionalization	covalent *COOH pre-functionalized*	non-covalent *polyvinyl butyrate polymer wrapping*	non-covalent *polyvinyl butyrate polymer wrapping*

Fabrication Parameters of Dataset 1

CNT depositions of *Dataset 1* with the HVLP paint sprayer were done inside a fume hood at room temperature with the paint sprayer attached to a clamp stand. The distance from the nozzle of the sprayer to the sample was 12 inches. The sample was placed on a stationary, non-heated stage. The CNTs were in a solution of chloroform ($CHCl_3$) with a concentration of 0.1 g/L. The solution was mixed then sonicated for 90 minutes.

Chloroform was chosen for its low room temperature viscosity *(0.56 mPa•s)* and surface tension *(27.1 dyn/cm)* compared to water *(0.89 mPa•s and 72.0 dyn/cm respectively)* [134, 135]. Lower viscosity and surface tension lead to a smaller droplet size for spray coating applications [136], which is thought to reduce CNT agglomerations and enhance uniformity. The CNTs were low-cost, reduced purity to create an inexpensive MMC fabrication process. Dry multi-walled CNTs were bought directly from *CheapTubes.com*. These CNTs were grown using catalytic chemical vapor deposition, with a purity of at least 95% and ash content of 1.5%. They came pre-functionalized with a COOH (1.8%) functionalization to enhance adhesion to silver. Their diameters range from 3 – 5 nm with pre-spray lengths of 10 -20 μm. Based on SEM images of the CNTs after being spray coated with the HVLP paint sprayer, the lengths were reduced to approximately 2.5 μm. This is likely due to sonication of the $CHCl_3$/CNT solution. The flow rate of the HVLP sprayer could be altered but not with precise control. The flow valve was locked in a single position for each CNT deposition.

Fabrication Parameters of Dataset 2

The ultrasonic nozzle is a Sonaer Narrow Spray 130kHz ultrasonic atomizer nozzle with a Sonaer PinPoint Spray Shaper attachment and powered by the SONOZAP Ultrasonic Atomizer generator. The atomizer is mounted on a stepper motor to allow for linear translation over the sample stage with a set nozzle speed. The atomizer's liquid supply is controlled using a syringe pump. The atomizer also has a gas inlet for compressed air with a pressure of roughly 5 psi. Samples are placed on a heated stage (~110 °C) to accelerate evaporation of the solvent. Surface coverage of the CNT layer is varied by the number of atomizer translation cycles over the sample. The CNT concentration varies for

each of the two datasets deposited with the ultrasonic atomizer. Chloroform could not be used with the ultrasonic nozzle syringe pump tubing, therefore either DI water or ethanol was used as a solvent. Carbon nanotubes used with ultrasonic deposition were provided by *Molecular Rebar*. These CNTs are premixed with a predetermined solvent at a high concentration by the manufacturer for transport and are diluted in the lab to the desired concentration.

In *Dataset 2*, the nozzle to sample distance was 3.5 inches. The nozzle was placed at this distance from the sample to decrease losses from ambient effects. To reduce agglomerations of CNTs, the CNT concentration and flow rate were 0.007 g/L and 0.3 mL/min respectively. Multi-walled carbon nanotubes are provided by *Molecular Rebar* as a mixture of 3.84 wt% short CNTs in DI water with an average length of 900 nm and a diameter of 13 nm. The nozzle speed was set to 1250 mm/min (1.31 in/s). The frequency generator operated at a power of 40% (1.5 W).

Fabrication Parameters of Dataset 3

Long single walled CNTs were used in *Dataset 3* again provided by *Molecular Rebar*. They arrived as a 0.4% concentration in ethanol/EGBEA *(ethylene glycol butyl ether acetate)* and were further diluted to a concentration of 0.005% in ethanol. The long single walled CNTs had a diameter range of 1.5 – 2 nm and a length of 2 – 10 μm. The nozzle height, flow rate, power, and nozzle speed remained the same as *Dataset 2.*

4.3 CNT Quantification: Scanning Electron Microscopy and Image Analysis

During CNT spray coating, a sacrificial sample is coated along with the dog-bone structures for carbon nanotube content quantification. Scanning electron microscopy (SEM) is performed on the sacrificial samples to image and extract the CNT surface coverage without causing any damage to the MMC films to be mechanically tested. SEM is taken of the top view of the CNT layer and machine-learning driven image analysis is done to determine the CNT surface area coverage.

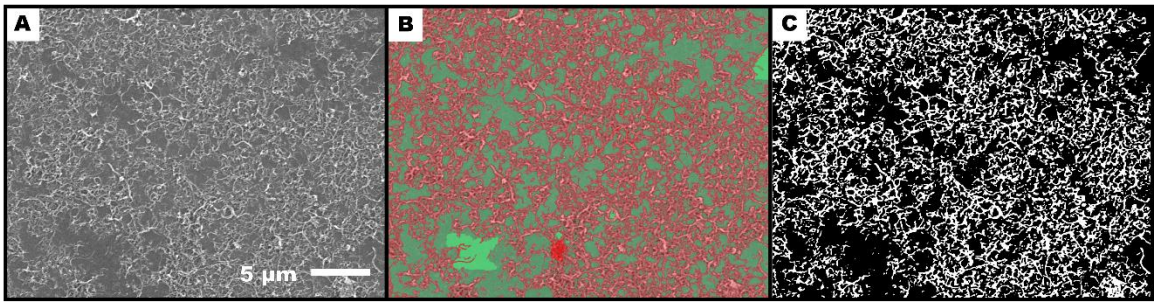

Figure 4.6 *Image analysis process for CNT surface coverage area determination. A) Original SEM image B) Classified image based on user selected regions (solid areas) C) Binary image used for CNT coverage area calculation.*

Image analysis is done using the FIJI (ImageJ) plugin "Trainable Weka Segmentation" trainer [137]. To train the machine learning model, the user manually selects and labels a few regions for each desired class, in this case a CNT class and a silver class. A machine learning algorithm then classifies the remainder of the image into one of the two classes. The final image can then be converted into a binary image of two grayscale values. The CNT surface coverage is then calculated as the ratio between the number of pixels from the CNT class and the total number of pixels. This process is shown in Figure 4.6.

SEM is done using a *"JEOL JSM-IT200 InTouchScope"*. The accelerating voltage was typically 15 – 20 kV with a photocurrent of 50% the maximum. Seven images of identical magnification from the sacrificial samples are captured. The magnifications varied slightly for each dataset but were typically around x3000 – x4000. The lowest and highest percentages were removed and the remaining five were averaged.

For the HVLP paint sprayer *(Dataset 1)*, the CNT content was varied by depositing for variable amounts of time. The HVLP paint sprayer did not produce repeatable CNT content for the same deposition times. This was due to subtle fluctuations in flow rate, even with the flow valve lock in place. The deposition time could also vary by a few seconds due to operator error of starting the timer and simultaneously beginning the deposition. However, the spray spot size of the HVLP sprayer was large enough to coat three dog bone samples at one time. The 3D printed masks were the same width as a glass slide and included three dog bone openings. Therefore, three samples with theoretically setup-invariant CNT content could be fabricated.

For the samples deposited with the ultrasonic nozzle *(Datasets 2 and 3)*, the controllable flowrate and translating nozzle allowed for a nearly repeatable CNT surface coverage using the same number of translation cycles. For ultrasonic deposition, dog bone samples were reduced to 1/3 the width of a glass slide. The combination of the small nozzle opening, reduced nozzle-to-sample distance, and the nature of linear translation provided a spray spot size the width of only one dog bone specimen. The width of the heated stage limited the number of samples that could be spray coated in one session to three. The number of nozzle translation cycles determined the CNT content per deposition session. Two sessions of deposition were done per number of translation cycles for a total of six

samples with the same number of spray coat cycles. At least one sacrificial sample was coated with each set, with the assumption that CNT coverage would be nearly identical for the entire set. Both sacrificial samples were imaged and analyzed as described above.

4.4 Tension Testing with Dynamic Mechanical Analysis

The mechanical properties for the CNT/Ag composites in free-standing configuration are obtained via tension testing using Dynamic Mechanical Analysis (DMA) with a *TA Instruments DMA Q800*. Samples are mounted to the instrument tension clamps with a torque of 3.5 inch-lb. The top clamp is fixed while the bottom clamp applies a strain rate of 0.05% per minute until the composite reaches failure. The innate design of the dog-bone structure enables an optimum failure point in the center of the loading direction due to the tapered shape of the deposited film. Mechanical testing is also done for pure silver films to be used as a baseline for composite comparison. The pure silver mechanical data is additionally used as material input data for finite element modeling of the composite.

Stress-strain curves are produced via DMA testing for each dog-bone specimen. Each CNT surface coverage has a sample set of 3 - 6 data points depending on the deposition setup. Four mechanical properties are extracted from each experimental stress-strain curve then averaged as a function of CNT surface coverage: elastic modulus, modulus of toughness, fracture strain, and ultimate tensile stress (UTS). Elastic modulus is calculated as the slope of initial linear region of the stress-strain curve, modulus of toughness is the area under the curve, fracture strain is the maximum strain value corresponding to sample failure, and UTS is the maximum stress value.

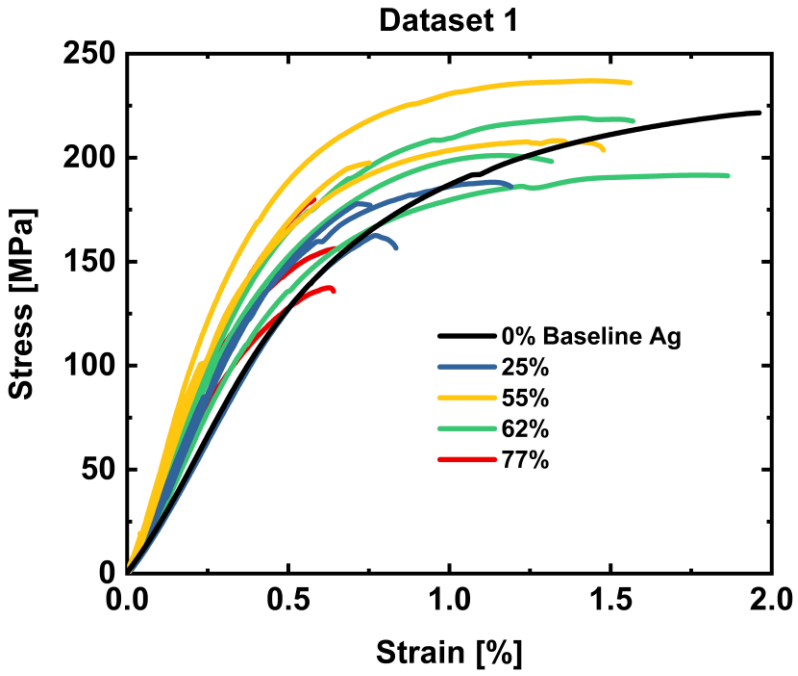

Figure 4.7 *Dataset 1: Stress-Strain curves from tension testing*

The elastic modulus is indicative of the material's stiffness and the ultimate tensile stress of the material's strength. Both properties are thought to increase with CNT incorporation compared to pure silver properties due to the large strength and stiffness of carbon nanotubes. In the mechanisms of load transfer from matrix to CNT, the elongation or fracture strain has been shown to decrease with CNT incorporation [29, 138] as the CNTs increase the material strength. However, in other layer-by-layer metal matrix composites, the fracture strain has increased with increased CNT loading [34]. This study also showed an increase in toughness with CNT content. However, at a certain CNT loading mechanical properties typically tend to drop off [34, 52–56]. This is typically attributed to agglomerations or the increase of weaker van der Waal interactions from the CNT side walls.

Analysis of Dataset 1

The stress strain curves of *Dataset 1* MMC thin films for 25%, 55%, 62%, and 77% surface area coverage of carbon nanotubes are shown in Figure 4.7. This set was spray coated with the high pressure HVLP paint gun. The CNT initial length was 10 -20 µm and reduced to approximately 2.5 µm during sonication. The CNTS were mixed into $CHCl_3$ for spray coating and sonicated for 90 minutes. For each of these surface coverages, three free-standing films were tested. Other surface coverages were fabricated for this dataset, but two of the three films either broke during mounting or broke near the paddles. This was also the case for the silver baseline samples, so only one stress-strain curve is presented. It is shown for comparison to the MMC samples but is less statistically relevant.

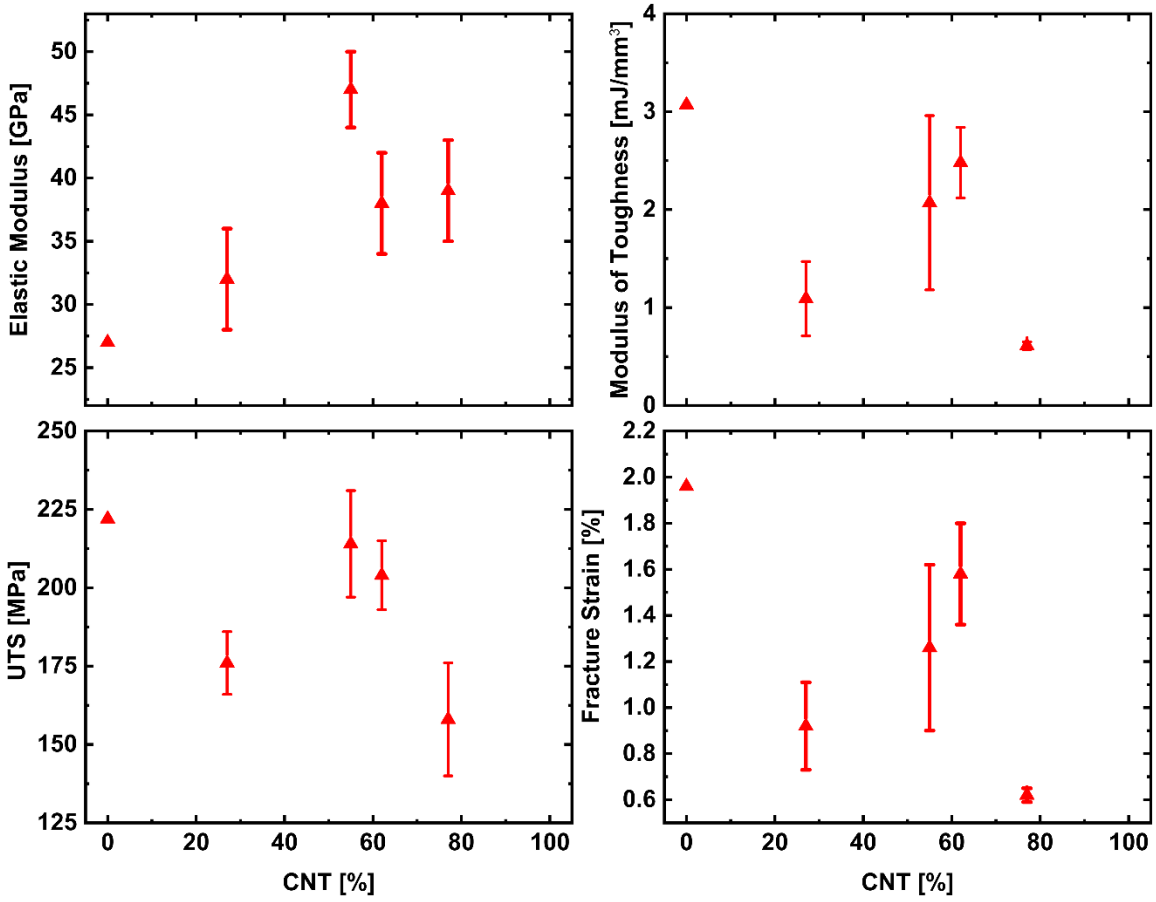

Figure 4.8 *Dataset 1: Mechanical parameters as a function of CNT surface coverage*

The four extracted mechanical properties for *Dataset 1* are shown in Figure 4.8. The elastic modulus is improved for all composites compared to the pure silver specimen, indicating increased stiffness from CNT incorporation. Fracture strain, toughness, and ultimate tensile stress (UTS) all have decreased properties compared to baseline silver. The modulus of toughness usually follows the same trend as the fracture strain since it is calculated as the area under the stress strain curve and fracture strain has more variability across specimens compared to the upper stress limits. The 55% and 62% surface coverages appear to have the superior properties off all the MMCs in *Dataset 1*. However, it is difficult to make any confident conclusions with this limited dataset.

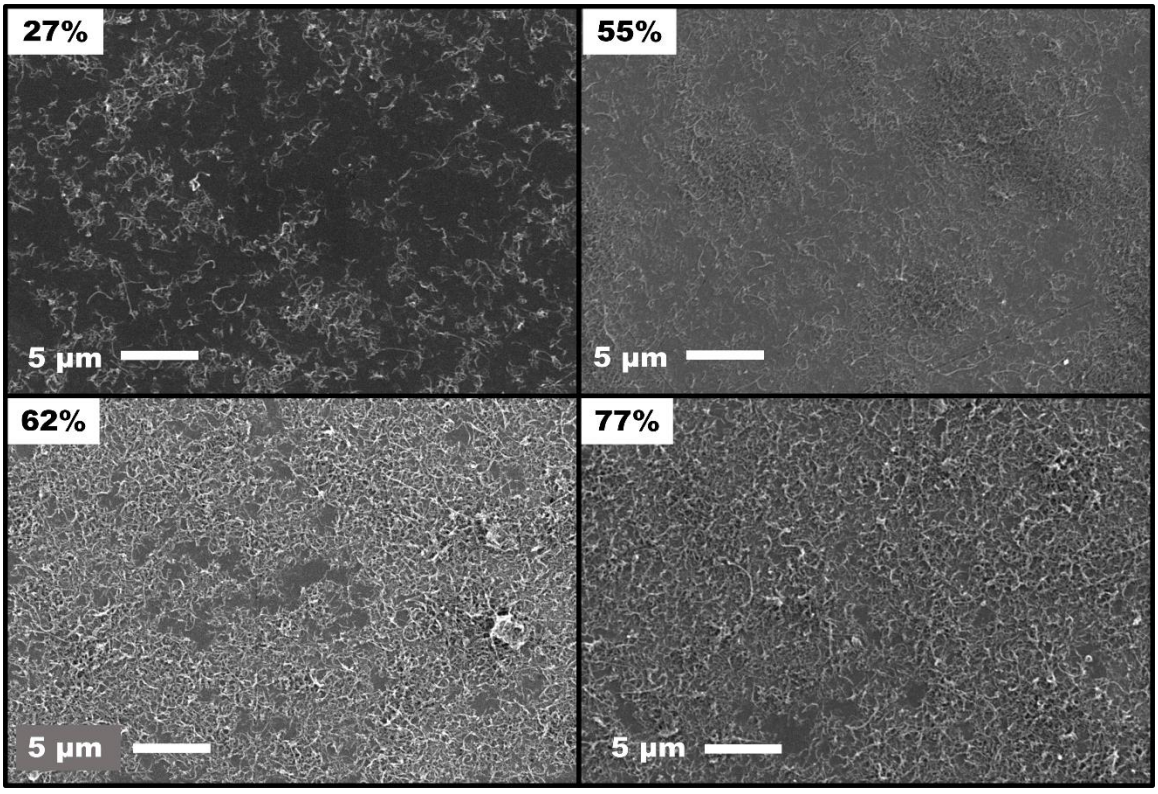

Figure 4.9 *Dataset 1: Top view SEM images of CNT layer for varying surface coverage*

The microstructure of these composites can be seen in Figures 4.9 and 4.10. At high magnifications under SEM (Fig 4.7), the CNTs appear to be well dispersed and evenly

distributed. However, lower magnification images (Fig 4.8) show large agglomerations on the surface with average diameters of 11 µm. The large agglomerations are likely the cause for reduced strength and potentially early fracture. Agglomerations prevent load transfer from CNT to matrix with the large concentration of CNT-CNT weak van der Waal interactions. Agglomerations can also act as crack initiation sites, and lead to a premature composite fracture as cracks near agglomerations propagate. Figure 4.10 illustrates how the agglomeration density increases at higher CNT loading, further weakening the composite.

From this data, there is evidence that the addition of CNTs for 55 – 62% surface coverage has an improved mechanical response compared to the lowest (25%) and highest (77%) coverages. The properties show the trends present in other CNT composite studies from literature showing an increase in strength with increasing CNT concentration until a decrease at larger surface coverage related to accumulation of agglomerates and increased CNT- CNT van der Waal interactions. There may be some enhanced stiffness from the areas of dispersed carbon nanotubes, but it seems the agglomerations reduce the strength and potentially cause early fracture compared to the baseline silver. This dataset provided

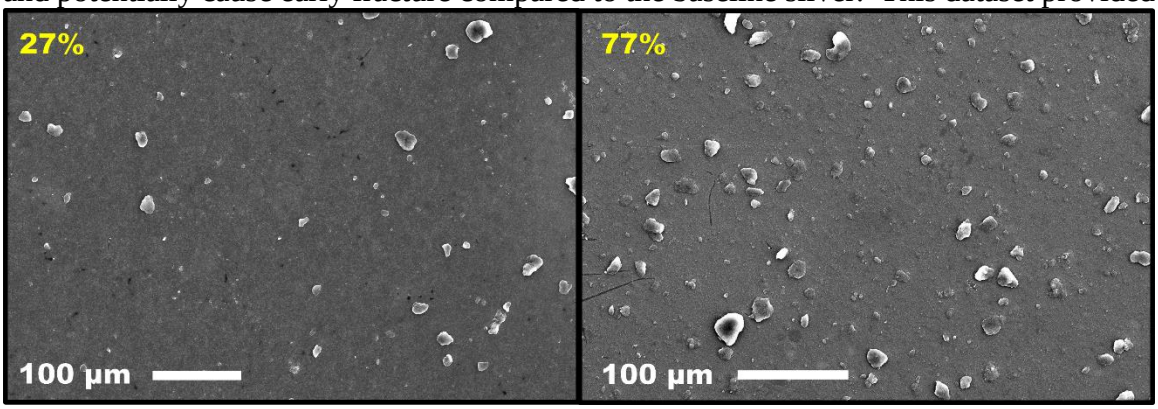

Figure 4.10 *Dataset 1: Agglomerations in 27% and 77% CNT surface coverage samples. Agglomerations have an average diameter of 11 µm.*

some promising initial indication that there may be an ideal CNT surface coverage for optimizing the MMC mechanical properties.

Analysis of Dataset 2

For *Dataset 2*, CNTs were coated using an ultrasonic atomizer nozzle. The CNTs were short (0.9 um) and multiwalled. Polymer wrapping (polyvinyl butyrate) was used for enhanced CNT dispersion in DI water for spray coating. Figure 4.11 shows a collection of one representative stress-strain curve from each CNT surface coverage sample set. All MMC stress-strain curves show higher ductility compared to the baseline curve. Figure 4.12 shows the average and standard deviation of each of the four extracted mechanical properties as a function of CNT loading. The elastic modulus, or stiffness, does not show a definite trend as a function of CNT loading. However, all MMCs have a lower elastic modulus compared to the baseline silver. This is likely due to the non-ideal adhesion between CNT and silver, or agglomeration sites within the CNT layer causing nanotube

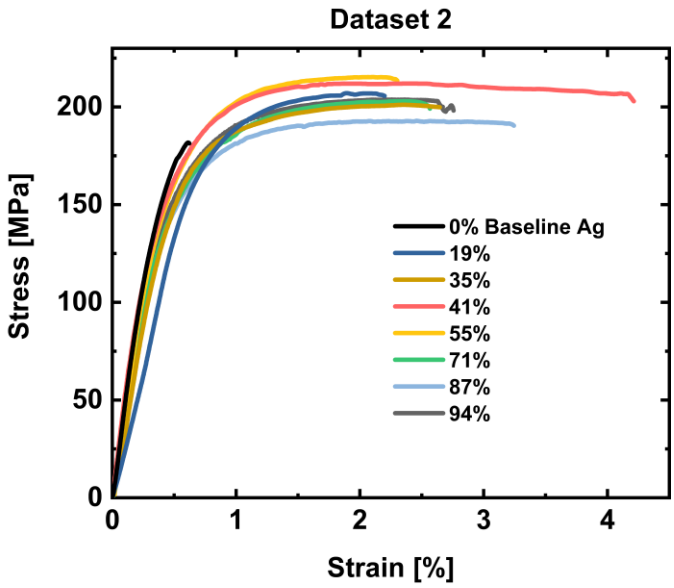

Figure 4.11 *Dataset 2: Representative stress-strain curve from each CNT surface coverage sample set*

slip and reducing stiffness. Figure 4.14 shows SEM images at low magnification for two samples within this dataset. Some agglomerations exist with average diameter of 1 µm. This is greatly reduced from *Dataset 1* agglomeration size of ~11 µm. The density of agglomerations in this set are also reduced. The reduction in agglomerations is like due to the reduced CNT concentration and lower, controlled flow rate of the ultrasonic nozzle setup. This setup also used a heated stage for rapid evaporation of the solvent.

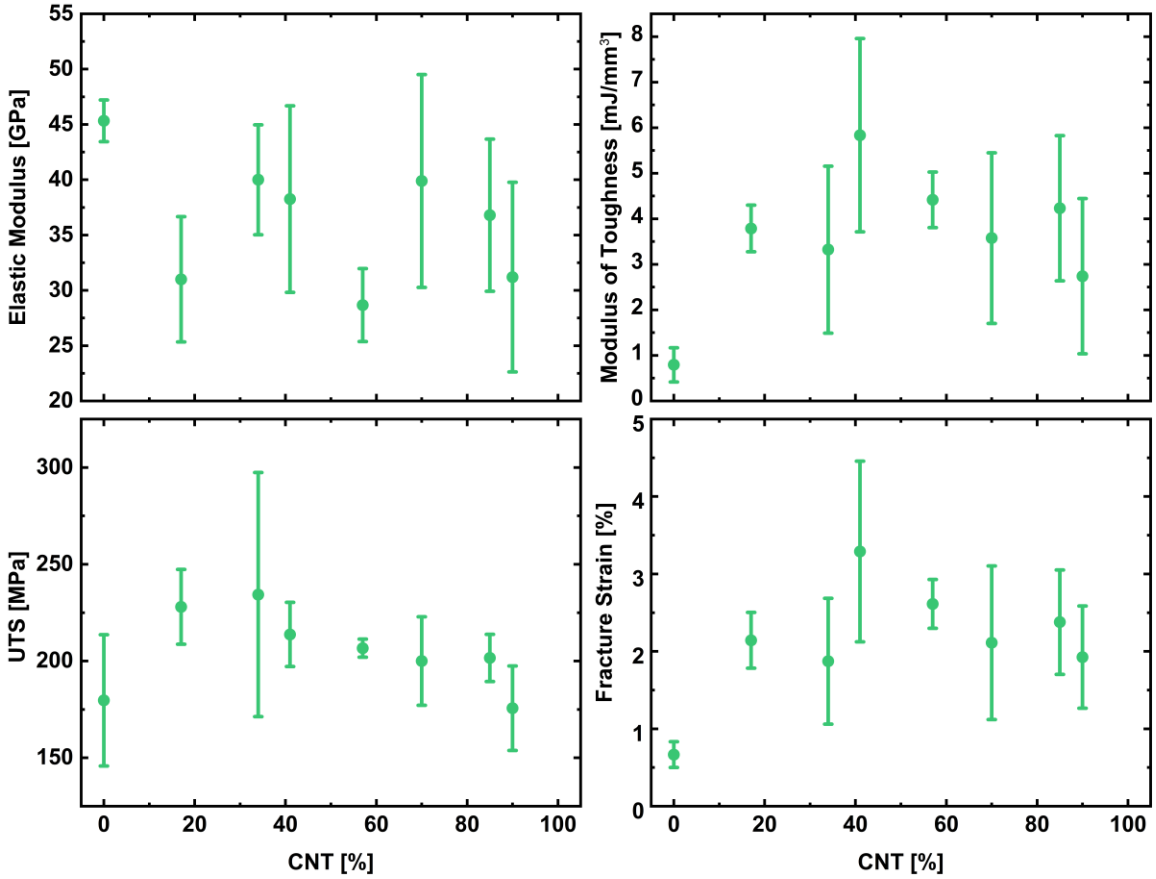

Figure 4.12 *Dataset 2: Mechanical properties as a function of CNT loading*

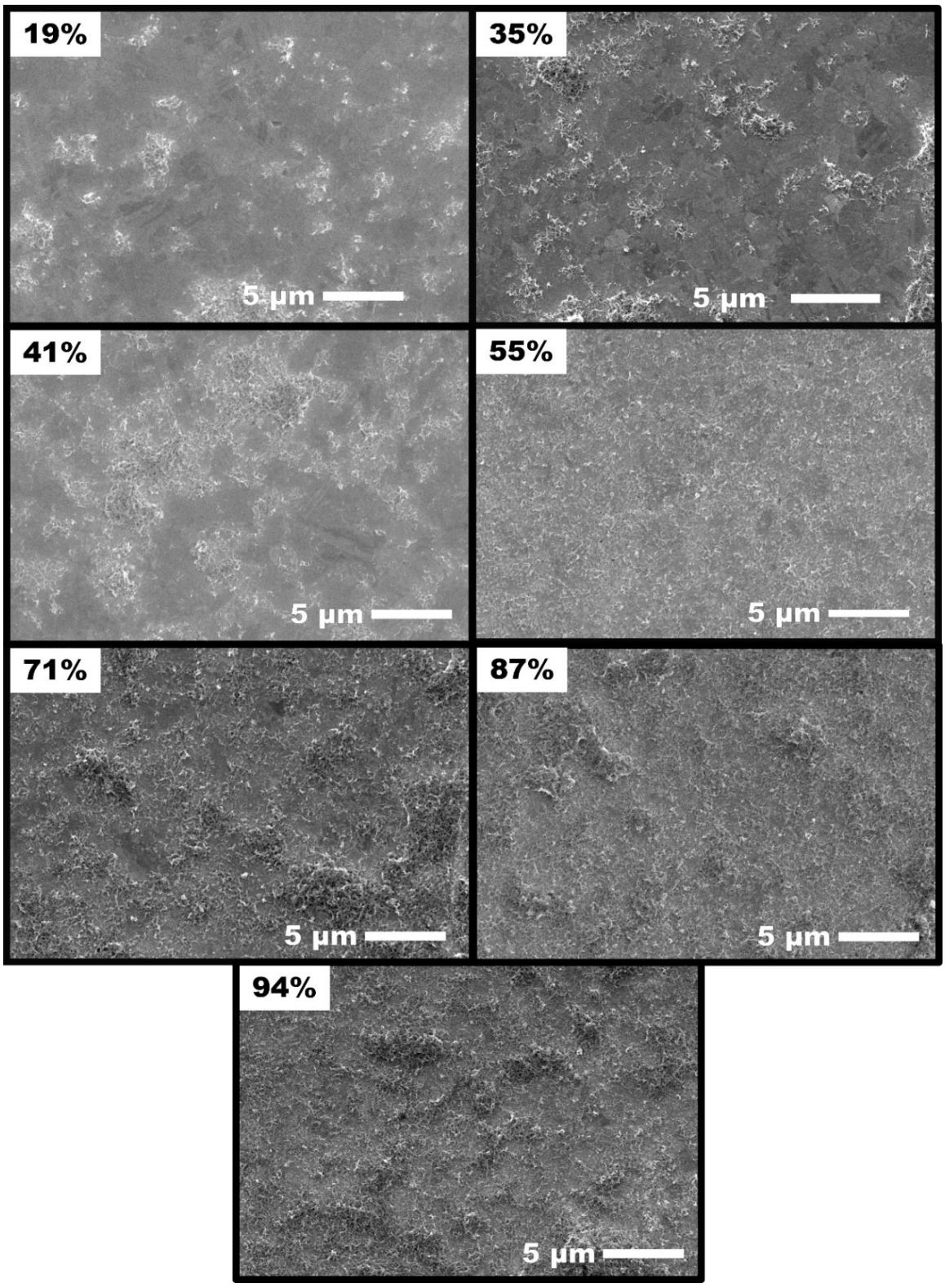

Figure 4.13 *Dataset 2: Top view SEM images of CNT layer for varying surface coverage*

The MMC values for toughness, UTS, and fracture strain are all greater than baseline silver. Toughness increases over 6-fold, UTS increases by a factor of 0.3, and fracture strain increases nearly 4-fold from baseline to their respective peak values. These three properties also show a subtle rise-and-fall trend with the peak being between 35% and 41% CNT surface coverage. The increased fracture strain and toughness of the composites suggest a more ductile material with an increased strain energy density with the inclusion of CNTs. The larger ultimate tensile strength (UTS) from baseline to composite, suggests there is load transfer from the silver to the CNTs leading to a MMC that can tolerate a larger tensile force than pure silver.

For toughness, UTS, and fracture strain the experimental values rise from baseline to 35-41% CNT surface coverage, then drop off. It is possible that the top layer of silver intercalating the CNT layer and meeting with the bottom silver layer has an impact on the composite's mechanical properties. As the CNT surface coverage increases and the silver intercalation (opening) decreases, the CNT network begins to weaken due to the CNT-CNT van der Waals bonding being the dominant adhesion force. As the CNT surface

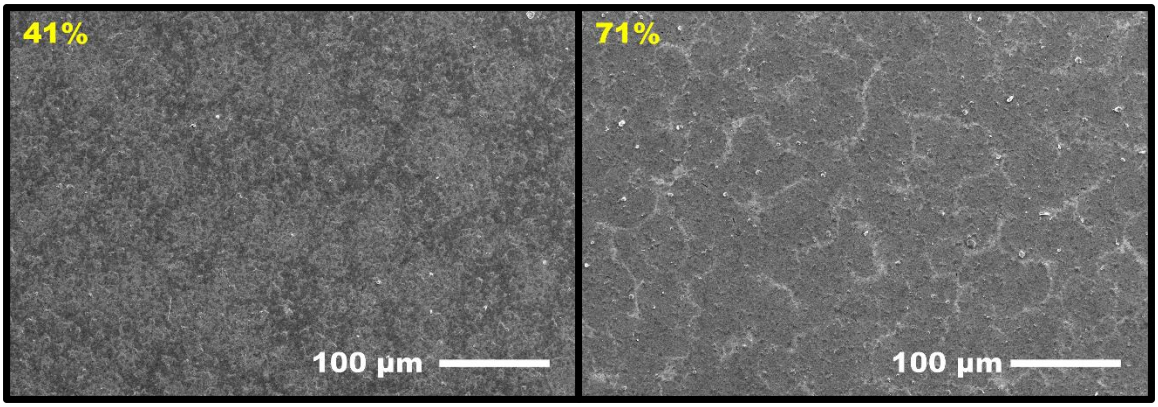

Figure 4.14 *Dataset 2: Agglomerations in 41% and 71% CNT surface coverage samples. Agglomerations have an average diameter of 1 µm.*

coverage increases, so does the number of inevitable CNT agglomerations sites that also lead to weak spots within the CNT network. Figure 4.13 provides a visualization of how the silver openings gradually reduce with CNT coverage as a dense carbon nanotube layer forms. It is also worth noting the formation of CNT mounds for coverages above 55%. These mounds likely contribute to the decrease of values seen in the UTS, toughness and fracture strain for coverages 71% - 94%.

Analysis of Dataset 3

The carbon nanotubes in *Dataset 3* are long, single walled nanotubes deposited via ultrasonic atomization. The stress-strain curves are shown in Figure 4.15 and average mechanical properties in Figure 4.16. For composite samples, each CNT loading had at least three samples tested and two for silver. For this set, the composites show larger stiffness, but decreased strength, toughness, and fracture strain compared to the baseline silver. This is a similar trend to *Dataset 1*. The composites with 16%, 42%, and 71% have

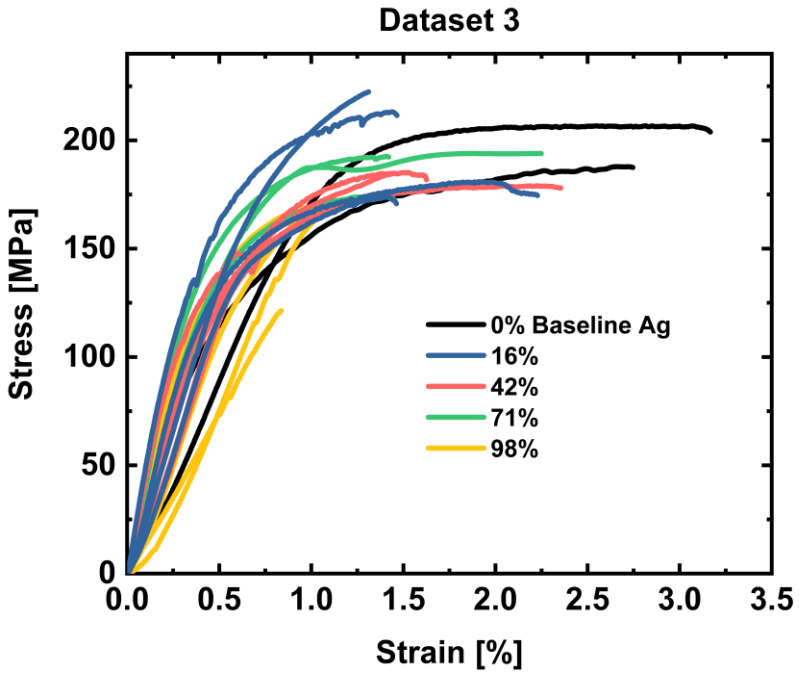

Figure 4.15 *Dataset 3: Stress-strain curves from tension testing*

similar mechanical responses. The 16% surface coverage composite shows a higher UTS compared to other composites. The composite with nearly full coverage in the CNT layer (98%) shows the largest reduction in mechanical properties. Again, this can be contributed to the increased CNT-CNT interactions at higher coverages with little silver intercalation.

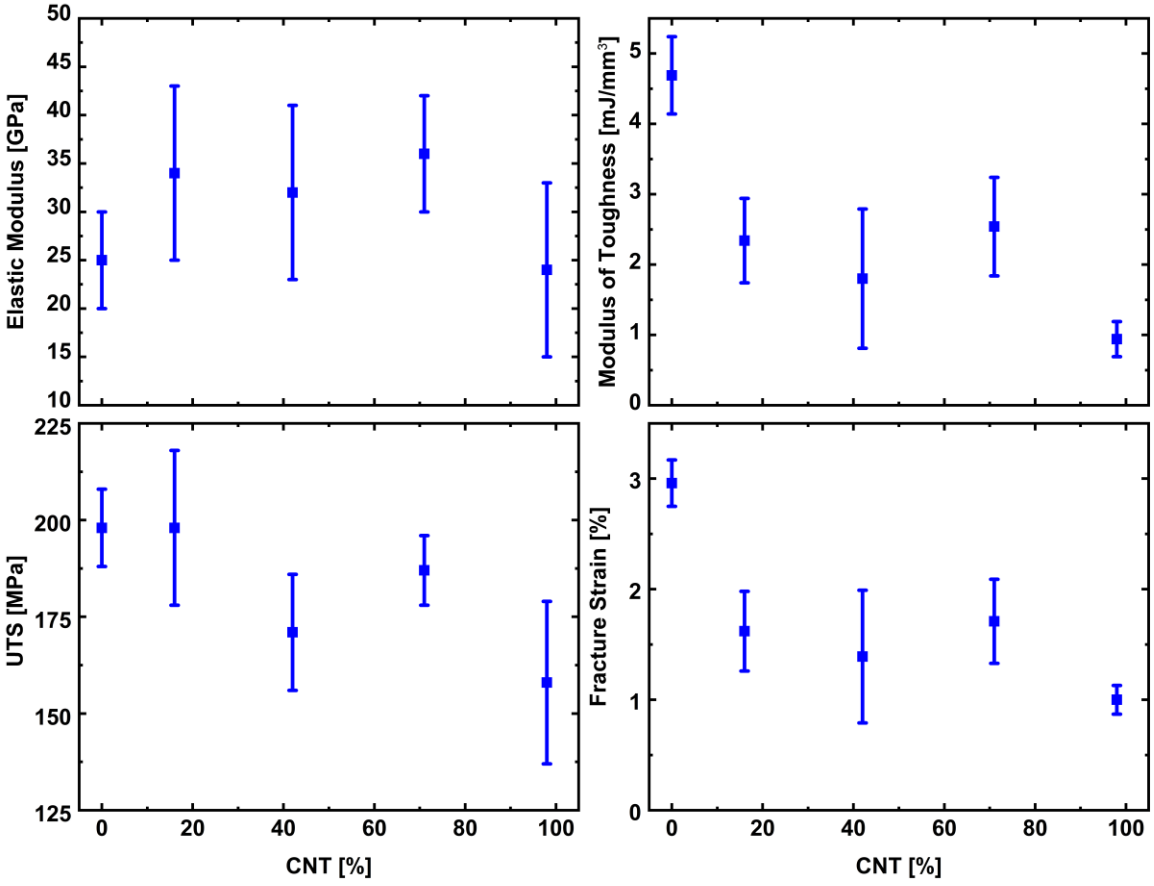

Figure 4.16 *Dataset 3: Mechanical parameters as a function of CNT surface coverage*

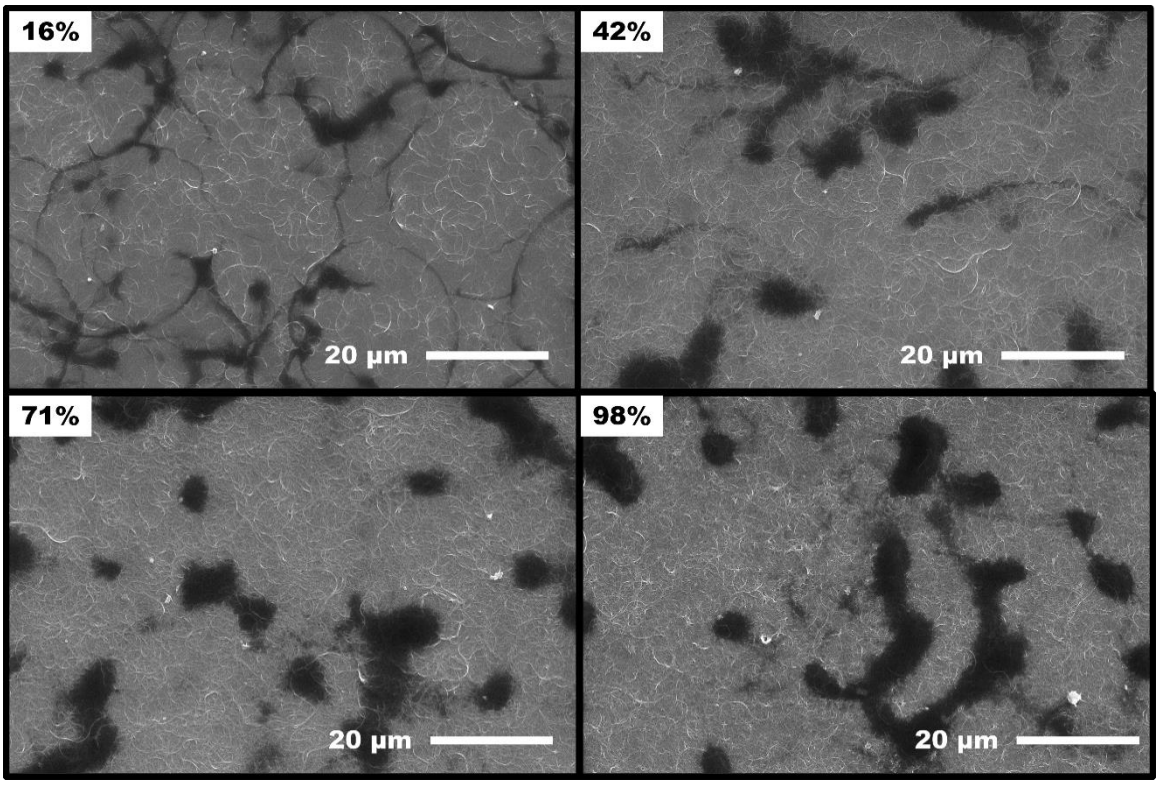

Figure 4.17 *Dataset 3: Topvew of CNT layer for varying surface coverages*

The CNTs used for this dataset are much longer than the other sets with an average length of 6 µm compared to 2.5 µm and 0.9 µm for the other sets. They are also single walled compared to the multiwalled CNTs used in *Datasets 1* and *2*. Figure 4.17 shows the general microstructure and CNT coverages of this dataset. The CNTs are well dispersed with very few agglomerations. Typically, short CNTs disperse better than long, here the dispersion is attributed to the EGBEA solvent. There are coffee rings that remain after spray coating from residual ethanol/EGBEA solvent. The width of the coffee ring appears to grow from 16% to 42% coverage then stabilizes for the remaining coverages.

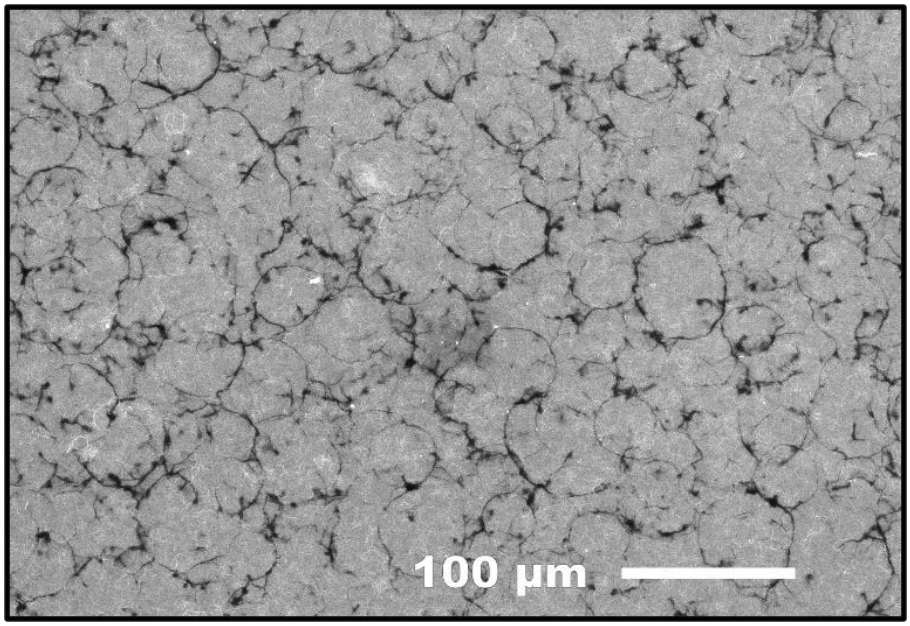

Figure 4.18 *Dataset 3: Few agglomerations are present, but coffee rings remain from ethanol/EGBEA solvent*

Comparison of All Sets

Figure 4.19 shows the four extracted material properties for each set in the same plots. To maintain an equivalent silver microstructure comparison of MMCs to Ag baseline samples, a set of baseline samples were metal evaporated alongside the MMCs for each dataset using the same evaporation rate. As seen from the comparison of the three datasets in Figure 4.19, there is variation in silver properties from set to set. This may be explained by instrumental variations in the metal evaporation processes from set to set. Due to the variations in chamber conditions, the relative comparison within each dataset is appropriate, but process dependencies should be considered for absolute comparison between sets. The elastic modulus shows similar values across all datasets. *Dataset 2* shows the largest toughness, fracture strain, and UTS for most CNT loading values. It appears that the short MWCNTs with smaller, fewer agglomeration perform the best mechanically. The reduced fracture strains of *Datasets 1* and *3* lead to reduced modulus

of toughness. The agglomerations of *Dataset 1* likely create regions of high localized stress that are susceptible to fracture at lower strains. For *Dataset 3* it's possible that the long SWCNTs do not actually provide significant reinforcement due to the slip at the CNT-CNT and CNT-Ag interfaces, leading to a weaker composite.

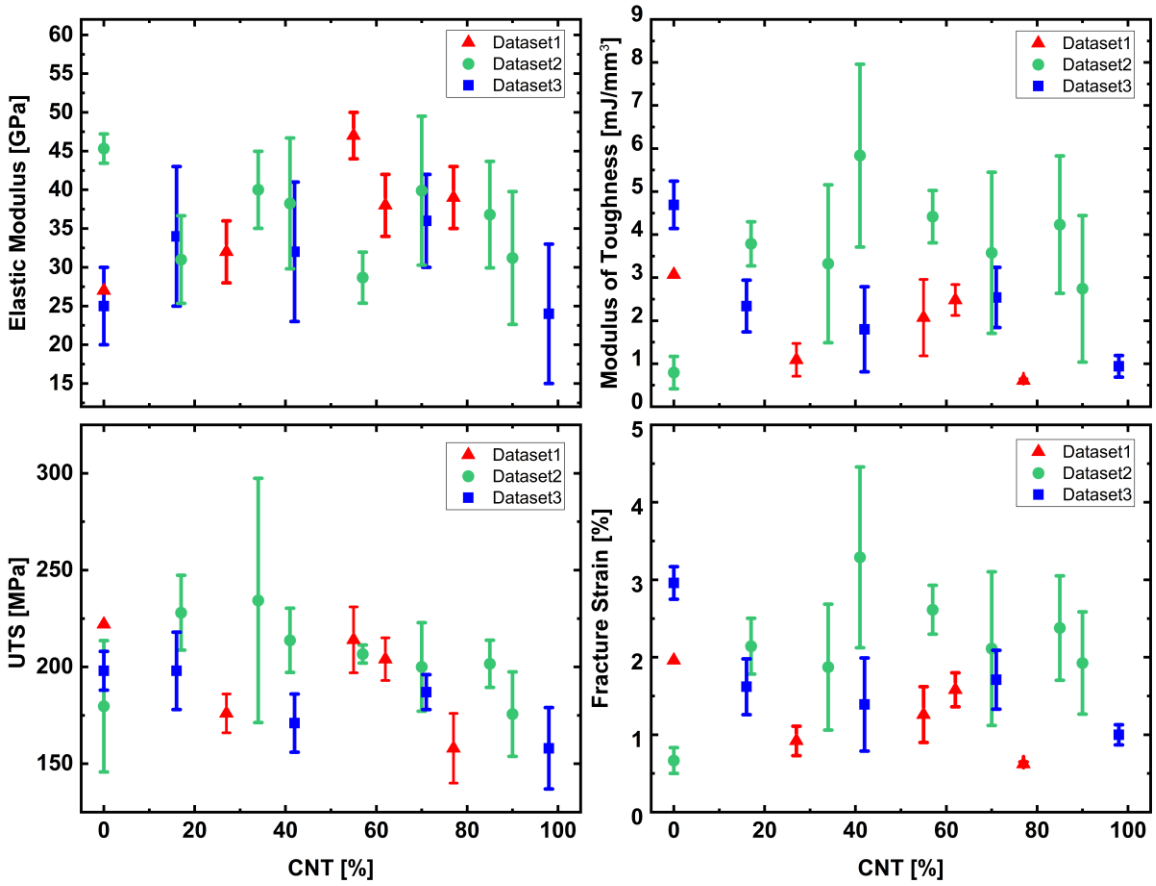

Figure 4.19 *Comparison of all dataset's mechanical properties*

The combination of these datasets show that agglomerations within the composite most strongly impact fracture strain, which propagates into the modulus of toughness calculations. This can be visualized in Figure 4.20, which shows the averaged composite mechanical properties of each dataset, where *Dataset 1* with large agglomerations has the lowest values. The long CNTs *(Dataset 3)* also have reduced facture strain compared to the short CNTs. *Dataset 2* shows the largest UTS. It's possible this enhancement could

be due grain refinement of the top silver layer due to CNT grain pinning of the short nanotubes. The elastic modulus is the parameter that has the most uncertainty based on the acquisition method. It is calculated as the slope of the stress-strain curve up to the yielding point. However, it is not always clear where the yield point is. Therefore, the values acquired could vary based on what portion of the slope is used for calculation. For this reason it's difficult to make any assumptions about the impact of CNT microstructure and content on the elastic modulus. Overall, it seems short carbon nanotubes with a center layer surface coverage around 35 – 41% provide the best mechanical response for this layer-by-layer composite structure.

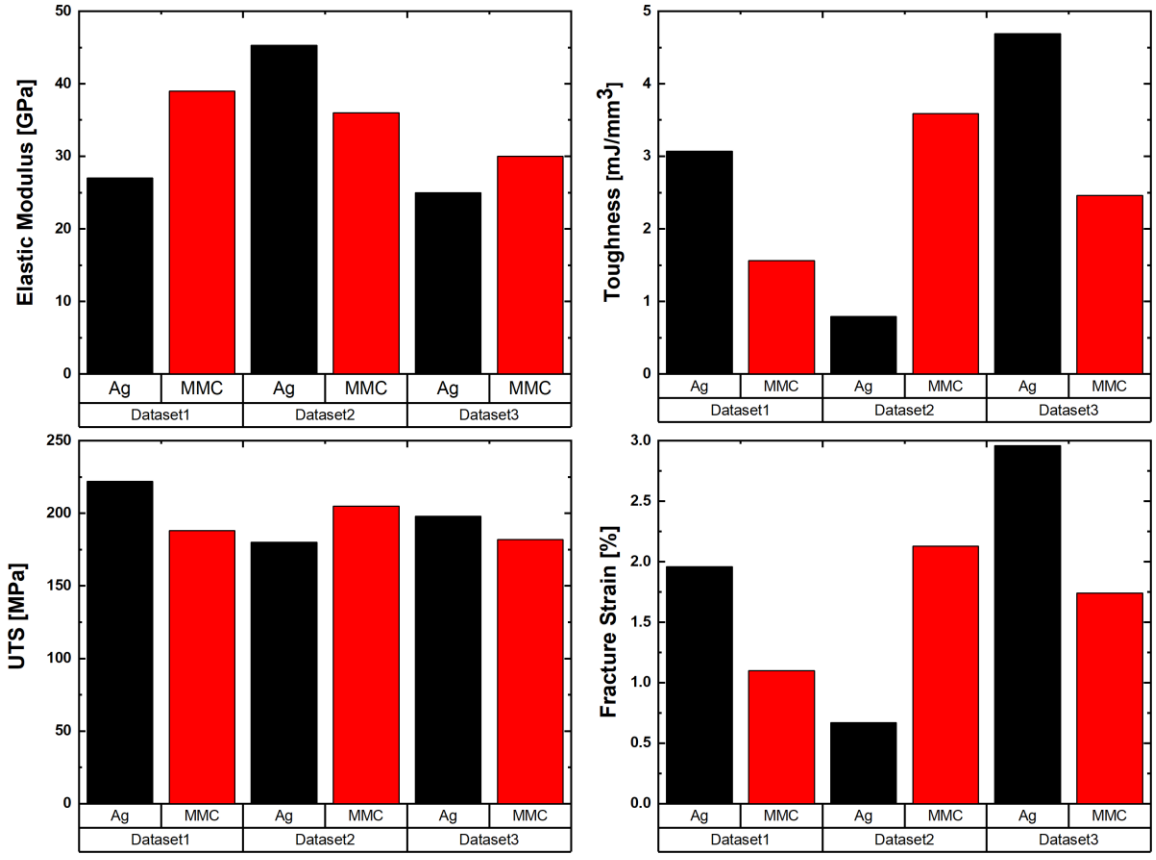

Figure 4.20 *MMC mechanical properties averaged for each dataset and compared to respective baseline. Dataset 2 with the short CNTs and 1 µm agglomerations perform best with respect to Ag baseline.*

4.5 Conclusions

This chapter has been focused on the fabrication and mechanical characterization of silver-carbon nanotube composites to determine if there is an optimal CNT loading or microstructure to yield the most advantageous composite mechanical response. Initially nanoindentation was explored using electroplated silver and dropcast/nanospread carbon nanotubes. Testing of silver grown at different electrodeposited cathode current densities showed current densities of 4 -5 mA/cm^2 to provide increased hardness and reduced elastic modulus compared to the lower current densities. The values of reduced elastic modulus of silver measured by nanoindentation were less than the silver elastic modulus measured by tension testing. This is likely due to differences is silver microstructure from differing growth methods. Electrochemical deposition tends to make more porous films compared to electron beam evaporation. Nanoindentation showed initial promise of mechanical enhancement using CNTs. Hardness and reduced modulus showed improvements compared to baseline silver for the more evenly distributed CNTs deposited by nanospreading. However, the technique provided localized results at shallow depths. This proved to not be the ideal mechanical testing method for the layer-by-layer structure. Therefore, a method of producing free-standing MMC films was utilized to test the composite in tension with no substrate effects.

The free-standing composites were fabricated with electron beam metal evaporated silver. Carbon nanotubes were deposited using spray coating methods for a more uniform distribution. Three composite datasets were fabricated and tested using DMA tension clamps. *Dataset 1* had large agglomerations but overall good dispersion. *Dataset 2* used short CNTs with smaller and fewer agglomerations than *Dataset 1*. *Dataset 3* used long

CNTs with good dispersion and very few agglomerations. *Dataset 2* proved to show the best mechanical response and improvement compared to baseline silver, indicating short CNTs even with some degree of agglomeration can slightly outperform composites with larger agglomerations or longer CNTs when compared to the respective baseline. This could be due to grain refinement of the top silver layer due to the short CNTs, decreased load transfer of the long CNTs due to van der Waals interaction, or initiation of crack sites due to the large agglomerations. The composites with short CNTs also showed the best performance at 35 – 41% surface coverage. These results show the potential of carbon nanotube incorporation to mechanically enhance silver and improve photovoltaic metallization longevity.

Further processing improvements and testing could be done to the composite to further enhance the mechanical properties and our understanding of the impact of CNT content and microstructure. The fabrication of the layer-by-layer structure is a straightforward process that could easily be incorporated into PV metallization manufacturing processes. However, having such a negligibly thin layer of CNTs between much thicker silver has shown to provide minimal reinforcement. The more ideal composite metallization would have CNTs uniformly dispersed throughout the entire structure. This can be done by incorporating CNTs into a silver paste and screen printing the composite as gridlines, something that this research group is continuing to investigate. Increasing the sample size of these tension tests would also be valuable for having a more statistically relevant dataset.

CHAPTER 5: COMPUTATIONAL MODELING OF METAL MATRIX COMPOSITE

5.1 Purpose of Finite Element Analysis

After mechanical characterization of the composites, finite element (FE) analysis was used to qualitatively explore how the carbon nanotubes (CNTs) behave as a bulk layer and how the CNT mechanical properties and content can impact the composite. The finite element software ABAQUS (*Version 2017, Dassault Systems Simulia Corp., Johnston, RI, USA*) was used to extract the possible effective properties of the CNT layer. As opposed to using a complicated and computationally expensive mesh of individual CNTs, an effective CNT material was employed for this model. The extracted properties of the effective layer encapsulate microstructure phenomena such as CNT agglomerations and CNT/Ag adhesion. The mesh geometry was further simplified to a symmetric, periodic microstructure of CNTs with intercalated silver.

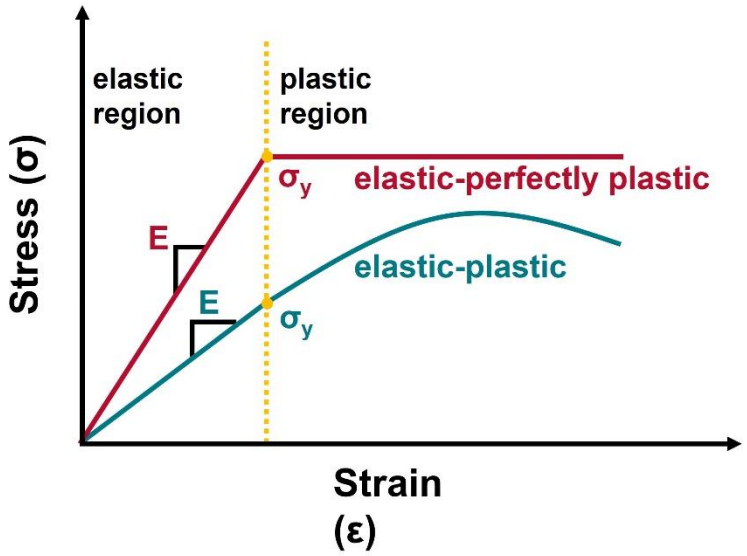

Figure 5.1 *Examples of stress-strain curves with elastic-perfectly plastic behavior vs. elastic-plastic behavior*

Both silver and the CNT layer were given elastic-plastic deformation properties. Materials with an elastic-plastic response initially behave elastically when a load is applied up to the yield stress. At the yield stress the material begins to deform plastically (permanently). The stress strain curve of the elastic region is linear, and the slope is the elastic modulus. After the yield point, plastic deformation begins, and the stress begins to level off. If the material is assumed to be perfectly plastic, the stress remains at the yield stress value, see Figure 5.1. In reality there is some degree of strain hardening causing a slight increase in stress, this is the elastic-plastic response.

The mechanical properties of interest for FE are the elastic modulus, yield stress, and points of strain hardening within the plastic response of the stress-strain curve. The silver material input properties were taken from experimental tensile test data (*Dataset 2)* of baseline silver samples. The CNT input properties were used as fitting parameters against composite stress-strain curves with equivalent CNT layer surface area coverage of experimental tensile tests. The fit values of the CNT effective layer were explored as a function of the CNT surface area coverage.

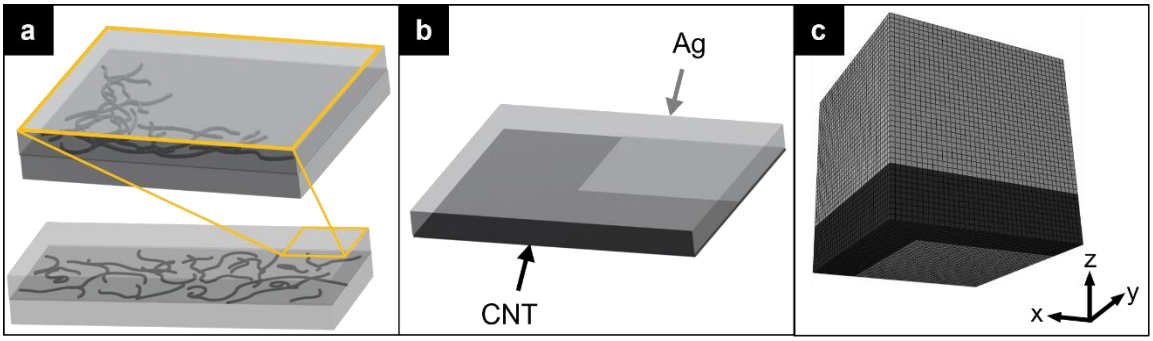

Figure 5.2 *a) Assumption of periodic silver openings within the CNT layer b) CNTs are assumed to function as an effective layer with layer properties encapsulating microstructure effects c) Model mesh, a representative volume element of the composite microstructure, simplified using symmetry assumptions*

5.2 Model Setup and Parameters

Model Geometry and Mesh

The metal matrix composite (MMC) microstructure is assumed to be a periodic distribution of CNTs with silver openings, illustrated in Figure 5.2. The layer-by-layer structure of CNTs sandwiched between two layers of silver provides a horizontal line of symmetry, allowing for only half the structure to be modeled in the z-direction. The assumption that the composite is a repeating unit cell of CNTs and silver openings can reduce the modeled MMC to a representative volume element (RVE). Again, due to symmetry, the final RVE is a quarter of the repeating unit cell. The individual CNTs all have a random orientation, but the overall distribution is relatively uniform. Since the CNT layer is thin and has less than 100% surface coverage for all MMC films, the silver does intercalate through the CNT layer openings during the final silver evaporation. The modeled geometry is a cube with a thick solid silver top layer and a thin CNT bottom layer with a square silver opening. A square-shaped silver opening was chosen as the most straightforward option within the CNT layer due to the global cubic geometry. The RVE uses general-purpose, 3D solid (continuum) linear hexahedral, stress/displacement elements each containing 8 nodes and 3 translational degrees of freedom. In the finite element analysis, the displacements are calculated at the nodes of the elements. In the hexahedral (brick) elements used in this work, the nodes are located at each corner and the displacements at other locations of the element are calculated using a linear interpolation between nodes [139]. The model mesh can be seen in Figure 5.2c. The actual composite films are 4 μm thick. With the horizontal symmetry, the modeling thickness is reduced to

2 µm. The RVE cube dimensions within ABAQUS were set to 2µm x 2µm x 2µm with a mesh (node spacing) size of 0.05.

Model Functionality and Parameters

Boundary conditions are used to constrict the symmetry planes that comprise the RVE. The bottom xy-plane, front xz-plane, and left yz-plane as shown in Figure 5.2c are all symmetry planes and have a boundary condition of zero displacement in their respective normal direction. All nodes along the right yz-plane are tied to a single node, forcing the entire plane to move at the same rate. A displacement is applied to this single node in the direction of the x-axis to mimic tensile loading. The resulting reaction force and displacement of this node provide the basis for the stress-strain curve of the modeled composite.

For modeling purposes, a representative stress-strain curve was selected from each set of CNT surface area tensile tests. The CNT surface coverage within the model was set to that of the experimental composite film. The applied displacement for the model was also set to the equivalent experimental fracture strain of the representative composite stress-strain curve. This displacement was applied at a uniform rate up to the experimental fracture point. The incremental displacement can be converted to strain values using the ratio of change in length to the initial length in the axial loading (x) direction. To calculate stress, the reaction force at the node where the displacement is applied is used. Stress is then the reaction force divide by the model cross sectional area.

5.3 Carbon Nanotube Parameter Extraction

For composite modeling and effective CNT property extraction, five CNT surface coverages are examined: 35%, 41%, 71%, 87%, and 94%. Of all the composite datasets discussed in Chapter 4.4, *Dataset 2* provided the best mechanical response, and was therefore chosen for finite element analysis. One representative stress-strain curve was fit from each set of CNT surface coverages. The elastic modulus, yield stress, and strain hardening points of the effective CNT layer are used as fitting parameters. The resulting stress-strain curve of the FE model is fit to the composite experimental stress-strain curve.

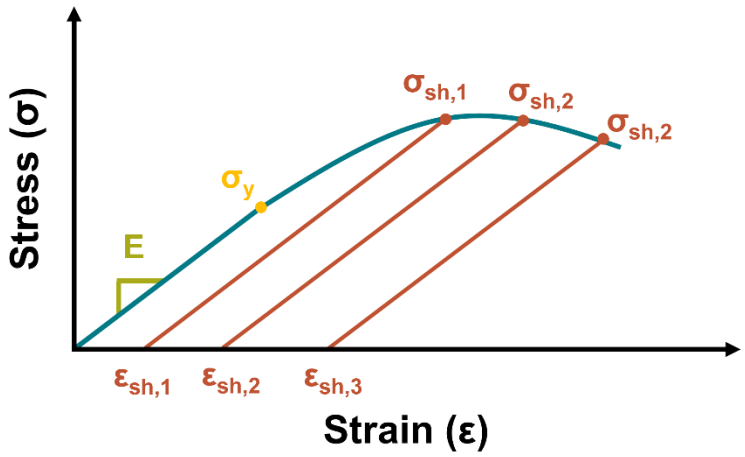

Figure 5.3 *Typical stress-strain response and material properties used for FE analysis. Elastic modulus (E) is slope of linear region, yield stress (σ_y) is the onset of plastic deformation, and (ε_{sh}, σ_{sh}) are the strain hardening coordinates*

The CNT layer of the composite is a layer of CNT regions with silver intercalation. The CNTs do not constitute a continuous film, therefore the thickness of the CNT layer is unknown and can be treated as another modeling parameter. When modeling the CNT regions as an effective layer, there are also microstructural effects that could expand beyond the CNT regions but contribute to the composite mechanics and increase the

thickness of the CNT effective layer. For example, the CNTs may cause pinning of the surrounding silver matrix therefore the CNT influence extends beyond the physical nanotube. With the assumption that there is a gradient opposed to a well-defined CNT-Ag interface, a CNT effective thickness can is also be employed in the FE model, giving some insight to potential reinforcement mechanisms of the carbon nanotubes. To explore these options, models of two carbon nanotube equivalent thicknesses were used to examine potential effective CNT properties. To examine possible CNT layer elastic modulus and yield stress values, a parametric analysis was done. First, a parametric study determined the value of elastic modulus that most closely fit the composite linear region. A second parametric study provided a yield stress value matching the experimental data. Lastly, strain hardening points were added to the plastic response of the model to correspond with the composite experimental data. Figure 5.3 illustrates these parameters in relation to a stress-strain curve.

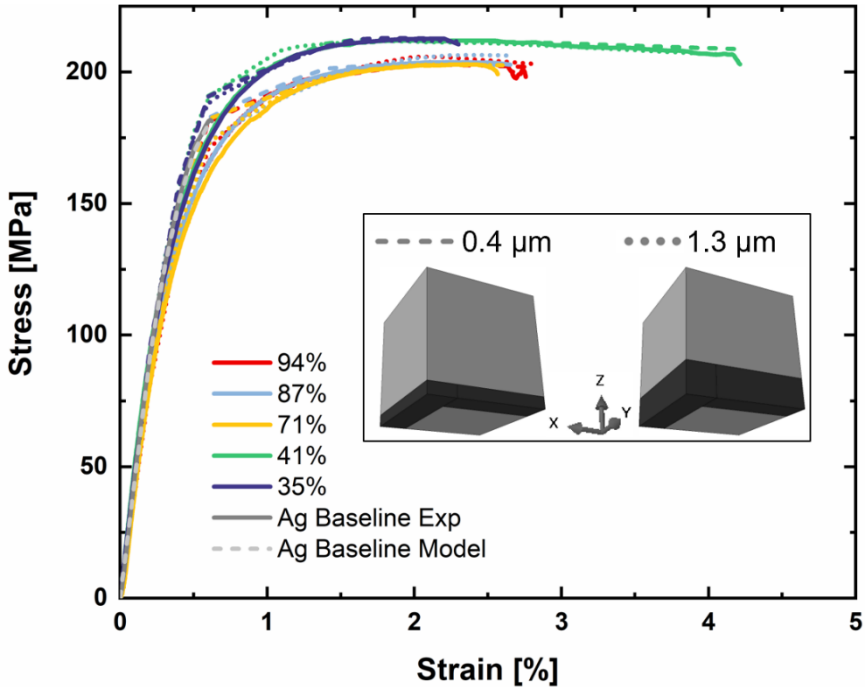

Figure 5.4 *Inset shows two effective CNT layer thicknesses used in the model. Experimental stress-strain curves along with resulting model curves from each thickness.*

An external code (written in Python) was used to automatically run multiple variants of the model only changing the value of CNT elastic modulus for a given range with a given increment. The array of resulting stress strain curves was then analyzed against the experimental curve. The elastic modulus value providing the best fit was kept as the effective CNT modulus for the next step of fitting. Next, the same parametric study was carried out for the yield stress. At this point in the modeling, the effective CNT layer is assumed to be elastic-perfectly plastic meaning there is no strain hardening. Once the best fit value of CNT yield stress was identified, a quadratic equation was used to include the trend of strain hardening effects in the post-yield region of the stress strain curve.

The input silver material properties were taken from experimental DMA tension tests of pure silver specimens. The silver was evaporated alongside all the composite samples and should have a representative microstructure (grain size and thickness) compared to the MMC samples. A total of three baseline silver samples were measured. The average elastic modulus was used as the material input, 45.5 GPa. The Poisson's ratio of silver was set to 0.37, a well agreed upon value [140]. A representative silver stress-

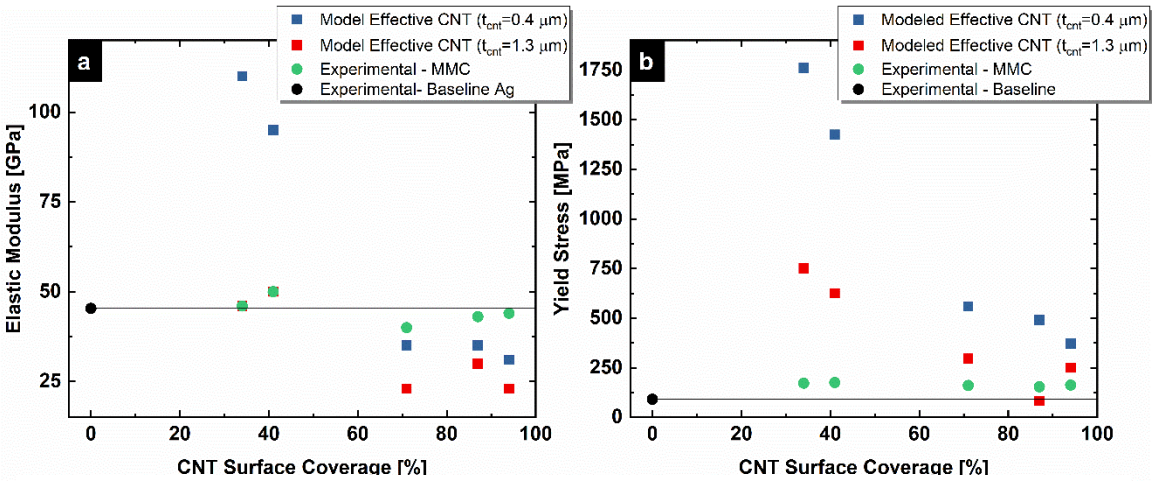

Figure 5.5 *Possible effective CNT elastic modulus and yield stress that provide a good fit to experimental data compared to experimental composite data*

strain curve was used for silver yield stress and plastic behavior, seen in Figure 5.4. The fit for the silver plastic behavior was done the same way described above using a pure silver RVE.

Finite element modeling was done for CNT layer equivalent thickness, 0.4 μm and 1.3 μm, see Figure 5.4 inset. These values are relative to the 4 μm composite, due to symmetry the modeled CNT thicknesses were halved. The carbon nanotube thickness of 0.4 μm was initially used and yielded surprisingly large mechanical values. The thickness was then increased to 1.3 μm under the assumption of CNT pinning increasing the effective thickness. The elastic and plastic properties of the effective CNT region can be systematically chosen for each thickness model, to generate the numerical stress-strain curves mimicking the experimental results. The extracted effective CNT elastic modulus and yield stress are shown in Figure 5.5. The experimental MMC and silver baseline data are also included for reference. There is a need to use very high elastic modulus (95 – 110 GPa) values for the model with a CNT effective thickness of 0.4 μm in the ideal loading range of 35-41%, to generate the desired stress-strain response. *Zhan, et. al* reported an elastic modulus between 55.2 – 58.9 GPa for highly aligned and densely packed CNT films [70]**.** The modulus required to match experimental results is almost twice that of the highly aligned and densely packed CNT films. Due to observed agglomerations and random CNT orientation seen in *Dataset 2*, it is anticipated that the large elastic modulus values are not representative of the CNT effective layer. More reasonable modulus values (23 – 50 GPa) are used to achieve a good fit for the 1.3 μm model.

5.4 Conclusion

The experimental data of *Dataset 2* indicate mechanical reinforcement of carbon nanotubes seen by the increase in yield stress in MMCs compared to baseline silver. The entirety of the mechanical response cannot be explained using the simplified, two-phase model presented here. The actual CNT structure has a more inhomogeneous distribution with more complex interfaces between CNT-Ag and CNT-CNT interaction.

The composite microstructure may be explained as a layer-by-layer structure with the center, carbon nanotube containing layer extending beyond the physical CNTs. The short CNTs may be responsible for pinning the silver matrix that directly surround the nanotubes, increasing the CNT effective thickness and strengthening the material. This is a phenomenon that has been reported in the literature for short CNTs [44, 48, 49]. These results suggest CNT pinning and silver grain refinement due to the CNTs may play a role as a reinforcement strengthening mechanism in this composite structure. As with the mechanical property analysis from DMA data, more measured samples with greater correlation to CNT loading would provide a higher quality fit for the FEA model layers.

CONCLUSIONS

In this work the impact of carbon nanotube (CNT) reinforcement in a silver matrix was explored as photovoltaic cell metallization and as a free-standing composite film for mechanical analysis. CNT metal matrix composites (MMC) were fabricated in a layer-by-layer structure with carbon nanotubes sandwiched between two layers of silver metal. The composite integration onto solar cell gridlines demonstrated the ability of carbon nanotubes to electrically bridge cracks within the device and maintain electrical conductivity compared to standard metal grid lines. PV cells with composite metallization had at most a loss in short circuit current of 1%, compared to the control cells that showed a maximum current loss of 55%. These results established the crack-bridging capabilities of carbon nanotubes in a layer-by-layer composite. To further understand the microstructure of the Ag/CNT composite and impact of the carbon nanotubes on the material properties of the bulk, composite films were fabricated and tested with nanoindentation and under tension as free-standing films. The stress-strain curves from one tension dataset were fit with a finite element numerical model using a representative volume element (RVE) of the composite microstructure. Potential carbon nanotube material properties were used as the fitting parameter to investigate how the CNT domain may behave as an effective layer.

Initial composite mechanical testing was done using nanoindentation. The results suggested that a more uniformly dispersed carbon nanotube layer can yield increased hardness and elastic modulus. To test the MMCs in tension with no substrate effects, free-standing composite films were fabricated. Within these films, each silver layer was 2 μm with a thin spray coated layer of CNTs in between. Standard silver solar cell gridlines are deposited with a thickness of 4 μm and this dimension was chosen for the free-standing

composite film thickness for comparison. The layer-by-layer structure was fabricated using simplified manufacturing techniques such as spray-coating that could be applied to preexisting PV fabrication processes.

The results of tension testing for three datasets having differing CNT geometries and degrees of agglomeration indicated an enhanced mechanical response for the composite with the shortest (0.9 μm) CNTs *(Dataset 2)* when compared to the baseline. This dataset also contained agglomerations visible under SEM with average diameters of 1 μm. *Dataset 1* contained large agglomerations (~11 μm) and had the lowest value of fracture strain and toughness. This set showed reduction in most mechanical properties compared to the baseline samples. Prior work indicates that the large agglomerates can create crack initiation sites that lead to fracture at lower strain than a uniform metal matrix with no reinforcement particle. Although *Dataset 3* had the greatest uniformity in the deposited carbon nanotubes and extremely low agglomeration density, DMA results exhibited a reduced mechanical response. A potential cause for this reduction is the longer (2 – 20 μm) carbon nanotubes compared to the 0.9 μm tubes in *Dataset 1*. The increased surface area increases the density of mechanically weaker van der Waals interactions between the individual carbon nanotube walls, allowing for pull out of the CNTs under tensile loading.

This objective for tension testing of this composite structure was to understand how carbon nanotube content impacted the MMC mechanical response. *Dataset 2* showed an ideal loading window of 35 – 41% CNT coverage which agrees with results from the literature [52]. For the other MMC sample sets, there is no strong trend in mechanical properties as a function of CNT loading. With a much larger data set, process and analysis

uncertainties can be reduced and effects of the CNT inclusions may be more observable. Another possibility for the lack of obvious correlation in CNT surface coverage is that the CNT volume fraction of the entire composite is very small relative to the silver matrix. The change in surface coverage of the CNT layer within this composite structure only slightly increases the volume fraction and the potential contributions of CNT reinforcement. Increasing the CNT content in a single layer within this structure decreases the mechanical response by increasing slip at CNT-CNT interfaces. If a layer-by-layer thin film is to be used as PV metallization it is best for the CNT layer to not be continuous. This allows for a reinforcement effect of the nanotube by providing more regions of Ag/CNT contact and limiting CNT-CNT interactions which are weaker than the individual nanotubes. The dispersed CNTs can also lead to grain refinement of the silver matrix, or act as barriers to dislocation motion increasing yield stress of the composite.

To investigate a more uniformly dispersed MMC, ongoing work by this research group is being done to explore another CNT/Ag composite microstructure fabricated by an alternative method. To maintain applicability to PV manufacturing techniques, a common form of PV metallization deposition is utilized whereby silver paste is screen printed onto the semiconductor substrate and then fired to form a crystalline metal grid line. Carbon nanotubes can be homogeneously dispersed within the silver paste which can then be printed and fired with no modification to the traditional process. This allows for a MMC microstructure with a volumetrically uniform carbon nanotube distribution as opposed to a localized layer in the sandwich structure used in this work. Initial comparisons of DMA results for a fired Ag/CNT paste show stronger correlation with CNT inclusion as compared to the film coverage explored in this work [141].

REFERENCES

1. Park N, Jeong J, Han C (2014) Estimation of the degradation rate of multi-crystalline silicon photovoltaic module under thermal cycling stress. Microelectronics Reliability 54:1562–1566. https://doi.org/10.1016/j.microrel.2014.03.021

2. Roy S, Kumar S, Gupta R (2019) Investigation and analysis of finger breakages in commercial crystalline silicon photovoltaic modules under standard thermal cycling test. Engineering Failure Analysis 101:309–319. https://doi.org/10.1016/j.engfailanal.2019.03.031

3. Köntges M, Kunze I, Kajari-Schröder S, et al (2011) The risk of power loss in crystalline silicon based photovoltaic modules due to micro-cracks. Solar Energy Materials and Solar Cells 95:1131–1137. https://doi.org/10.1016/j.solmat.2010.10.034

4. Shen Y-L (2016) Numerical Study of Solder Bond Failure in Photovoltaic Modules. Procedia Eng 139:93–100. https://doi.org/10.1016/j.proeng.2015.08.1113

5. Köntges M, Siebert M, Morlier A, et al (2016) Impact of transportation on silicon wafer-based photovoltaic modules: Impact of transportation on photovoltaic modules. Prog Photovolt: Res Appl 24:1085–1095. https://doi.org/10.1002/pip.2768

6. Morlier A, Haase F, Kontges M (2015) Impact of Cracks in Multicrystalline Silicon Solar Cells on PV Module Power—A Simulation Study Based on Field Data. IEEE J Photovolt 5:1735–1741. https://doi.org/10.1109/JPHOTOV.2015.2471076

7. Corrado M, Infuso A, Paggi M (2017) Simulated hail impacts on flexible photovoltaic laminates: testing and modelling. Meccanica 52:1425–1439. https://doi.org/10.1007/s11012-016-0483-2

8. Gou X, Li X, Wang S, et al (2018) The Effect of Microcrack Length in Silicon Cells on the Potential Induced Degradation Behavior. International Journal of Photoenergy 2018:1–6. https://doi.org/10.1155/2018/4381579

9. Lee Y, Tay AAO (2013) Stress Analysis of Silicon Wafer-Based Photovoltaic Modules Under IEC 61215 Mechanical Load Test. Energy Procedia 33:265–271. https://doi.org/10.1016/j.egypro.2013.05.067

10. Käsewieter J, Haase F, Larrodé MH, Köntges M (2014) Cracks in Solar Cell Metallization Leading to Module Power Loss under Mechanical Loads. Energy Procedia 55:469–477. https://doi.org/10.1016/j.egypro.2014.08.011

11. Del Prado Santamaria R, Dos Reis Benatto GA, Lancia AAS, et al (2021) Characterization of Electrical Parameters of Cracked Crystalline Silicon Solar Cells

in Photovoltaic Modules. In: 2021 IEEE 48th Photovoltaic Specialists Conference (PVSC). IEEE, Fort Lauderdale, FL, USA, pp 0846–0853

12. Dolara A, Leva S, Manzolini G, Ogliari E (2014) Investigation on Performance Decay on Photovoltaic Modules: Snail Trails and Cell Microcracks. IEEE J Photovoltaics 4:1204–1211. https://doi.org/10.1109/JPHOTOV.2014.2330495

13. Varma Siruvuri SDVSS, Budarapu PR, Paggi M (2022) Current–voltage characteristics of silicon based solar cells in the presence of cracks: MD simulations. Semicond Sci Technol 37:025011. https://doi.org/10.1088/1361-6641/ac3374

14. Köntges M, Oreski G, Jahn U, et al (2017) Assessment of photovoltaic module failures in the field: International Energy Agency Photovoltaic Power Systems Programme: IEA PVPS Task 13, Subtask 3: report IEA-PVPS T13-09:2017. International Energy Agency, Paris

15. Chaturvedi P, Hoex B, Walsh TM (2013) Broken metal fingers in silicon wafer solar cells and PV modules. Solar Energy Materials and Solar Cells 108:78–81. https://doi.org/10.1016/j.solmat.2012.09.013

16. Electrical Conductivity - Elements and other Metals. https://www.engineeringtoolbox.com/conductors-d_1381.html

17. Ebong A, Chen N (2012) Metallization of crystalline silicon solar cells: A review. In: High Capacity Optical Networks and Emerging/Enabling Technologies. IEEE, Istanbul, Turkey, pp 102–109

18. Wang Y, Weng GJ (2018) Electrical Conductivity of Carbon Nanotube- and Graphene-Based Nanocomposites. In: Meguid SA, Weng GJ (eds) Micromechanics and Nanomechanics of Composite Solids. Springer International Publishing, Cham, pp 123–156

19. Choudhary V, Gupt A (2011) Polymer/Carbon Nanotube Nanocomposites. In: Yellampalli S (ed) Carbon Nanotubes - Polymer Nanocomposites. InTech

20. Popov V (2004) Carbon nanotubes: properties and application. Materials Science and Engineering: R: Reports 43:61–102. https://doi.org/10.1016/j.mser.2003.10.001

21. Wong H-SP, Akinwande D (2011) Carbon nanotube and graphene device physics. Cambridge University Press, Cambridge; New York

22. Hayashi T, Kim YA, Natsuki T, Endo M (2007) Mechanical Properties of Carbon Nanomaterials. ChemPhysChem 8:999–1004. https://doi.org/10.1002/cphc.200700077

23. Iijima S (1991) Helical microtubules of graphitic carbon. Nature 354:56–58. https://doi.org/10.1038/354056a0

24. Treacy MMJ, Ebbesen TW, Gibson JM (1996) Exceptionally high Young's modulus observed for individual carbon nanotubes. Nature 381:678–680. https://doi.org/10.1038/381678a0

25. Yu M-F, Lourie O, Dyer MJ, et al (2000) Strength and Breaking Mechanism of Multiwalled Carbon Nanotubes Under Tensile Load. Science 287:637–640. https://doi.org/10.1126/science.287.5453.637

26. Peng B, Locascio M, Zapol P, et al (2008) Measurements of near-ultimate strength for multiwalled carbon nanotubes and irradiation-induced crosslinking improvements. Nature Nanotech 3:626–631. https://doi.org/10.1038/nnano.2008.211

27. Ibrahim KS (2013) Carbon nanotubes-properties and applications: a review. Carbon letters 14:131–144. https://doi.org/10.5714/CL.2013.14.3.131

28. Bakshi SR, Lahiri D, Agarwal A (2010) Carbon nanotube reinforced metal matrix composites - a review. International Materials Reviews 55:41–64. https://doi.org/10.1179/095066009X12572530170543

29. Chen B, Li S, Imai H, et al (2015) Load transfer strengthening in carbon nanotubes reinforced metal matrix composites via in-situ tensile tests. Composites Science and Technology 113:1–8. https://doi.org/10.1016/j.compscitech.2015.03.009

30. Cox HL (1952) The elasticity and strength of paper and other fibrous materials. Br J Appl Phys 3:72–79. https://doi.org/10.1088/0508-3443/3/3/302

31. Fan J-P, Zhuang D-M, Zhao D-Q, et al (2006) Toughening and reinforcing alumina matrix composite with single-wall carbon nanotubes. Appl Phys Lett 89:121910. https://doi.org/10.1063/1.2336623

32. Esawi AMK, Morsi K, Sayed A, et al (2009) Fabrication and properties of dispersed carbon nanotube–aluminum composites. Materials Science and Engineering: A 508:167–173. https://doi.org/10.1016/j.msea.2009.01.002

33. Li L, Xia ZH, Curtin WA, Yang YQ (2009) Molecular Dynamics Simulations of Interfacial Sliding in Carbon-Nanotube/Diamond Nanocomposites. Journal of the American Ceramic Society 92:2331–2336. https://doi.org/10.1111/j.1551-2916.2009.03214.x

34. Cox ND, Rape A, Pham M, et al (2016) Free-standing silver/carbon nanotube metal matrix composite thin films. J Mater Sci 51:10935–10942. https://doi.org/10.1007/s10853-016-0305-x

35. Suárez S, Ramos-Moore E, Lechthaler B, Mücklich F (2014) Grain growth analysis of multiwalled carbon nanotube-reinforced bulk Ni composites. Carbon 70:173–178. https://doi.org/10.1016/j.carbon.2013.12.089

36. Bai JB, Allaoui A (2003) Effect of the length and the aggregate size of MWNTs on the improvement efficiency of the mechanical and electrical properties of nanocomposites—experimental investigation. Composites Part A: Applied Science and Manufacturing 34:689–694. https://doi.org/10.1016/S1359-835X(03)00140-4

37. Wilson K, Barrera EV, Bayazitoglu Y (2010) Processing of Titanium Single-Walled Carbon Nanotube Metal-Matrix Composites by the Induction Melting Method. Journal of Composite Materials 44:1037–1048. https://doi.org/10.1177/0021998310367263

38. Nam DH, Cha SI, Lim BK, et al (2012) Synergistic strengthening by load transfer mechanism and grain refinement of CNT/Al–Cu composites. Carbon 50:2417–2423. https://doi.org/10.1016/j.carbon.2012.01.058

39. Hall EO (1951) The Deformation and Ageing of Mild Steel: III Discussion of Results. Proc Phys Soc B 64:747–753. https://doi.org/10.1088/0370-1301/64/9/303

40. Petch N (1953) The Cleavage Strength of Polycrystals. Journal of the Iron and Steel Institute 3:25–28

41. Hansen N (2004) Hall–Petch relation and boundary strengthening. Scripta Materialia 51:801–806. https://doi.org/10.1016/j.scriptamat.2004.06.002

42. Cordero ZC, Knight BE, Schuh CA (2016) Six decades of the Hall–Petch effect – a survey of grain-size strengthening studies on pure metals. International Materials Reviews 61:495–512. https://doi.org/10.1080/09506608.2016.1191808

43. Ashby MF (1970) The deformation of plastically non-homogeneous materials. The Philosophical Magazine: A Journal of Theoretical Experimental and Applied Physics 21:399–424. https://doi.org/10.1080/14786437008238426

44. Fitch C, Morsi K (2021) Effect of Shortening Carbon Nanotubes on Carbon Nanotube Dispersion, Damage and Mechanical Behavior of Carbon Nanotube-Metal Matrix Nanocomposites. Metallogr Microstruct Anal 10:167–173. https://doi.org/10.1007/s13632-021-00725-x

45. Manohar PA, Ferry M, Chandra T (1998) Five Decades of the Zener Equation. ISIJ International 38:913–924. https://doi.org/10.2355/isijinternational.38.913

46. Park JG, Keum DH, Lee YH (2015) Strengthening mechanisms in carbon nanotube-reinforced aluminum composites. Carbon 95:690–698. https://doi.org/10.1016/j.carbon.2015.08.112

47. Orowan E (1948) Symposium on internal stress in metals and alloys. Institute of Metals 451:

48. Chen B, Shen J, Ye X, et al (2017) Length effect of carbon nanotubes on the strengthening mechanisms in metal matrix composites. Acta Materialia 140:317–325. https://doi.org/10.1016/j.actamat.2017.08.048

49. Tan J, Yu T, Xu B, Yao Q (2006) Microstructure and wear resistance of nickel–carbon nanotube composite coating from brush plating technique. Tribol Lett 21:107–111. https://doi.org/10.1007/s11249-006-9025-8

50. Ruoff RS, Tersoff J, Lorents DC, et al (1993) Radial deformation of carbon nanotubes by van der Waals forces. Nature 364:514–516. https://doi.org/10.1038/364514a0

51. Bakshi SR, Agarwal A (2011) An analysis of the factors affecting strengthening in carbon nanotube reinforced aluminum composites. Carbon 49:533–544. https://doi.org/10.1016/j.carbon.2010.09.054

52. Feng Y, Yuan HL, Zhang M (2005) Fabrication and properties of silver-matrix composites reinforced by carbon nanotubes. Materials Characterization 55:211–218. https://doi.org/10.1016/j.matchar.2005.05.003

53. Li H, Fan J, Kang J, et al (2014) In-situ homogeneous synthesis of carbon nanotubes on aluminum matrix and properties of their composites. Transactions of Nonferrous Metals Society of China 24:2331–2336. https://doi.org/10.1016/S1003-6326(14)63353-7

54. Yang P, Wang N, Zhang J, et al (2022) Investigation of the microstructure and tribological properties of CNTs/Ni composites prepared by electrodeposition. Mater Res Express 9:036404. https://doi.org/10.1088/2053-1591/ac5c2b

55. Deng CF, Wang DZ, Zhang XX, Li AB (2007) Processing and properties of carbon nanotubes reinforced aluminum composites. Materials Science and Engineering: A 444:138–145. https://doi.org/10.1016/j.msea.2006.08.057

56. Tjong SC (2013) Recent progress in the development and properties of novel metal matrix nanocomposites reinforced with carbon nanotubes and graphene nanosheets. Materials Science and Engineering: R: Reports 74:281–350. https://doi.org/10.1016/j.mser.2013.08.001

57. Romanov VS, Lomov SV, Verpoest I, Gorbatikh L (2015) Stress magnification due to carbon nanotube agglomeration in composites. Composite Structures 133:246–256. https://doi.org/10.1016/j.compstruct.2015.07.069

58. Palaci I, Fedrigo S, Brune H, et al (2005) Radial Elasticity of Multiwalled Carbon Nanotubes. Phys Rev Lett 94:175502. https://doi.org/10.1103/PhysRevLett.94.175502

59. Anumandla V, Gibson RF (2006) A comprehensive closed form micromechanics model for estimating the elastic modulus of nanotube-reinforced composites.

Composites Part A: Applied Science and Manufacturing 37:2178–2185. https://doi.org/10.1016/j.compositesa.2005.09.016

60. Fisher F (2003) Fiber waviness in nanotube-reinforced polymer composites—I: Modulus predictions using effective nanotube properties. Composites Science and Technology 63:1689–1703. https://doi.org/10.1016/S0266-3538(03)00069-1

61. Alian AR, Meguid SA (2017) Molecular dynamics simulations of the effect of waviness and agglomeration of CNTs on interface strength of thermoset nanocomposites. Phys Chem Chem Phys 19:4426–4434. https://doi.org/10.1039/C6CP07464B

62. Banhart F (2009) Interactions between metals and carbon nanotubes: at the interface between old and new materials. Nanoscale 1:201. https://doi.org/10.1039/b9nr00127a

63. Pal H, Sharma V, Sharma M (2014) Influence of functionalization on mechanical and electrical properties of carbon nanotube-based silver composites. Philosophical Magazine 94:1478–1492. https://doi.org/10.1080/14786435.2014.892221

64. Lara IV, Zanella I, Fagan SB (2014) Functionalization of carbon nanotube by carboxyl group under radial deformation. Chemical Physics 428:117–120. https://doi.org/10.1016/j.chemphys.2013.11.007

65. Fujigaya T, Nakashima N (2015) Non-covalent polymer wrapping of carbon nanotubes and the role of wrapped polymers as functional dispersants. Science and Technology of Advanced Materials 16:024802. https://doi.org/10.1088/1468-6996/16/2/024802

66. Chik MW, Hussain Z, Zulkefeli M, et al (2019) Polymer-wrapped single-walled carbon nanotubes: a transformation toward better applications in healthcare. Drug Deliv and Transl Res 9:578–594. https://doi.org/10.1007/s13346-018-0505-9

67. Yu M-F (2004) Fundamental Mechanical Properties of Carbon Nanotubes: Current Understanding and the Related Experimental Studies. J Eng Mater Technology 126:271–278. https://doi.org/10.1115/1.1755245

68. Montazeri A, Javadpour J, Khavandi A, et al (2010) Mechanical properties of multi-walled carbon nanotube/epoxy composites. Mater Des 31:4202–4208. https://doi.org/10.1016/j.matdes.2010.04.018

69. Shi D-L, Feng X-Q, Huang YY, et al (2004) The Effect of Nanotube Waviness and Agglomeration on the Elastic Property of Carbon Nanotube-Reinforced Composites. J Eng Mater Technology 126:250–257. https://doi.org/10.1115/1.1751182

70. Zhan H, Chen YW, Shi QQ, et al (2022) Highly aligned and densified carbon nanotube films with superior thermal conductivity and mechanical strength. Carbon 186:205–214. https://doi.org/10.1016/j.carbon.2021.09.069

71. Schlesinger M, Paunovic M (2011) Modern Electroplating

72. PubChem: Potassium silver cyanide. In: National Library of Medicine: National Center for Biotechnology Information. https://pubchem.ncbi.nlm.nih.gov/compound/Potassium-silver-cyanide

73. (2020) E-Brite 50/50 RTP Non-Cyanide Alkaline Silver Plating

74. Abudayyeh OK, Gapp ND, Nelson C, et al (2016) Silver–Carbon-Nanotube Metal Matrix Composites for Metal Contacts on Space Photovoltaic Cells. IEEE J Photovoltaics 6:337–342. https://doi.org/10.1109/JPHOTOV.2015.2480224

75. Abudayyeh OK (2016) Development of Metal Matrix Composite Gridlines for Space Photovoltaics. University of New Mexico

76. Martin PM (2010) Handbook of deposition technologies for films and coatings: science, applications and technology. Elsevier, Amsterdam; Boston

77. Majumder M, Rendall C, Li M, et al (2010) Insights into the physics of spray coating of SWNT films. Chemical Engineering Science 65:2000–2008. https://doi.org/10.1016/j.ces.2009.11.042

78. Deegan RD, Bakajin O, Dupont TF, et al (1997) Capillary flow as the cause of ring stains from dried liquid drops. Nature 389:827–829. https://doi.org/10.1038/39827

79. Lefebvre AH (1989) Properties of Sprays. Part Part Syst Charact 6:176–186. https://doi.org/10.1002/ppsc.19890060129

80. Fernando RH, Xing L-L, Glass JE (2000) Rheology parameters controlling spray atomization and roll misting behavior of waterborne coatings. Progress in Organic Coatings 40:35–38. https://doi.org/10.1016/S0300-9440(00)00112-0

81. Verding P, Deferme W, Steffen W (2020) Velocity and size measurement of droplets from an ultrasonic spray coater using photon correlation spectroscopy and turbidimetry. Appl Opt 59:7496. https://doi.org/10.1364/AO.402579

82. Wan LSC, Heng PWS, Liew CV (1995) The influence of liquid spray rate and atomizing pressure on the size of spray droplets and spheroids. International Journal of Pharmaceutics 118:213–219. https://doi.org/10.1016/0378-5173(94)00363-A

83. Carey T, Jones C, Le Moal F, et al (2018) Spray-Coating Thin Films on Three-Dimensional Surfaces for a Semitransparent Capacitive-Touch Device. ACS Appl Mater Interfaces 10:19948–19956. https://doi.org/10.1021/acsami.8b02784

84. Panão M (2022) Ultrasonic Atomization: New Spray Characterization Approaches. Fluids 7:29. https://doi.org/10.3390/fluids7010029

85. Deepu P, Peng C, Moghaddam S (2018) Dynamics of ultrasonic atomization of droplets. Experimental Thermal and Fluid Science 92:243–247. https://doi.org/10.1016/j.expthermflusci.2017.11.021

86. Lang RJ (1962) Ultrasonic Atomization of Liquids. The Journal of the Acoustical Society of America 34:6–8. https://doi.org/10.1121/1.1909020

87. Willey AD, et. al. (2012) Ultrasonic Spraying of Carbon Nanotubes using NMP. TechConnect [u.a.], Danville, Calif

88. Schuh CA (2006) Nanoindentation studies of materials. Materials Today 9:32–40. https://doi.org/10.1016/S1369-7021(06)71495-X

89. Oliver WC, Pharr GM (1992) An improved technique for determining hardness and elastic modulus using load and displacement sensing indentation experiments. J Mater Res 7:1564–1583. https://doi.org/10.1557/JMR.1992.1564

90. Oliver WC, Pharr GM (2004) Measurement of hardness and elastic modulus by instrumented indentation: Advances in understanding and refinements to methodology. J Mater Res 19:3–20. https://doi.org/10.1557/jmr.2004.19.1.3

91. Kim J-Y, Lee J-J, Lee Y-H, et al (2006) Surface roughness effect in instrumented indentation: A simple contact depth model and its verification. J Mater Res 21:2975–2978. https://doi.org/10.1557/jmr.2006.0370

92. Fischer-Cripps AC (2006) Critical review of analysis and interpretation of nanoindentation test data. Surface and Coatings Technology 200:4153–4165. https://doi.org/10.1016/j.surfcoat.2005.03.018

93. Bolshakov A, Pharr GM (1998) Influences of pileup on the measurement of mechanical properties by load and depth sensing indentation techniques. J Mater Res 13:1049–1058. https://doi.org/10.1557/JMR.1998.0146

94. Khursheed A (2011) Scanning electron microscope optics and spectrometers. World Scientific, New Jersey

95. TA Instruments TA Instruments Dynamic Mechanical Analyzer

96. TA Instruments (2019) Dynamic Mechanical Analysis Basic Theory & Applications Training

97. Becquerel AE (1839) Memoire sur les Effects d'Electriques Produits Sous l'Influence des Rayons Solaires. Comptes Rendus de l'Academie des Sciences 9:561–567

98. Chapin DM, Fuller CS, Pearson GL (1954) A New Silicon *p-n* Junction Photocell for Converting Solar Radiation into Electrical Power. Journal of Applied Physics 25:676–677. https://doi.org/10.1063/1.1721711

99. Martin (John) M. Atalla (MOSFET). In: National Inventors Hall of Fame. https://www.invent.org/inductees/martin-john-m-atalla. Accessed 10 Mar 2022

100. Black LE (2016) New Perspectives on Surface Passivation: Understanding the Si-Al2O3 Interface. Springer International Publishing, Cham

101. Wolf M (1960) Limitations and Possibilities for Improvement of Photovoltaic Solar Energy Converters: Part I: Considerations for Earth's Surface Operation. Proc IRE 48:1246–1263. https://doi.org/10.1109/JRPROC.1960.287647

102. Flat A, Milnes AG (1979) Optimization of multi-layer front-contact grid patterns for solar cells. Solar Energy 23:289–299. https://doi.org/10.1016/0038-092X(79)90122-1

103. Beckman WA (1967) Optimization of Contact Grid Spacing for High Solar Flux Photovoltaic Cells. Journal of Engineering for Power 89:415–418. https://doi.org/10.1115/1.3616707

104. Mandelkorn J, Rappaport P, Ross B, et al (1962) Radiation-Resistant Solar Cells

105. Easton RL, Votaw MJ (1959) Vanguard I IGY Satellite (1958 Beta). Review of Scientific Instruments 30:70–75. https://doi.org/10.1063/1.1716492

106. Blakers AW, Green MA (1986) 20% efficiency silicon solar cells. Appl Phys Lett 48:215–217. https://doi.org/10.1063/1.96799

107. Geisz JF, Friedman DJ, Ward JS, et al (2008) 40.8% efficient inverted triple-junction solar cell with two independently metamorphic junctions. Appl Phys Lett 93:123505. https://doi.org/10.1063/1.2988497

108. NREL Best Research-Cell Efficiency Chart. In: NREL - Photovoltaic Research. https://www.nrel.gov/pv/cell-efficiency.html

109. Honsberg C, Bowden S PV Education. In: PV Education. pveducation.org

110. Kasewieter J, Haase F, Kontges M (2016) Model of Cracked Solar Cell Metallization Leading to Permanent Module Power Loss. IEEE J Photovoltaics 6:28–33. https://doi.org/10.1109/JPHOTOV.2015.2487829

111. Zhang Y, Liu Q, Hou J, et al (2021) Experimental study on micro-crack initiation in photovoltaic polycrystalline silicon wafer. Materials Science in Semiconductor Processing 123:105539. https://doi.org/10.1016/j.mssp.2020.105539

112. Demant M, Welschehold T, Oswald M, et al (2016) Microcracks in Silicon Wafers I: Inline Detection and Implications of Crack Morphology on Wafer Strength. IEEE J Photovoltaics 6:126–135. https://doi.org/10.1109/JPHOTOV.2015.2494692

113. Demant M, Welschehold T, Kluska S, Rein S (2016) Microcracks in Silicon Wafers II: Implications on Solar Cell Characteristics, Statistics and Physical Origin. IEEE J Photovoltaics 6:136–144. https://doi.org/10.1109/JPHOTOV.2015.2465172

114. Papargyri L, Theristis M, Kubicek B, et al (2020) Modelling and experimental investigations of microcracks in crystalline silicon photovoltaics: A review. Renewable Energy 145:2387–2408. https://doi.org/10.1016/j.renene.2019.07.138

115. Kajari-Schröder S, Kunze I, Eitner U, Köntges M (2011) Spatial and orientational distribution of cracks in crystalline photovoltaic modules generated by mechanical load tests. Solar Energy Materials and Solar Cells 95:3054–3059. https://doi.org/10.1016/j.solmat.2011.06.032

116. Kikelj M, Lipovšek B, Bokalič M, Topič M (2021) Spatially resolved electrical modelling of cracks and other inhomogeneities in crystalline silicon solar cells. Prog Photovolt Res Appl 29:124–133. https://doi.org/10.1002/pip.3348

117. Park J, Lee S-H, Lee J, et al (2017) Accurate measurement of specific tensile strength of carbon nanotube fibers with hierarchical structures by vibroscopic method. RSC Adv 7:8575–8580. https://doi.org/10.1039/C6RA26607J

118. Ruoff RS, Qian D, Liu WK (2003) Mechanical properties of carbon nanotubes: theoretical predictions and experimental measurements. Comptes Rendus Physique 4:993–1008. https://doi.org/10.1016/j.crhy.2003.08.001

119. Salvetat-Delmotte J-P, Rubio A (2002) Mechanical properties of carbon nanotubes: a fiber digest for beginners. Carbon 40:1729–1734. https://doi.org/10.1016/S0008-6223(02)00012-X

120. Bernholc J, Brenner D, Buongiorno Nardelli M, et al (2002) Mechanical and Electrical Properties of Nanotubes. Annu Rev Mater Res 32:347–375. https://doi.org/10.1146/annurev.matsci.32.112601.134925

121. Marinho B, Ghislandi M, Tkalya E, et al (2012) Electrical conductivity of compacts of graphene, multi-wall carbon nanotubes, carbon black, and graphite powder. Powder Technology 221:351–358. https://doi.org/10.1016/j.powtec.2012.01.024

122. (2018) ZTJ Space Solar Cell - 3rd Generation Triple-Junction Solar Cell for Space Applications

123. Parikh HR, Buratti Y, Spataru S, et al (2020) Solar Cell Cracks and Finger Failure Detection Using Statistical Parameters of Electroluminescence Images and Machine Learning. Applied Sciences 10:8834. https://doi.org/10.3390/app10248834

124. Dhimish M, Holmes V (2019) Solar cells micro crack detection technique using state-of-the-art electroluminescence imaging. Journal of Science: Advanced Materials and Devices 4:499–508. https://doi.org/10.1016/j.jsamd.2019.10.004

125. Prevo BG, Velev OD (2004) Controlled, Rapid Deposition of Structured Coatings from Micro- and Nanoparticle Suspensions. Langmuir 20:2099–2107. https://doi.org/10.1021/la035295j

126. Nix WD, Gao H (1998) Indentation size effects in crystalline materials: A law for strain gradient plasticity. Journal of the Mechanics and Physics of Solids 46:411–425. https://doi.org/10.1016/S0022-5096(97)00086-0

127. Pharr GM, Herbert EG, Gao Y (2010) The Indentation Size Effect: A Critical Examination of Experimental Observations and Mechanistic Interpretations. Annu Rev Mater Res 40:271–292. https://doi.org/10.1146/annurev-matsci-070909-104456

128. Voyiadjis G, Yaghoobi M (2017) Review of Nanoindentation Size Effect: Experiments and Atomistic Simulation. Crystals 7:321. https://doi.org/10.3390/cryst7100321

129. Zhang B, Wang W, Zhang GP (2006) Depth dependent hardness variation in Ni–P amorphous film under nanoindentation. Materials Science and Technology 22:734–737. https://doi.org/10.1179/026708306X81540

130. Beck CE, Hofmann F, Eliason JK, et al (2017) Correcting for contact area changes in nanoindentation using surface acoustic waves. Scripta Materialia 128:83–86. https://doi.org/10.1016/j.scriptamat.2016.09.037

131. McElhaney KW, Vlassak JJ, Nix WD (1998) Determination of indenter tip geometry and indentation contact area for depth-sensing indentation experiments. J Mater Res 13:1300–1306. https://doi.org/10.1557/JMR.1998.0185

132. Tsui TY, Oliver WC, Pharr GM (1996) Influences of stress on the measurement of mechanical properties using nanoindentation: Part I. Experimental studies in an aluminum alloy. J Mater Res 11:752–759. https://doi.org/10.1557/JMR.1996.0091

133. Weil R, Paquin R (1960) The Relationship between Brightness and Structure in Electroplated Nickel. J Electrochem Soc 107:87. https://doi.org/10.1149/1.2427639

134. PubChem: Chloroform. In: National Library of Medicine: National Center for Biotechnology Information. https://pubchem.ncbi.nlm.nih.gov/compound/Chloroform

135. PubChem: Water. In: National Library of Medicine: National Center for Biotechnology Information. https://pubchem.ncbi.nlm.nih.gov/compound/962

136. Part 4 - Droplet size. In: The Spray Nozzle People. https://www.spray-nozzle.co.uk/home/resources/engineering-resources/guide-to-spray-properties/4--droplet-size

137. Arganda-Carreras I, Kaynig V, Rueden C, et al (2017) Trainable Weka Segmentation: a machine learning tool for microscopy pixel classification. Bioinformatics 33:2424–2426. https://doi.org/10.1093/bioinformatics/btx180

138. Boesl B, Lahiri D, Behdad S, Agarwal A (2014) Direct observation of carbon nanotube induced strengthening in aluminum composite via in situ tensile tests. Carbon 69:79–85. https://doi.org/10.1016/j.carbon.2013.11.061

139. Abaqus 6.14 27.1.1 Element library: overview

140. Silver, Ag

141. Chavez A, Rummel B, Dowdy N, et al (2021) Optimization of Carbon-Nanotube-Reinforced Composite Gridlines Towards Commercialization. In: 2021 IEEE 48th Photovoltaic Specialists Conference (PVSC). IEEE, Fort Lauderdale, FL, USA, pp 1427–1429

142. Abudayyeh OK, Nelson C, Bradshaw GK, et al (2019) Crack-Tolerant Metal Composites as Photovoltaic Gridlines. IEEE J Photovolt 9:1754–1758. https://doi.org/10.1109/JPHOTOV.2019.2939096

143. Patra S, Ajayan PM, Narayanan TN (2020) Dynamic mechanical analysis in materials science: The Novice's Tale. Oxford Open Materials Science 1:itaa001. https://doi.org/10.1093/oxfmat/itaa001

144. Measurement of Solar Cell Efficiency. In: PV Education. https://www.pveducation.org/pvcdrom/characterisation/measurement-of-solar-cell-efficiency